



Diese Dissertation haben begutachtet:

\_\_\_\_\_  
Prof.Dr. K.Held

\_\_\_\_\_  
Prof.Dr. R.Valentí

\_\_\_\_\_  
Prof.Dr. E.Arrigoni

## DISSERTATION

---

# Towards an *ab initio* treatment of materials with local and non-local electronic correlations

---

Ausgeführt zum Zwecke der Erlangung des akademischen Grades einer Doktorin  
der Naturwissenschaften

unter der Leitung von

Univ. Prof. Dr. Karsten Held

Dr. Jan M. Tomczak und Dr. Patrik Thunström

E138—Institut für Festkörperphysik

eingereicht an der Technischen Universität Wien

Fakultät für Physik

von

Dipl.-Ing. Anna Galler, BSc, BA

Matrikelnummer: 0727375

Wien, im Juni 2017

---



# Kurzfassung

Materialien mit starken elektronischen Korrelationen bergen eine Vielzahl faszinierender physikalischer Phänomene; darunter z.B. der Mott Metall-Isolator Übergang in  $V_2O_3$ , Magnetismus in Fe und Ni, die thermoelektrischen Eigenschaften von  $CrSb_2$  oder  $LiRh_2O_4$  und die Hochtemperatur-Supraleitung in bestimmten Kupraten. Es ist also nicht erstaunlich, dass stark korrelierte Elektronensysteme einen regen Forschungsgegenstand darstellen. Was deren theoretische Beschreibung betrifft, so hat sich über die letzten 20 Jahre die Kombination aus Dichtefunktionaltheorie (DFT) und dynamischer Molekularfeldtheorie (DMFT) erfolgreich etabliert. Diese DFT+DMFT Methode wird im ersten Teil dieser Dissertation vorgestellt. Gleich im Anschluss werden die Ergebnisse einer DFT+DMFT Rechnung präsentiert, in deren Rahmen ich die magnetischen Eigenschaften von FeAl untersucht habe. FeAl ist im Experiment paramagnetisch, während konventionelle DFT-Rechnungen einen ferromagnetischen Grundzustand liefern. Hier zeige ich, dass eine bessere Beschreibung elektronischer Korrelationen im Rahmen der DFT+DMFT Methode das Nicht-Vorhandensein von Ferromagnetismus in FeAl erklärt. In der Tat werden laut DFT+DMFT die lokalen magnetische Momente von  $1.6 \mu_B$  der Fe-Atome durch Spin-Fluktuationen stark abgeschirmt, sodass sich keine ferromagnetische Ordnung ausbilden kann.

Die DFT+DMFT Methode beschreibt erfolgreich alle lokalen elektronischen Korrelationen, beinhaltet aber keine nicht-lokalen Korrelationen. Letztere sind jedoch in bestimmten Fällen von Bedeutung, z.B. in Materialien mit einer 2d Schicht-Struktur. Um auch nicht-lokale elektronische Korrelationen zu berücksichtigen, sind in letzter Zeit zahlreiche Erweiterungen der DMFT entwickelt worden. Darunter findet sich die dynamische Vertex-Approximation (D $\Gamma$ A), eine diagrammatische Erweiterung der DMFT. Die D $\Gamma$ A wurde schon erfolgreich verwendet, um Modell-Systeme—insbesondere das Ein-Band Hubbard Modell—zu untersuchen. Ein zentrales Thema dieser Dissertation ist die Erweiterung der D $\Gamma$ A, um damit Materialeigenschaften zu berechnen. Diese neu entwickelte AbinitioD $\Gamma$ A stellt eine umfassende diagrammatische Methode dar, die sowohl

alle DMFT- und GW-Diagramme, als auch zusätzliche nicht-lokale elektronische Korrelationen, z.B. nicht-lokale Spin-Fluktuationen, beinhaltet. Im zweiten Teil dieser Dissertation werden die neue AbinitioDFA Methode und ihre numerische Implementierung im Detail präsentiert, zusammen mit den ersten AbinitioDFA Ergebnissen für  $\text{SrVO}_3$ .

# Abstract

Materials with strong electronic correlations exhibit many fascinating physical phenomena: from the Mott metal-insulator transition in  $V_2O_3$  and the magnetism in Fe and Ni, to the large thermopower in  $CrSb_2$  or  $LiRh_2O_4$  and the high-temperature superconductivity in some cuprates. Thus, strongly correlated materials are currently a very vivid and interesting field of research. On the theoretical side, the DFT+DMFT approach (density functional theory combined with dynamical mean-field theory), which will be introduced in the first part of this thesis, has become a well-established method over the last two decades. In this thesis, the results of a DFT+DMFT study for the magnetic properties of FeAl will be presented. While standard DFT studies fail to correctly predict the experimentally observed paramagnetism in FeAl, I show here that the absence of ferromagnetism can be explained by the correlation-induced screening of short-lived local magnetic moments of  $1.6 \mu_B$  on the Fe site.

However, even though DFT+DMFT works well for many correlated compounds, it still remains a mean-field theory in the spatial coordinates, which can capture only local electronic correlations. Thus, in order to include also non-local electronic correlations, which are important e.g. in materials with a layered 2d structure, extensions of DMFT have been developed in recent years. Among them, there is the dynamical vertex approximation (D $\Gamma$ A), a diagrammatic extension of DMFT. D $\Gamma$ A has already been used successfully to study model systems, in particular the one-band Hubbard model. A main part of this thesis has been the extension of D $\Gamma$ A to realistic materials' computations. This newly developed AbinitioD $\Gamma$ A method represents a unifying framework which includes both, the GW and DMFT diagrams, but also important non-local correlations beyond, e.g. non-local spin fluctuations. In the second part of this thesis, the AbinitioD $\Gamma$ A method and its numerical implementation are discussed in detail, together with the first AbinitioD $\Gamma$ A results for the transition metal oxide  $SrVO_3$ .



*Für meine Eltern Elisabeth und Martin*





*“There is no gate, no lock, no bolt that you can set upon the freedom of my mind.”*

Virginia Woolf, *A Room of One's Own* (1929)



# Contents

<b>Introduction</b>	<b>1</b>
<b>1 The DFT+DMFT approach</b>	<b>5</b>
1.1 The solid state Hamiltonian . . . . .	5
1.2 Density functional theory (DFT) . . . . .	7
1.3 The multi-orbital Hubbard model . . . . .	11
1.4 Wannier projection . . . . .	14
1.5 <i>Ab initio</i> computation of the Coulomb interaction . . . . .	18
1.6 Dynamical mean-field theory (DMFT) . . . . .	21
1.6.1 Green's functions and Feynman diagrams . . . . .	22
1.6.2 Diagrammatic content of DMFT . . . . .	25
1.6.3 Mapping onto an Anderson impurity model . . . . .	26
1.7 DFT+DMFT double counting correction . . . . .	28
1.8 Summary: DFT+DMFT flow . . . . .	30
1.9 Spectral functions and analytical continuation . . . . .	32
<b>2 Screened moments and absence of ferromagnetism in FeAl</b>	<b>37</b>
2.1 Motivation . . . . .	37
2.2 Electronic structure within DFT . . . . .	39
2.3 DMFT self-energy and spectral function . . . . .	40
2.4 DMFT magnetic properties . . . . .	42
<b>3 Beyond DMFT: the dynamical vertex approximation (D<math>\Gamma</math>A)</b>	<b>47</b>
3.1 Extensions of DMFT . . . . .	47
3.2 An introduction to D $\Gamma$ A . . . . .	50
3.2.1 The two-particle Green's function . . . . .	50
3.2.2 The basic idea of D $\Gamma$ A . . . . .	52
3.2.3 Full parquet version . . . . .	54
3.2.4 Ladder approximation . . . . .	58
<b>4 <i>Ab initio</i> dynamical vertex approximation</b>	<b>63</b>
4.1 Derivation of the equations . . . . .	63
4.1.1 Extracting the local irreducible vertex $\Gamma_{\text{loc}}$ . . . . .	64
4.1.2 The non-local Coulomb interaction $V^{\mathbf{q}}$ . . . . .	69
4.1.3 Construction of the full vertex $F^{\mathbf{q}}$ . . . . .	70
4.1.4 Equation of motion . . . . .	75

4.2	Implementational details . . . . .	78
4.2.1	DFT+DMFT computation . . . . .	79
4.2.2	Preprocessing of the AbinitioDΓA input data . . . . .	81
4.2.3	The main AbinitioDΓA program . . . . .	84
4.2.4	Numerical effort . . . . .	93
4.3	Test cases . . . . .	94
4.3.1	One-band Hubbard model . . . . .	94
4.3.2	Two-band atomic limit . . . . .	97
<b>5</b>	<b>AbinitioDΓA results for SrVO<sub>3</sub></b>	<b>101</b>
<b>6</b>	<b>Conclusion and outlook</b>	<b>109</b>
	<b>Bibliography</b>	<b>123</b>
	<b>Acknowledgements</b>	<b>123</b>
	<b>Curriculum vitae</b>	<b>125</b>

# Introduction

In solid state physics, one can explore countless fascinating materials and physical phenomena therein. This ranges from naturally grown minerals, which come in a huge variety of colors and shapes, to engineered functional materials, which are used in technological applications. The latter include e.g. semiconducting devices in computers, magnetic materials for storage media, thermoelectrics for the conversion of waste heat into electricity, or superconducting magnets used in high-magnetic-field experiments. All physical phenomena in the solid state—like magnetism or superconductivity—basically arise from the interplay among the constituting electrons and ions. However, given the huge amount of particles  $N \sim \mathcal{O}(10^{23})$  in a solid, it is very challenging to start from the microscopic Coulomb interaction between the single electrons and ions to finally get some insight into macroscopic physical phenomena.

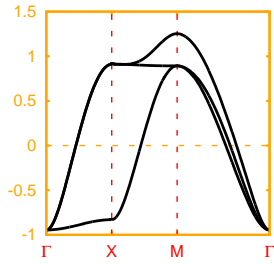


FIGURE 1: DFT band-structure of  $\text{SrVO}_3$ .

The density functional theory (DFT) [1, 2] which, in principle, starts *ab initio* from the Coulomb interaction among the electrons and ions in a solid has been very successful in predicting the electronic structure of many compounds. Here, the many-body problem of  $N \sim \mathcal{O}(10^{23})$  particles interacting with each other is not solved straightforwardly. Instead, several approximations are needed in order to make the problem treatable. As a first approximation, the ions are seen as part of a static lattice potential. The electron-electron Coulomb interaction, on the other hand, is also approximated very roughly. In fact, within DFT the many-electron problem is replaced by an effective single-electron problem, where the effect of all the remaining electrons is only considered through an averaged mean-field. The resulting single-electron problem is usually numerically solvable and the electronic band-structure and density of states of realistic materials can be computed. Nowadays, even complex heterostructures and surfaces (see e.g. Refs. [3, 4]) are treatable within DFT. Furthermore, the computed results often agree very well with the ones obtained by photoemission experiments. This

is rather surprising, since the effective single-particle problem solved within DFT approximates the original many-body problem only very roughly. But it turns out that, especially in metals, electronic screening processes are often so effective that the mean-field approach within DFT can be a good approximation.

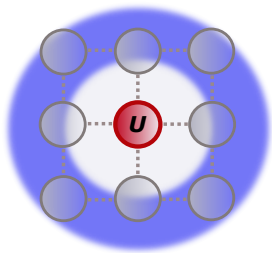


FIGURE 2: The DMFT impurity model.

However, DFT usually fails to correctly predict the electronic structure of materials with partially filled  $d$  or  $f$  orbitals. This is due to the fact that the partially filled  $3d$  orbitals in transition metal elements (from Ti to Cu) and the  $4f$  orbitals in rare earth elements (from Ce to Yb) are rather localized. Thus, electronic screening processes are not very effective in these orbitals and a mean-field-like treatment of the electron-electron Coulomb interaction is not sufficient any more. Instead, the strong Coulomb interaction correlates the movement of the electrons. Thus,

in these strongly correlated materials, a better treatment of electronic correlations is needed. This is possible with the dynamical mean-field theory (DMFT) [5, 6]. As its name suggests, DMFT is still a mean-field theory in the spatial coordinates. However, in contrast to usual mean-field theories, DMFT is a diagrammatic technique which does not take a time average—it is a *dynamical* mean-field theory. Thus, it captures all dynamical, local electronic correlations, e.g. local spin fluctuations. It has been shown that DMFT provides the exact solution of the Hubbard model in infinite dimensions [5]. However, it turns out that DMFT is usually also a good approximation in three dimensions. Furthermore, when combined with DFT in the so-called DFT+DMFT approach, physical quantities of strongly correlated materials can be computed. This includes spectral functions, magnetic susceptibilities, optical conductivity or thermoelectric response functions. Indeed, over the last decade, DMFT has become a well-established and standard method to treat strongly correlated materials.

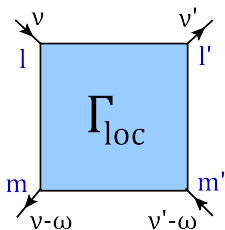


FIGURE 3: The local vertex function  $\Gamma_{\text{loc}}$  used in AbinitioDFA.

Nevertheless, DMFT still remains a mean-field theory in the spatial coordinates and it does not capture any non-local electronic correlations. Especially in materials with a 2d or 1d structure, e.g. superconducting cuprates with their layered crystal structure, or close to a second-order phase transition, e.g. the transition from para- to ferromagnetism, a mean-field in space can be a poor approximation. Here, one needs to include also spatial electronic correlations. In fact, in recent years, extensions of DMFT have emerged in order to capture also non-local electronic correlations. One

prominent diagrammatic extension of DMFT is the so-called dynamical vertex approximation (D $\Gamma$ A) [7]. The latter builds on the local DMFT vertex function  $\Gamma_{\text{loc}}$ —which is basically a two-particle scattering diagram—and constructs non-local Feynman diagrams through the Bethe-Salpeter and/or Parquet equations. D $\Gamma$ A has already been successfully used for studying the one-band Hubbard model, e.g. to calculate critical exponents and phase diagrams [8, 9]. One main task of this thesis has been the extension of D $\Gamma$ A to multi-orbital systems, so that realistic materials’ computations become feasible. This newly developed AbinitioD $\Gamma$ A starts from a local vertex function  $\Gamma_{\text{loc}}$ , which is obtained from a DFT+DMFT computation, and constructs non-local Feynman diagrams through the non-local Bethe-Salpeter equation. Furthermore, AbinitioD $\Gamma$ A is not only the generalization of D $\Gamma$ A to multi-orbital systems, but it includes also a non-local Coulomb interaction  $V^{\mathbf{q}}$  beyond the Hubbard model. Thus, AbinitioD $\Gamma$ A is a unifying framework which includes both, the GW and DMFT diagrams, but also important non-local correlations beyond, e.g. non-local spin fluctuations. The method development and implementation of AbinitioD $\Gamma$ A has been one main task of this thesis, which is structured as follows:

- In Chap. 1, the well-established DFT+DMFT approach to strongly correlated materials is introduced. The chapter starts with a discussion of the general solid state Hamiltonian and density functional theory (DFT). Then, the intermediate steps necessary to combine DFT and DMFT—namely the Wannier projection and the *ab initio* computation of the interaction parameters through the constrained random phase approximation (cRPA)—are described. Finally, the multi-orbital Hubbard model and its solution within DMFT are discussed.
- In Chap. 2, the results of a DFT+DMFT study for the intermetallic FeAl are presented. In this study, I have investigated the magnetic properties of FeAl. The latter are intriguing since DFT predicts a ferromagnetic ground-state for FeAl, while the material is found to be paramagnetic in experiment. Here, by computing magnetic susceptibilities within DFT+DMFT, I show that the absence of ferromagnetism in FeAl can be explained by a screening of short-lived local magnetic moments. The results presented in this chapter have already been published in the article *A. Galler et al., Phys. Rev. B 92, 205132 (2015)*.
- Chap. 3 provides an introduction to the dynamical vertex approximation (D $\Gamma$ A), including its full Parquet version and ladder approximation. Here—before dealing with all the details of the newly developed AbinitioD $\Gamma$ A formalism in the following chapter—an overview of the D $\Gamma$ A method and its basic ideas, which have been developed over the last years, is given.

- In Chap. 4, the newly developed AbinitioDFA method and its implementation are presented in detail. First, all multi-orbital equations are derived and the corresponding Feynman diagrams are depicted. Next, I discuss some implementational details and the structure of the newly developed AbinitioDFA program. Finally, the results of some test cases are shown. Part of the equations and diagrams in this chapter have already been presented in a similar, but shorter version in the article *A. Galler et al., Phys. Rev. B 95, 115107 (2017)*.
- In Chap. 5, the first AbinitioDFA results for the transition metal oxide  $\text{SrVO}_3$  are shown and discussed. Most of the results presented in this chapter have already been published in *A. Galler et al., Phys. Rev. B 95, 115107 (2017)*.



# Chapter 1

## The DFT+DMFT approach

*In this chapter, I introduce the DFT+DMFT approach (density functional theory combined with dynamical mean field theory), which is a well-established method to treat materials with strong electronic correlations. Starting from the general solid state Hamiltonian, I first briefly discuss the basic ideas of DFT. Then, the necessary steps to combine DFT with DMFT are presented: the Wannier projection and the computation of the Coulomb interaction through the constrained random phase approximation (cRPA). In the following, the multi-orbital Hubbard model, which is solved within DMFT, is discussed in detail. Finally, I present the DMFT, together with a short introduction to Green's functions and Feynman diagrams. In the end of the chapter, the DFT+DMFT approach is summarized in a flow chart, and methods to analytically continue the DFT+DMFT Green's function and self-energy are discussed.*

### 1.1 The solid state Hamiltonian

In solid state physics, the fundamental "theory of everything" is, in principle, known. Since in materials, at the relevant energy scales ranging from some meV to some eV, only the Coulomb interaction plays a role, the given problem basically consists in all the electrons and ions of the lattice interacting with each other via the Coulomb interaction. Usually also relativistic effects can be neglected so that the solid state Hamiltonian is given by

$$\hat{H} = \sum_i \frac{\mathbf{p}_i^2}{2m} + \sum_l \frac{\mathbf{P}_l^2}{2M_l} + \frac{1}{2} \sum_{k \neq l} \frac{Z_k Z_l e^2}{|\mathbf{R}_k - \mathbf{R}_l|} - \sum_{i,l} \frac{Z_l e^2}{|\mathbf{r}_i - \mathbf{R}_l|} + \frac{1}{2} \sum_{i \neq j} \frac{e^2}{|\mathbf{r}_i - \mathbf{r}_j|}, \quad (1.1)$$

where  $-e$  ( $Ze$ ),  $m$  ( $M$ ),  $\mathbf{r}$  ( $\mathbf{R}$ ) and  $\mathbf{p}$  ( $\mathbf{P}$ ) label the charge, the mass, the position and the momentum of the electrons (ions). The first two terms in Eq. (1.1) represent the

kinetic energy of the electrons and the ions. The other three terms instead describe the ion-ion, ion-electron and electron-electron Coulomb interaction, respectively.

At first glance, the Hamiltonian in Eq. (1.1) does not look overly complicated. However, due to the large number of particles  $N \sim \mathcal{O}(10^{23})$  in a solid, there is no hope to solve the problem exactly, neither analytically nor numerically. In fact, one is also not interested in the complete information about the solid state system under investigation. The complete information would correspond to knowing the full many-body wave function depending on all the coordinates of all the electrons and ions involved, or—seen in a semi-classical way—knowing about the movement of all the single electrons and ions in the solid. This large amount of information is neither interesting nor can it be processed or stored anywhere. Instead, one is usually interested in collective phenomena in a solid, where the interplay between the electrons and ions gives rise for example to magnetism, superconductivity or thermoelectricity. In order to theoretically describe these and other fascinating phenomena in solid state systems, one could already start from macroscopic observables. This is done in phenomenological approaches like the Landau theory for phase transitions. In these phenomenological, mostly thermodynamic approaches one directly works with macroscopic quantities like the total energy, entropy, pressure or temperature, without going back to their microscopic origins.

In this thesis, however, I am concentrating on *ab initio* approaches—namely density functional theory combined with dynamical mean field theory (DFT+DMFT) and the newly developed *ab initio* dynamical vertex approximation (AbinitioDFA). In this context, *ab initio* means *starting from first principles*, i.e. from the Hamiltonian in Eq. (1.1) describing the Coulomb interaction between all the electrons and ions in the lattice. Equivalently, *ab initio* is often also translated as *parameter free*. In fact, the Hamiltonian in Eq. (1.1) does not contain any external parameters. In practice, however, Eq. (1.1) needs to be approximated, which always involves some phenomenological parameters. Nevertheless, these approximations, foremost the local density approximation within density functional theory, are usually referred to being *ab initio*. Thus, in agreement with the common use of the term, in this work *ab initio* refers to approaches for realistic materials starting from their electronic structure, which is usually computed within density functional theory, and involving as few phenomenological parameters as possible.

**Born-Oppenheimer approximation** A first and very common simplification of the solid state Hamiltonian in Eq. (1.1) is the Born-Oppenheimer approximation, which assumes that the ionic degrees of freedom can be separated from the electronic ones. This approximation can usually be applied since the movement of the electrons is much

faster than that of the ions because of their difference in mass. Thus, the electrons adapt quasi instantly to a modified position of the ions in the lattice. If one is interested in the electronic structure only, the purely ionic part of the energy can be neglected and the ions can be seen as forming a static lattice potential  $V(\mathbf{r}) = \sum_l -\frac{Z_l e^2}{|\mathbf{r} - \mathbf{R}_l|}$ . Thus, the solid state Hamiltonian in the Born-Oppenheimer approximation reads

$$\hat{H} = \sum_i \frac{\mathbf{p}_i^2}{2m} + \sum_i V(\mathbf{r}_i) + \frac{1}{2} \sum_{i \neq j} \frac{e^2}{|\mathbf{r}_i - \mathbf{r}_j|}, \quad (1.2)$$

including the kinetic energy of the electrons, the interaction between the electrons and the lattice potential, and the electron-electron Coulomb interaction.

Despite the simplifications applied so far, it is still impossible to compute the eigenvalues and corresponding wave functions of the Hamiltonian in Eq. (1.2). Most of the complexity of the problem lies in the last term of Eq. (1.2), the electron-electron Coulomb interaction. Due to this mutual Coulomb interaction, the movement of every single electron is influenced by all the other electrons in the solid. In other words, all the electrons are correlated with each other. In general, these electronic correlations are of course not negligible. However, it turns out that in many solid state systems, especially in metals, the electrons are mobile enough to screen the Coulomb interaction, so that the effective electron-electron Coulomb interaction becomes weaker and electronic correlations are less important. In this context, a successful approach to make the problem in Eq. (1.2) treatable, consists in approximating the electron-electron Coulomb repulsion by an interaction between a single electron and an effective mean-field generated by all the other electrons. Such a mean-field approach, which replaces the correlated many-electron problem by an effective single-electron problem, has successfully been formulated within density functional theory (DFT), which will be discussed in the following.

## 1.2 Density functional theory (DFT)

**Hohenberg-Kohn theorem** In its mathematical formulation, density functional theory (DFT) is, in principle, an exact theory. In 1964, Hohenberg and Kohn [1] have shown that the ground state energy of an interacting electron gas in an external potential  $V(\mathbf{r})$  is a unique functional of the electron density  $E = E[\rho]$ ; and the true ground state electron density yields a minimum of  $E[\rho]$ . Since the interaction between the electrons and the lattice potential is the only non-universal contribution to the ground state energy, the Kohn-Sham energy functional can be written as

$$E[\rho] = \int d^3r V(\mathbf{r})\rho(\mathbf{r}) + F[\rho]. \quad (1.3)$$

This Hohenberg-Kohn-theorem marks the starting point of density functional theory. Please note that  $F[\rho]$  in Eq. (1.3) is a universal functional, valid for any number of particles and any potential. If  $F[\rho]$  was a known and sufficiently simple functional of  $\rho$ , it would be possible to find the ground state energy and density by minimizing the energy functional. But  $F[\rho]$  is not known and its determination leads back to the problems associated with the complexity of many-electron systems.

**Kohn-Sham equations** In 1965, Kohn and Sham [2] reformulated DFT by mapping it to a non-interacting electron system. Thus, they wrote the energy functional of Eq. (1.3) as

$$E[\rho] = \int d^3r V(\mathbf{r})\rho(\mathbf{r}) + \frac{1}{2} \int \int d^3r d^3r' \frac{\rho(\mathbf{r})\rho(\mathbf{r}')}{|\mathbf{r} - \mathbf{r}'|} + T_s[\rho] + E_{xc}[\rho], \quad (1.4)$$

where  $T_s[\rho]$  is the kinetic energy of the non-interacting electrons and  $E_{xc}[\rho]$  the exchange and correlation energy. Again, the true ground state electron density can in principle be found by minimizing the energy functional. Applying the variational principle to Eq. (1.4) leads to the single-electron Kohn-Sham equations

$$\left[ -\frac{\hbar^2}{2m} \Delta + V(\mathbf{r}) + \int d^3r' \frac{\rho(\mathbf{r}')}{|\mathbf{r} - \mathbf{r}'|} + \frac{\delta E_{xc}[\rho]}{\delta \rho(\mathbf{r})} \right] \psi_n(\mathbf{r}) = \epsilon_n \psi_n(\mathbf{r}), \quad (1.5)$$

which have to be solved self-consistently together with

$$\rho(\mathbf{r}) = \sum_n |\psi_n(\mathbf{r})|^2. \quad (1.6)$$

The last three terms in Eq. (1.5) can be seen as an effective potential  $V_{\text{eff}}(\mathbf{r}) = V(\mathbf{r}) + \int d^3r' \frac{\rho(\mathbf{r}')}{|\mathbf{r} - \mathbf{r}'|} + \frac{\delta E_{xc}[\rho]}{\delta \rho(\mathbf{r})}$  including exchange and correlation. Please note that, in principle, the Kohn-Sham wave functions  $\psi_n(\mathbf{r})$  are only auxiliary wave functions, which yield the correct ground state density and energy, and do not represent the physical orbitals of the system. Nevertheless, in DFT band-structure calculations the eigenvalues  $\epsilon_n$  in Eq. (1.5) are usually associated with the physical eigenenergies of the system.

**Local density approximation** In principle, the Kohn-Sham equations are suitable to perform electronic structure calculations, but the exact exchange and correlation energy  $E_{xc}[\rho]$  is an unknown functional and has to be approximated. In the common local density approximation (LDA), the functional dependence is restricted to the local electron density. Thus, the LDA exchange and correlation potential reads

$$E_{xc}^{LDA}[\rho] = \int d^3r \rho(\mathbf{r}) \epsilon_{xc}^{LDA}(\rho(\mathbf{r})), \quad (1.7)$$

where  $\epsilon_{xc}^{LDA}(\rho(\mathbf{r}))$  depends only on the electron density  $\rho$  at point  $\mathbf{r}$  and is independent of the density at neighboring points. In standard LDA computations, the corresponding exchange and correlation energy of a uniform electron gas is used to evaluate  $\epsilon_{xc}^{LDA}(\rho(\mathbf{r}))$  for a given local density. It is also possible to go beyond standard LDA by including local changes of the density that are mathematically described by the gradient  $\nabla\rho(\mathbf{r})$ . This yields the the generalized gradient approximation (GGA)

$$E_{xc}^{GGA}[\rho] = \int d^3r \rho(\mathbf{r}) \epsilon_{xc}^{GGA}(\rho(\mathbf{r}), \nabla\rho(\mathbf{r})). \quad (1.8)$$

Beside LDA and GGA, a variety of exchange and correlation functionals have been developed. Most of them are based on the GGA approximation, e.g. also the commonly used PBE functional [10]. In fact, optimizing and developing new exchange and correlation functionals that are suited for certain classes of materials, is still an ongoing field of research [11–13].

For many materials, LDA and related functionals provide good results, which is rather surprising since the Coulomb interaction itself is not local. But, as mentioned already, especially in metallic systems the electrons are mobile and able to screen their mutual interaction such that using a local expression for  $E_{xc}[\rho]$  can yield quite good results.

**Basis sets and pseudopotentials** As the lattice potential  $V(\mathbf{r})$  is periodic, the single-particle wave functions  $\psi_n(\mathbf{r})$  obtained from the Kohn-Sham equations are Bloch waves

$$\psi_{n\mathbf{k}}(\mathbf{r}) = e^{i\mathbf{k}\mathbf{r}} u_{n\mathbf{k}}(\mathbf{r}), \quad (1.9)$$

characterized by the envelope function  $e^{i\mathbf{k}\mathbf{r}}$  and  $u_{n\mathbf{k}}(\mathbf{r})$ , which has the periodicity of the lattice potential. Bloch waves are labeled by a crystal momentum  $\mathbf{k}$  lying inside the Brillouin zone and a band index  $n$ . In order to use the Kohn-Sham equations in DFT codes, one needs to introduce a set of basis functions  $\phi_j$  :

$$\psi_{n\mathbf{k}}(\mathbf{r}) = \sum_j c_{n\mathbf{k},j} \phi_{n\mathbf{k},j}(\mathbf{r}). \quad (1.10)$$

A very simple choice of basis functions are plane waves

$$\psi_{n\mathbf{k}}(\mathbf{r}) = \sum_j c_{n\mathbf{k},j} e^{i(\mathbf{k}+\mathbf{G}_j)\mathbf{r}}, \quad (1.11)$$

where  $\mathbf{G}_j$  represent reciprocal lattice vectors. Plane waves can be implemented straightforwardly, but in most systems a very large basis set of plane waves is required to obtain reasonable results. Especially close to the atomic cores, where the lattice potential diverges, a huge number of plane waves is needed. Thus, different approaches have

been developed. In particular two methods have shown to give very good results with a reasonable computational effort: one can choose a different basis set or introduce pseudopotentials.

Pseudopotentials are effective potentials that take into account the screening of the core electrons. In the core region the valence electrons interact with the pseudopotential, while outside the core region they are subject to the full potential. There exist different methods to construct pseudopotentials [14–16]. Of course, the pseudopotential always has to be constructed in a way that the wave functions are smooth at the boundary of the core region. A different approach, allowing the full potential to be used, consists in choosing a different basis set than plane waves. In the core region, atomic orbitals appear to be a good choice for basis functions, while in the interstitial region between the atoms, where the potential is quite smooth, plane waves are usually more appropriate. A combination of both leads, among others, to augmented plane waves (APW) [17]. In practice, one has to define a muffin tin radius, which describes non-overlapping spheres centered at the atomic cores. Within this radius, atomic orbitals are used as a basis set, while in the remaining interstitial region plane waves are used. On the sphere boundaries, the inner and the outer part of the APW have to match. By linearizing the problem one ends up with linearized augmented plane waves (LAPW) [18] which are used in the Wien2k code [19].

**Beyond DFT: Electronic correlations** DFT in its local density approximation works well for many materials—especially metals, where the Coulomb interaction is screened by itinerant electrons. In fact, for many compounds, DFT successfully predicts their electronic structure, which can be confirmed experimentally by angle-resolved photoemission experiments (ARPES). For materials with strong electronic correlations, however, DFT often fails to predict their electronic structure correctly. For example, for some compounds with partially filled  $d$  or  $f$  orbitals, DFT predicts a metallic behavior while they are found to be insulating in experiment. This is not a surprise since especially the partially filled  $3d$  orbitals in transition metal elements or the  $4f$  orbitals in rare earth elements are rather localized and electronic correlations play an important role. But in DFT electronic correlations are neglected or, in other words, included only on a mean-field level within the exchange and correlation potential. Thus, for strongly correlated materials, many-body approaches, which do not approximate the solid state Hamiltonian in Eq. (1.2) by an effective single-electron problem, are needed. Due to their complexity and numerical effort, it is usually, however, not possible to directly apply many-body techniques to the Hamiltonian in Eq. (1.2). Instead, model Hamiltonians, which are simpler but still capture the essential physics, must be derived first. One very

prominent model Hamiltonian in the field of strongly correlated electron systems is the so-called Hubbard model, which will be discussed in the following.

### 1.3 The multi-orbital Hubbard model

The Hubbard model, which was introduced by J. Hubbard already in 1963 [20], is the standard model for strongly correlated electron systems. As discussed in the previous Sec. 1.2, for electrons in strongly correlated orbitals, e.g. the partially filled  $3d$  orbitals in transition metal elements, a mean-field description like in DFT is not enough. On the other hand, a treatment beyond mean-field of the full solid state Hamiltonian in Eq. (1.2) is currently not feasible. Thus, the method of choice consists in introducing a simpler model Hamiltonian, which approximates the original solid state Hamiltonian while preserving its most important physical aspects. The model Hamiltonian of choice in this context is the Hubbard model, which will be introduced in the following.

We start from the solid state Hamiltonian of Eq. (1.2) in second quantization

$$\begin{aligned} \hat{H} = & \sum_{\sigma} \int d^3r \, \hat{\psi}_{\sigma}^{\dagger}(\mathbf{r}) \left[ -\frac{\hbar^2}{2m} \Delta + V(\mathbf{r}) \right] \hat{\psi}_{\sigma}(\mathbf{r}) \\ & + \frac{1}{2} \sum_{\sigma, \sigma'} \int d^3r \, d^3r' \, \hat{\psi}_{\sigma}^{\dagger}(\mathbf{r}) \hat{\psi}_{\sigma'}^{\dagger}(\mathbf{r}') \frac{e^2}{|\mathbf{r} - \mathbf{r}'|} \hat{\psi}_{\sigma'}(\mathbf{r}') \hat{\psi}_{\sigma}(\mathbf{r}), \end{aligned} \quad (1.12)$$

where  $\hat{\psi}_{\sigma}^{\dagger}(\mathbf{r})$  and  $\hat{\psi}_{\sigma}(\mathbf{r})$  are field operators that create or respectively annihilate an electron with spin  $\sigma$  at the position  $\mathbf{r}$ .<sup>1</sup> We can expand these field operators in terms of localized basis functions, e.g. maximally localized Wannier functions which are introduced in detail in Sec. 1.4. This yields

$$\hat{\psi}_{\sigma}^{(\dagger)}(\mathbf{r}) = \sum_{\mathbf{R}, m} w_{m\mathbf{R}}^{(*)}(\mathbf{r}) \hat{c}_{\mathbf{R}m\sigma}^{(\dagger)}, \quad (1.13)$$

where  $w_{m\mathbf{R}}(\mathbf{r})$  is the Wannier function of orbital  $m$  centered at lattice site  $\mathbf{R}$ , and  $\hat{c}_{\mathbf{R}m\sigma}^{\dagger}$  the corresponding creation operator. Please note that the orbitals  $m$  included in the Hubbard Hamiltonian are usually the rather localized, partially filled  $3d$  or  $4f$  orbitals in transition metal or rare earth elements.

---

<sup>1</sup>For the formalism of field operators and second quantization see e.g. Refs. [21, 22].

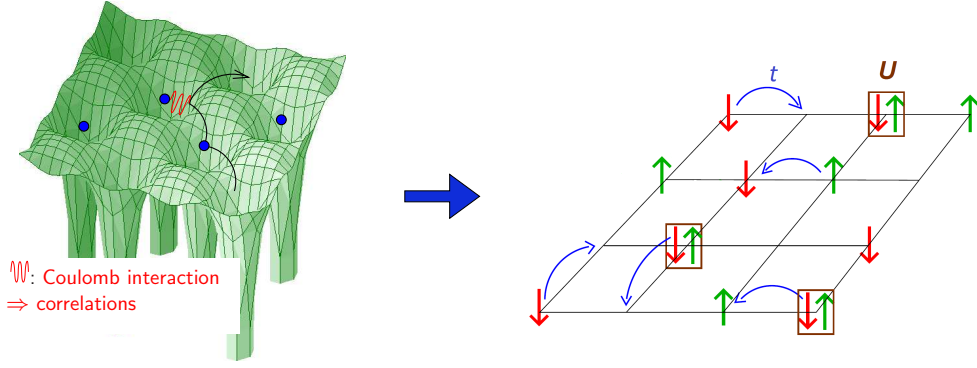


FIGURE 1.1: Left: In a solid, the electrons move (black arrow) within a lattice potential (green) and interact with each other (red wiggled line). Through the electron-electron Coulomb interaction, the movement of the electrons is correlated with each other. Right: In the (one-band) Hubbard model, the solid state problem is replaced by (spin up/down) electrons moving from site to site with hopping amplitude  $t$  and interacting with each other through the local Coulomb interaction  $U$ . (Reproduced from Ref. [23])

With Eq. (1.13), the solid state Hamiltonian in Eq. (1.12) can be rewritten as

$$\begin{aligned} \hat{H} = & - \sum_{\substack{\mathbf{R}\mathbf{R}' \\ mm',\sigma}} t_{mm'}(\mathbf{R}, \mathbf{R}') \hat{c}_{\mathbf{R}m\sigma}^\dagger \hat{c}_{\mathbf{R}'m'\sigma} \\ & + \frac{1}{2} \sum_{\substack{\mathbf{R}_1\mathbf{R}_2\mathbf{R}_3\mathbf{R}_4 \\ ll'mm' \\ \sigma\sigma'}} U_{lm'ml'}(\mathbf{R}_1, \mathbf{R}_2, \mathbf{R}_3, \mathbf{R}_4) \hat{c}_{\mathbf{R}_3m'\sigma}^\dagger \hat{c}_{\mathbf{R}_1l\sigma'}^\dagger \hat{c}_{\mathbf{R}_2m\sigma'} \hat{c}_{\mathbf{R}_4l'\sigma}, \end{aligned} \quad (1.14)$$

where the indices  $ll'mm'$  label different Wannier orbitals, while  $\mathbf{R}_i$  correspond to different lattice sites. Thus, the first term in the Hamiltonian represents the kinetic energy part and describes electrons hopping from orbital  $m'$  on lattice site  $\mathbf{R}'$  to orbital  $m$  on lattice site  $\mathbf{R}$ . The probability of this process is given by the hopping matrix  $t_{mm'}(\mathbf{R}, \mathbf{R}')$ . The second term in Eq. (1.14) instead represents the electron-electron Coulomb interaction. In detail, the hopping matrix  $t_{mm'}(\mathbf{R}, \mathbf{R}')$  and the Coulomb interaction  $U_{lm'ml'}(\mathbf{R}_1, \mathbf{R}_2, \mathbf{R}_3, \mathbf{R}_4)$  are given by

$$t_{mm'}(\mathbf{R}, \mathbf{R}') = - \int d^3r w_{m\mathbf{R}}^*(\mathbf{r}) \left[ -\frac{\hbar^2}{2m} \Delta + V(\mathbf{r}) \right] w_{m'\mathbf{R}'}(\mathbf{r}), \quad (1.15)$$

$$U_{lm'ml'}(\mathbf{R}_1, \mathbf{R}_2, \mathbf{R}_3, \mathbf{R}_4) = \int d^3r d^3r' w_{m'\mathbf{R}_3}^*(\mathbf{r}) w_{l\mathbf{R}_1}^*(\mathbf{r}') \frac{e^2}{|\mathbf{r} - \mathbf{r}'|} w_{m\mathbf{R}_2}(\mathbf{r}') w_{l'\mathbf{R}_4}(\mathbf{r}). \quad (1.16)$$

In practice, however, the Coulomb interaction  $U_{lm'ml'}$  cannot be computed so straightforward. In fact, usually only the localized  $3d$  or  $4f$  orbitals, which represent only a small subset of all bands in a solid, are included in the Hubbard Hamiltonian. In this "few-orbital" Hubbard Hamiltonian all remaining bands need effectively be taken into



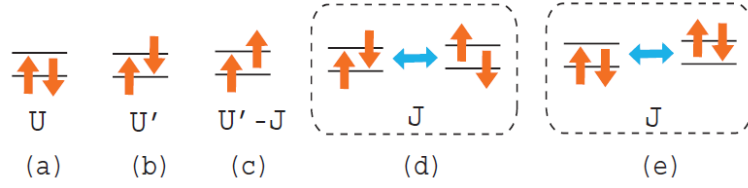


FIGURE 1.2: Coulomb interaction in the multi-orbital Hubbard model: (a) intra-orbital Coulomb interaction, (b-c) inter-orbital Coulomb interaction, (d) spin-flip and (e) pair-hopping term. (Taken from Ref. [25])

account by a screening of the Coulomb interaction  $U_{lm'm'l'}$ . In Sec. 1.5, this screening mechanism will be discussed in more detail and a method to compute the screened Coulomb interaction—the constrained random phase approximation (cRPA) [24]—will be presented.

**Kanamori interactions** Apart from the fact that only the localized, correlated orbitals are included in the Hamiltonian in Eq. (1.14), no further approximations have been made so far. However, in order to obtain a simplified model Hamiltonian—the multi-orbital Hubbard model—we now assume that only electrons on the same lattice site are interacting with each other. Thus, the Coulomb interaction becomes purely local and does not show any spatial dependence  $U_{lm'm'l'} = U_{lm'm'l'}(\mathbf{0}, \mathbf{0}, \mathbf{0}, \mathbf{0})$ .

In a further approximation for degenerate orbitals in a cubic crystal field (e.g. the  $t_{2g}$  orbitals in  $\text{SrVO}_3$ ), the four-index Coulomb interaction  $U_{lm'm'l'}$  is reduced to three interaction parameters: the intra-orbital Coulomb interaction  $U = U_{mmmm}$ , the inter-orbital Coulomb interaction  $U' = U_{mm'mm'}$  and the Hund's coupling  $J = U_{mmm'm'} = U_{mm'm'm}$ . Assuming furthermore a full rotational invariance of the orbitals,<sup>2</sup> one obtains so-called Kanamori interactions with  $U' = U - 2J$  [27]. Considering these approximations, one can write down the multi-orbital (Kanamori) Hubbard Hamiltonian as

$$\begin{aligned} \hat{H} = & - \sum_{\substack{\mathbf{R}\mathbf{R}' \\ mm', \sigma}} t_{mm'}(\mathbf{R}, \mathbf{R}') \hat{c}_{\mathbf{R}m\sigma}^\dagger \hat{c}_{\mathbf{R}'m'\sigma} \\ & + U \sum_{\mathbf{R}, m} \hat{n}_{\mathbf{R}m\uparrow} \hat{n}_{\mathbf{R}m\downarrow} + \sum_{\substack{\mathbf{R}, m \neq m' \\ \sigma\sigma'}} (U' - \delta_{\sigma\sigma'} J) \hat{n}_{\mathbf{R}m\sigma} \hat{n}_{\mathbf{R}m'\sigma'} \\ & + J \sum_{\mathbf{R}, m \neq m'} \left( \hat{c}_{\mathbf{R}m\uparrow}^\dagger \hat{c}_{\mathbf{R}m'\downarrow}^\dagger \hat{c}_{\mathbf{R}m\downarrow} \hat{c}_{\mathbf{R}m'\uparrow} + \hat{c}_{\mathbf{R}m\uparrow}^\dagger \hat{c}_{\mathbf{R}m\downarrow}^\dagger \hat{c}_{\mathbf{R}m'\downarrow} \hat{c}_{\mathbf{R}m'\uparrow} + h.c. \right). \end{aligned} \quad (1.17)$$

The first two local interaction terms (second line in Eq. (1.17)) are written in terms of the electron density operator  $\hat{n}_{\mathbf{R}m\sigma} = \hat{c}_{\mathbf{R}m\sigma}^\dagger \hat{c}_{\mathbf{R}m\sigma}$ . They represent the intra-orbital

<sup>2</sup>In a cubic crystal field, the rotational invariance of the orbitals is clearly not fulfilled. However, for 3d orbitals, the deviations from spherically symmetric interactions with  $U' = U - 2J$  are not significant, as shown in Ref. [26].

Coulomb interaction  $U$  of two electrons residing in the same orbital and the inter-orbital Coulomb interaction  $U' - \delta_{\sigma\sigma'}J$  of two electrons in different orbitals. The interaction parameter  $J$  is often referred to as *Hund's coupling*  $J$  as it reflects the well-known Hund's rule which postulates a maximum spin angular momentum for a given electronic configuration. The last two terms in the multi-orbital Hubbard Hamiltonian (last line in Eq. (1.17)) instead cannot be written in terms of density operators  $\hat{n}_{\mathbf{R}m\sigma}$ . They are the so-called spin-flip and pair-hopping terms (for a visualization see Fig. 1.2). As the name suggests, the spin-flip term "flips" the spin of two electrons residing in different orbitals  $m, m'$ . The pair-hopping term instead annihilates a pair of electrons in orbital  $m'$  and transfers them to orbital  $m$ .

The hopping matrix  $t_{mm'}(\mathbf{R}, \mathbf{R}')$ , which is needed in the multi-orbital Hubbard model in Eq. (1.17), is given by Eq. (1.15). Within the DFT+DMFT approach, however, it is obtained from an *ab initio* DFT computation for the material under investigation. Note that only the correlated orbitals are included in the multi-orbital Hubbard model, while DFT computes the whole electronic band-structure of the material. Hence, a projection is needed in order to obtain  $t_{mm'}(\mathbf{R}, \mathbf{R}')$  for the correlated orbital-subspace. This so-called Wannier projection, which will be discussed in the following, constructs localized wave functions  $w_m$  for the correlated orbitals out of the DFT Bloch wave functions and allows to obtain  $t_{mm'}(\mathbf{R}, \mathbf{R}')$  in the basis of localized Wannier functions  $w_m$ .<sup>3</sup>

## 1.4 Wannier projection

Within the DFT+DMFT approach, a Wannier projection is used to construct localized wave functions—the so-called Wannier functions—out of the extended Bloch wave functions used in DFT. These localized Wannier functions are constructed for the correlated orbitals and can then be interpreted as the localized orbitals of the multi-orbital Hubbard model in Eq. (1.17). In the following, I will briefly discuss this Wannier projection, a more detailed derivation and overview can be found in Ref. [28].

Wannier functions were first introduced in 1937 by G. Wannier [29], who suggested to construct localized atomic wave functions by superposing Bloch functions. Since Bloch wave functions of different  $\mathbf{k}$  have different envelope functions  $e^{i\mathbf{k}\mathbf{r}}$  (see e.g. left hand side of Fig. 1.3), one can expect to obtain a localized wave function by superposing them. Thus, in the simplest case of a single isolated band  $n$ , Wannier functions can be

---

<sup>3</sup>The  $t_{mm'}(\mathbf{R}, \mathbf{R}')$  obtained from a DFT computation does not contain only pure electronic hopping, but also some electronic exchange and correlation, which is included in DFT on a mean-field level. This gives rise to the so-called double counting problem, which is discussed in detail in Sec. 1.7.

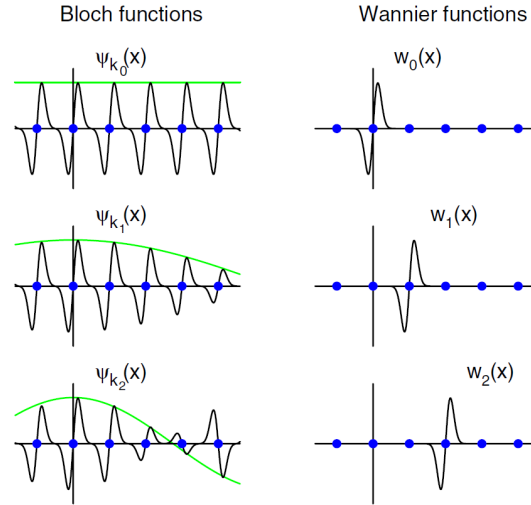


FIGURE 1.3: (Left) Bloch functions for three different wavevectors  $\mathbf{k}$  (green curves represent envelope functions  $e^{i\mathbf{k}\mathbf{R}}$ ). (Right) Localized Wannier functions which are obtained through a superposition of Bloch functions for different  $\mathbf{k}$ , see Eq. (1.18). (Image taken from Ref. [28])

constructed according to

$$w_{n\mathbf{R}}(\mathbf{r}) = \int_{\text{BZ}} d^3k e^{-i\mathbf{k}\mathbf{R}} \psi_{n\mathbf{k}}(\mathbf{r}), \quad (1.18)$$

where the integral goes over all  $\mathbf{k}$  in the first Brillouin zone.  $\mathbf{R}$  is a real-space lattice vector and Wannier functions at different  $\mathbf{R}$  are images of one another (see right hand side of Fig. 1.3).

The Wannier functions  $w_{n\mathbf{R}}(\mathbf{r})$  form an orthogonal set and Eq. (1.18) has the form of a Fourier transform. Its inverse transform, up to a renormalization factor, is

$$\psi_{n\mathbf{k}}(\mathbf{r}) = \sum_{\mathbf{R}} e^{i\mathbf{k}\mathbf{R}} w_{n\mathbf{R}}(\mathbf{r}). \quad (1.19)$$

Thus, the Bloch functions  $\psi_{n\mathbf{k}}(\mathbf{r})$  can be expanded in terms of Wannier functions  $w_{n\mathbf{R}}(\mathbf{r})$ , and vice versa. Both sets of wave functions span the same band-space and the transformation between them is, in principle, just a basis transformation. However, it should be noted that, unlike Bloch functions, Wannier functions are not eigenstates of the Kohn-Sham-Hamiltonian. Thus, in some sense one pays for the localization in real space with de-localization in energy.

The basis transformation between Bloch and Wannier functions in Eqs. (1.18) and (1.19) is unitary, but not unique. In fact, there exists a "gauge freedom" in the definition of the Bloch functions  $\psi_{n\mathbf{k}}(\mathbf{r})$  and one can replace

$$\tilde{\psi}_{n\mathbf{k}}(\mathbf{r}) = e^{i\phi_n(\mathbf{k})} \psi_{n\mathbf{k}}(\mathbf{r}), \quad (1.20)$$

without changing the physical description of the system. Here  $\phi_n(\mathbf{k})$  is a real function, that is periodic in  $\mathbf{k}$ -space. The "gauge freedom" in Eq. (1.20) propagates into the Wannier functions, meaning that different choices of  $\phi_n(\mathbf{k})$  result in different Wannier functions with different shapes and spreads. Thus, the construction of Wannier functions carries a degree of arbitrariness which can be used to construct e.g. maximally localized Wannier functions.

**Multi-orbital Wannier functions** So far, we implicitly assumed that we have a single isolated band with band index  $n$ . But in the band-structure of a realistic material one usually has a manifold of bands that overlap and hybridize with each other. Let us assume that the Bloch bands, which are included in the Wannier projection, form a manifold of  $L$  bands which are separated from any other bands outside the manifold.<sup>4</sup> In this case, the "gauge transformation" in Eq. (1.20) can be generalized to

$$\tilde{\psi}_{m\mathbf{k}}(\mathbf{r}) = \sum_{n=1}^L U_{mn}^{\mathbf{k}} \psi_{n\mathbf{k}}(\mathbf{r}), \quad (1.21)$$

where  $U_{mn}^{\mathbf{k}}$  is a unitary matrix of dimension  $L$ . The construction of the Wannier functions now allows for an additional mixing of the Bloch states according to

$$w_{m\mathbf{R}}(\mathbf{r}) = \int_{\text{BZ}} d^3k e^{-i\mathbf{k}\mathbf{R}} \sum_{n=1}^L U_{mn}^{\mathbf{k}} \psi_{n\mathbf{k}}(\mathbf{r}). \quad (1.22)$$

In this multi-band case, the unitary matrix  $U_{mn}^{\mathbf{k}}$  now carries the gauge freedom of the Wannier projection. It can e.g. be chosen in a way that maximally localized Wannier functions are obtained.

**Maximally localized Wannier functions** A localization criterion for maximally localized Wannier functions was introduced in 1997 by Marzari and Vanderbilt [30]. They proposed the functional

$$\Omega = \sum_m [\langle w_{m\mathbf{R}} | r^2 | w_{m\mathbf{R}} \rangle - |\langle w_{m\mathbf{R}} | \mathbf{r} | w_{m\mathbf{R}} \rangle|^2], \quad (1.23)$$

which gives a measure of the total spread of all  $L$  Wannier functions in real space.

---

<sup>4</sup>If the bands of interest overlap and hybridize with other bands which extend further out in energy, it is not easily possible to define a manifold of  $L$  bands for the Wannier projection. However, also in this case of *entangled* bands a Wannier projection is possible. The procedure then basically consists of two-steps: first a suitable  $L$ -dimensional band-subspace needs to be selected for each  $\mathbf{k}$  and then Wannier functions can be constructed. For more details regarding this *disentanglement* procedure see Ref. [28].

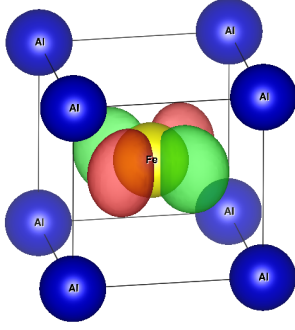


FIGURE 1.4: Maximally localized Fe  $t_{2g}$  Wannier orbital in FeAl.

In order to obtain maximally localized Wannier functions, the functional in Eq. (1.23) needs to be minimized with respect to the unitary transformations  $U^{\mathbf{k}}$  appearing in Eq. (1.22). In practice, this is done in an iterative procedure by starting from an initial projection and then varying  $U^{\mathbf{k}}$ . Recently, also "selectively localized" Wannier functions have been proposed in Ref. [31], where not the total spread of all  $L$  Wannier functions, but the spread of a subset of chosen Wannier functions is minimized. This slight variation of the mini-

mization criterion can lead to improvements for projections including a large number of Wannier functions, where some of them are expected to have a less localized orbital character than others.

**Wannier Hamiltonian** As mentioned already, a Wannier projection can provide *ab initio* values for the hopping matrix  $t_{mm'}$  in the multi-orbital Hubbard model in Eq. (1.17). Starting from a standard DFT computation, the correlated bands and thus the band-subspace  $L$  for the Wannier projection needs to be identified. These correlated bands are usually partially filled  $3d$  or  $4f$  bands close to the Fermi energy. Thus, it is useful to divide the Kohn-Sham Hamiltonian in the Bloch basis obtained from a DFT computation into submatrices

$$\begin{bmatrix} E_b^{\mathbf{k}} & 0 & 0 \\ 0 & E^{\mathbf{k}} & 0 \\ 0 & 0 & E_a^{\mathbf{k}} \end{bmatrix}, \quad (1.24)$$

where  $E^{\mathbf{k}}$  spans the correlated band subspace  $L$  we are interested in. The Hamiltonian  $E^{\mathbf{k}}$  in the Bloch basis (of course also  $E_a^{\mathbf{k}}$  and  $E_b^{\mathbf{k}}$ ) is diagonal  $E_{nm}^{\mathbf{k}} = \delta_{nm}\epsilon_{n\mathbf{k}}$ , with  $\epsilon_{n\mathbf{k}}$  being the Kohn-Sham eigenenergies. Wannier functions are now constructed only from the bands included in  $E^{\mathbf{k}}$ . When the Wannier projection is completed,  $E^{\mathbf{k}}$  can be rewritten in the basis of maximally localized Wannier functions. This is achieved through a simple basis transformation

$$H_W^{\mathbf{k}} = U^{\mathbf{k}} E^{\mathbf{k}} (U^{\mathbf{k}})^{\dagger}, \quad (1.25)$$

where  $U^{\mathbf{k}}$  are the unitary matrices obtained from the Wannier projection in Eq. (1.22). Thus, the Wannier Hamiltonian  $H_W^{\mathbf{k}}$  is simply the low energy part of the DFT Hamiltonian  $E^{\mathbf{k}}$  written in the basis of localized Wannier functions.  $H_W^{\mathbf{k}}$  is then used as *ab*

*initio* input for the single-electron part of the multi-orbital Hubbard model in Eq. (1.17). With the Fourier transform

$$H_W^{\mathbf{R}-\mathbf{R}'} = \sum_{\mathbf{k}} e^{i\mathbf{k}(\mathbf{R}-\mathbf{R}')} H_W^{\mathbf{k}}, \quad (1.26)$$

the multi-orbital Hubbard model in Eq. (1.17) can be rewritten as

$$\begin{aligned} \hat{H} = & \sum_{\substack{\mathbf{R}, \mathbf{R}' \\ mm', \sigma}} H_W^{\mathbf{R}-\mathbf{R}'} \hat{c}_{\mathbf{R}m\sigma}^\dagger \hat{c}_{\mathbf{R}'m'\sigma} \\ & + U \sum_{\mathbf{R}, m} \hat{n}_{\mathbf{R}m\uparrow} \hat{n}_{\mathbf{R}m\downarrow} + \sum_{\substack{\mathbf{R}, m \neq m' \\ \sigma \sigma'}} (U' - \delta_{\sigma\sigma'} J) \hat{n}_{\mathbf{R}m\sigma} \hat{n}_{\mathbf{R}m'\sigma'} \\ & + J \sum_{\mathbf{R}, m \neq m'} \left( \hat{c}_{\mathbf{R}m\uparrow}^\dagger \hat{c}_{\mathbf{R}m'\downarrow}^\dagger \hat{c}_{\mathbf{R}m\downarrow} \hat{c}_{\mathbf{R}m'\uparrow} + \hat{c}_{\mathbf{R}m\uparrow}^\dagger \hat{c}_{\mathbf{R}m\downarrow}^\dagger \hat{c}_{\mathbf{R}m'\downarrow} \hat{c}_{\mathbf{R}m'\uparrow} + h.c. \right) + \hat{H}_{dc}. \end{aligned} \quad (1.27)$$

Thus, the Wannier Hamiltonian  $H_W^{\mathbf{R}-\mathbf{R}'}$  acts as the hopping matrix  $t_{mm'}(\mathbf{R}, \mathbf{R}')$  in the original Hubbard model. However,  $H_W^{\mathbf{R}-\mathbf{R}'}$  does not contain only pure hopping terms, but also some electronic exchange and correlation included already in DFT. In order to avoid any double counting of electronic correlations, the so-called "double-counting" term  $\hat{H}_{dc}$  in Eq. (1.27) arises. This double-counting issue will be discussed in more detail in Sec. 1.7. Now I first focus on the *ab initio* computation of the interaction values  $U$ ,  $J$  and  $U'$ .

## 1.5 *Ab initio* computation of the Coulomb interaction

In the DFT+DMFT approach, the Hubbard interaction parameters  $U$ ,  $J$  and  $U'$  for the multi-orbital Hubbard model in Eq. (1.27) can be extracted from an *ab initio* DFT computation. However, the straightforward use of Eq. (1.16) usually leads to much too large values for the interaction parameters. This is the case because Eq. (1.16) uses the bare Coulomb interaction  $V = \frac{e^2}{|\mathbf{r}-\mathbf{r}'|}$  without considering any screening effects. Instead, the Coulomb interaction in the multi-orbital Hubbard model, which usually contains only a few correlated bands, is screened by mobile electrons residing in other bands of the material under investigation. These screening processes stemming from electrons in bands not included in the Wannier projection need to be considered when computing the interaction parameters  $U$ ,  $J$  and  $U'$ .

**Screening of the Coulomb interaction** A method to take into account electronic screening processes, is the random phase approximation (RPA) [32, 33]. In RPA, the

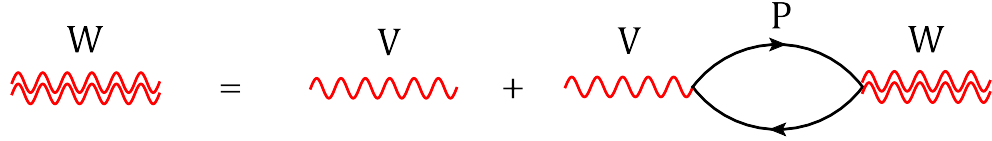


FIGURE 1.5: Screening of the Coulomb interaction within RPA. The double wiggled lines represent the screened Coulomb interaction  $W$  while single wiggled lines denote the bare Coulomb interaction  $V$ .

screened Coulomb interaction  $W$  is defined via a Dyson-like equation, which schematically reads

$$W = V + VPW, \quad (1.28)$$

leading to

$$W = \frac{V}{1 - PV}, \quad (1.29)$$

with the bare Coulomb interaction  $V = \frac{e^2}{|\mathbf{r} - \mathbf{r}'|}$  and the polarisation  $P$ . In principle, the latter contains all possible electronic screening processes, which in terms of diagrams means all possible two-particle diagrams including vertex corrections. However, in RPA one limits oneself to the lowest-order two-particle diagram, the so-called bubble diagram. Fig. 1.5 shows how in RPA the bare Coulomb interaction  $V$  is screened according to Eq. (1.28) with the bubble diagram being the only diagram contributing to the polarisation  $P$ . The bubble diagram describes an electron-hole pair and is mathematically simply the product of two Green's functions. Thus, the polarisation in RPA is

$$P(\mathbf{r}, \mathbf{r}', \omega) = -i \int \frac{d\omega'}{2\pi} G(\mathbf{r}, \mathbf{r}', \omega + \omega') G(\mathbf{r}', \mathbf{r}, \omega'). \quad (1.30)$$

By using the Kohn-Sham wave functions  $\psi_{n\mathbf{k}}$  and energies  $\epsilon_{n\mathbf{k}}$ , the polarisation  $P$  can be rewritten as [34]

$$P(\mathbf{r}, \mathbf{r}', \omega) = \sum_{n\mathbf{k}}^{\text{occ}} \sum_{n'\mathbf{k}'}^{\text{unocc}} \left[ \frac{\psi_{n\mathbf{k}}^*(\mathbf{r}) \psi_{n'\mathbf{k}'}(\mathbf{r}) \psi_{n'\mathbf{k}'}^*(\mathbf{r}') \psi_{n\mathbf{k}}(\mathbf{r}')}{\omega - \epsilon_{n'\mathbf{k}'} + \epsilon_{n\mathbf{k}} + i\delta} - \frac{\psi_{n\mathbf{k}}(\mathbf{r}) \psi_{n'\mathbf{k}'}^*(\mathbf{r}) \psi_{n'\mathbf{k}'}(\mathbf{r}') \psi_{n\mathbf{k}}^*(\mathbf{r}')}{\omega + \epsilon_{n'\mathbf{k}'} - \epsilon_{n\mathbf{k}} - i\delta} \right], \quad (1.31)$$

where  $\psi_{n\mathbf{k}}, \epsilon_{n\mathbf{k}}$  refer to occupied, while  $\psi_{n'\mathbf{k}'}, \epsilon_{n'\mathbf{k}'}$  to unoccupied states; and the polarisation  $P$  describes electronic excitations from occupied to unoccupied states.

**Constrained random phase approximation (cRPA)** In cRPA [24, 35, 36], one separates the total polarisation  $P$  into the polarisation  $P_d$  within the correlated target bands included in the Wannier Hamiltonian  $H_W^{\mathbf{k}}$  and the rest of the polarisation  $P_r$ .

$$P = P_d + P_r. \quad (1.32)$$

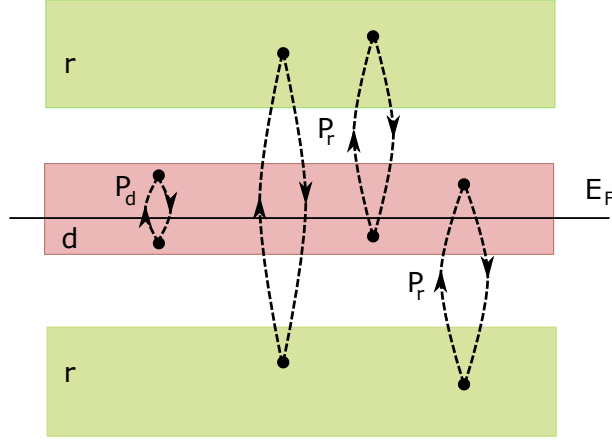


FIGURE 1.6: Schematic picture showing the polarisations  $P_d$  and  $P_r$  within cRPA.  $P_d$  is constrained to electronic transitions within the  $d$  subspace while  $P_r$  contains all other possible electronic transitions, e.g. between the  $r$  and the  $d$  subspace.

The polarisation within the target bands is denoted as  $P_d$  since the correlated bands have usually  $d$  character.  $P_d$  contains electronic transitions within the  $d$  subspace while  $P_r$  includes all other transitions, e.g. from  $d$  to  $r$  (for a visualization see Fig. 1.6). Since the effective Coulomb interaction in the DFT+DMFT Hubbard model should be screened by all polarisations excluding the ones within the  $d$  subspace, we are interested in computing  $P_r$ . Then, the partially screened Coulomb interaction  $W_r$  can be obtained through

$$W_r = \frac{V}{1 - P_r V} . \quad (1.33)$$

Please note that  $P(\mathbf{r}, \mathbf{r}', \omega)$  depends on  $\omega$  and this frequency dependence propagates into the screened Coulomb interaction  $W_r(\mathbf{r}, \mathbf{r}', \omega)$ . Thus, due to the energy-dependent screening, the screened Coulomb interaction becomes frequency-dependent. At high energies, screening processes become less efficient and above the plasma frequency  $\omega_p$  the screened Coulomb interaction recovers its unscreened value  $V$ . Practically,  $P_r$  is usually obtained by first computing the total polarisation  $P$  and the polarisation  $P_d$  within the target  $d$  bands [Eq. (1.31) can equally be used to compute  $P_d$  by simply limiting the Kohn-Sham states to states within the  $d$  subspace]. Then  $P_r$  is obtained by  $P_r = P - P_d$ .<sup>5</sup>

After obtaining the partially screened Coulomb interaction  $W_r(\mathbf{r}, \mathbf{r}', \omega)$  within cRPA, its matrix elements in the localized Wannier basis can be computed [35]. For this purpose we can use Eq. (1.16), but with the partially screened Coulomb interaction  $W_r(\mathbf{r}, \mathbf{r}', \omega)$

<sup>5</sup>In the case of entangled bands, the subspaces  $d$  and  $r$  cannot strictly be separated from each other. However, also in this case it is possible to compute the partially screened Coulomb interaction  $W_r(\mathbf{r}, \mathbf{r}', \omega)$  consistently with the disentanglement procedure of the Wannier projection. For more details see Refs. [34, 35].



instead of the bare one  $V = \frac{e^2}{|\mathbf{r}-\mathbf{r}'|}$ . This yields

$$U_{lm'ml'}(\mathbf{R}, \mathbf{R}, \mathbf{0}, \mathbf{0}, \omega) = \int d^3r d^3r' w_{m'\mathbf{0}}^*(\mathbf{r}) w_{l'\mathbf{R}}^*(\mathbf{r}') W_r(\mathbf{r}, \mathbf{r}', \omega) w_{m\mathbf{R}}(\mathbf{r}') w_{l'\mathbf{0}}(\mathbf{r}), \quad (1.34)$$

where  $w_{m'\mathbf{R}}$  is the Wannier function of orbital  $m'$  at lattice site  $\mathbf{R}$ . Please note that  $U_{lm'ml'}(\mathbf{R}, \mathbf{R}, \mathbf{0}, \mathbf{0}, \omega)$  explicitly depends on  $\mathbf{R}$  and the frequency  $\omega$ . The latter is due to the fact that the screening processes are  $\omega$ -dependent. However, in many DFT+DMFT studies including the ones presented in this work, the frequency dependence of the Coulomb interaction is neglected by simply taking its value at  $\omega = 0$ . Thus, the local and frequency-independent Hubbard interaction parameters  $U_{lm'ml'}$ , which are used in the multi-orbital Hubbard model, are calculated by setting  $\mathbf{R} = \mathbf{0}$  and  $\omega = 0$  in Eq. (1.34). From  $U_{lm'ml'}$ , the interaction parameters  $U$ ,  $J$  and  $U'$ —used in the multi-orbital Kanamori Hubbard model in Eq. (1.17)—can then simply be obtained as already described in Sec. 1.3. For the non-local Coulomb interaction  $V^{\mathbf{q}}$  instead, which is used in AbinitioDFA [see Eq. (4.26)], one needs to keep the  $\mathbf{R}$ -dependence in Eq. (1.34).

## 1.6 Dynamical mean-field theory (DMFT)

As discussed so far, one can set up a multi-orbital Hubbard model with *ab initio* DFT input. That is, the single-electron part—namely the Wannier Hamiltonian  $H_W^{\mathbf{R}-\mathbf{R}'}$ —in the Hubbard model in Eq. (1.27) can be obtained through a Wannier projection, while the local Coulomb interaction parameters  $U$ ,  $J$  and  $U'$  are calculated from cRPA. However, it is still not possible to solve the multi-orbital Hubbard model. Even for the single-orbital Hubbard model,<sup>6</sup> which includes only one intra-orbital Coulomb interaction term  $U$ ,

$$\hat{H} = -t \sum_{\langle \mathbf{R}\mathbf{R}' \rangle, \sigma} \hat{c}_{\mathbf{R}\sigma}^\dagger \hat{c}_{\mathbf{R}'\sigma} + U \sum_{\mathbf{R}} \hat{n}_{\mathbf{R}\uparrow} \hat{n}_{\mathbf{R}\downarrow}, \quad (1.35)$$

no solution exists, neither analytically nor numerically.<sup>7</sup> The difficulties arise from the fact that the kinetic energy and the Coulomb interaction term are diagonal in different bases: the hopping term  $t$  is diagonal in momentum space, while the local Coulomb interaction term  $U$  is diagonal in real space (it acts only on electrons residing on the same lattice site). It is exactly this competition between itineracy and localization of the electrons, which lies at the heart of the Hubbard model and makes its solution so

<sup>6</sup>For simplicity, I restrict the discussion in this section to the single-orbital Hubbard model with nearest-neighbor hopping  $t$  [denoted by  $\langle \mathbf{R}\mathbf{R}' \rangle$  in Eq. (1.35)]. However, please note that all statements and results in the following also apply to the multi-orbital case.

<sup>7</sup>However, there exists a solution in dimensions  $d = 1$  or  $d \rightarrow \infty$ , and for other simplifying limits such as  $U \rightarrow \infty$  [37].

difficult. Thus, further approximations are needed in order to make the Hubbard model treatable. At this point the dynamical mean-field theory (DMFT) comes into play.

DMFT maps the Hubbard model self-consistently onto an auxiliary single-site impurity model [6], which is way easier to treat than the full lattice problem. This mapping has been shown to be exact in infinite dimensions or infinite coordination number [5], while it is clearly an approximation in three or lower dimensions. As its name suggests, DMFT is a mean-field theory which performs a spatial average by treating the surrounding of the auxiliary impurity site as a mean-field. However, in contrast to classical mean-field approaches (e.g. the one for the Ising model), DMFT keeps the time-dependence of the mean-field—it is a *dynamical* mean-field theory. Since DMFT is a diagrammatic method, I will now first briefly introduce Green’s functions and Feynman diagrams. Then, in Sec. 1.6.2 and 1.6.3 the diagrammatic content of DMFT and the mapping onto an auxiliary Anderson impurity model will be discussed.

### 1.6.1 Green’s functions and Feynman diagrams

In DMFT and other many-body approaches, one does not directly approximate the many-electron wave function, but rather works with Green’s functions. The one-particle Green’s function describes the propagation of an electron/hole in an interacting many-body system. It is defined as<sup>8</sup>

$$G_{\sigma}(\tau, \mathbf{r}, \tau', \mathbf{r}') = -\langle \mathcal{T} [\hat{c}_{\sigma}(\tau, \mathbf{r}) \hat{c}_{\sigma}^{\dagger}(\tau', \mathbf{r}') ] \rangle, \quad (1.36)$$

where  $\hat{c}_{\sigma}^{(\dagger)}$  are fermionic creation (annihilation) operators and  $\mathcal{T}$  is the time ordering operator. If  $\tau > \tau'$ , the Green’s function in Eq. (1.36) describes the creation of an electron at position  $\mathbf{r}'$  and (imaginary) time  $\tau'$ ; this electron then propagates through the system and is annihilated later on at time  $\tau$  and position  $\mathbf{r}$ .<sup>9</sup> Thus, the Green’s function describes the process of probing an interacting many-body system with an additional particle. In fact, it is closely related to experiment, where solid state systems are usually probed by applying an external perturbation, e.g. photons in angular-resolved photoemission spectroscopy (ARPES).

Since we are dealing with systems in thermal equilibrium, Eq. (1.36) has already been adopted to the Matsubara formalism with imaginary time  $\tau \in [0, \beta)$  (with the inverse

---

<sup>8</sup>The definition of the Green’s function can easily be extended to two and more particles. The two-particle Green’s function, which describes the propagation of two electrons/holes in the system, will play a prominent role in this thesis and will be introduced in detail in Sec. 3.2.1. Here, however, for simplicity the discussion is limited to the one-particle Green’s function.

<sup>9</sup>If  $\tau < \tau'$ , the Green’s function in Eq. (1.36) describes the propagation of a hole. Please also note that the electrons in the system are indistinguishable particles and one can in principle not say that the particle which is extracted is the same as the one which was inserted.



FIGURE 1.7: Basic diagrammatic elements for constructing the Feynman diagrams of the Hubbard model: (left) the non-interacting Green's function  $G_0$  and (right) the local Coulomb interaction  $U$ .

temperature  $\beta = 1/T$ ). The concept of imaginary time and frequency is a mathematical construct, whose advantage can be seen by considering the field operators in their Heisenberg representation

$$\hat{c}_\sigma^{(\dagger)}(\tau, \mathbf{r}) = e^{\tau \hat{H}} \hat{c}_\sigma^{(\dagger)}(\mathbf{r}) e^{-\tau \hat{H}} \quad \hat{c}_\sigma^{(\dagger)}(t, \mathbf{r}) = e^{it \hat{H}} \hat{c}_\sigma^{(\dagger)}(\mathbf{r}) e^{-it \hat{H}}, \quad (1.37)$$

and recalling that the thermal expectation value  $\langle \dots \rangle$  is performed according to

$$\langle \dots \rangle = \frac{1}{Z} \text{Tr} \left( e^{-\beta \hat{H}} \dots \right), \quad (1.38)$$

where  $Z = \text{Tr} \left( e^{-\beta \hat{H}} \right)$ . Thus, by using imaginary time  $\tau$ , the exponential functions in Eqs. (1.37) and (1.38) can be subsumed in a single imaginary time integration, which is very useful e.g. for any perturbative expansion.

However, the Green's function of the Hubbard model cannot directly be calculated since the trace in the definition of the Green's function goes over the unknown states of the interacting many-particle system. So, what one usually does and what leads to the formalism of Feynman diagrams, is a perturbative expansion in the interacting part of the Hamiltonian. In fact, the Hubbard Hamiltonian in Eq. (1.35) can be divided into a non-interacting part  $\hat{H}_0$ , which is represented by the kinetic energy term, and a many-body interaction part  $\hat{H}_I$  represented by the Coulomb interaction term. For the latter the perturbative expansion is performed. A detailed derivation of the perturbative expansion and the formalism of Feynman diagrams can e.g. be found in Refs. [21, 22]. Here I just would like to summarize that the basic elements of the perturbative expansion of the Hubbard model, which are at the same time the basic ingredients for its Feynman diagrams, are the Green's function of the non-interacting system  $G_0$  and the local Coulomb interaction  $U$ . These two basic ingredients are depicted diagrammatically in Fig. 1.7. They can be used to construct all possible diagrams, following the Feynman rules. Two possible diagrams are e.g. shown in Fig. 1.9.

**Dyson equation** The non-interacting Green's function  $G_0$  is dressed with all possible diagrams, leading to the full interacting Green's functions  $G$  of Eq. (1.36). This process is described by the so-called Dyson-equation, which is depicted in Fig. 1.8. There, the

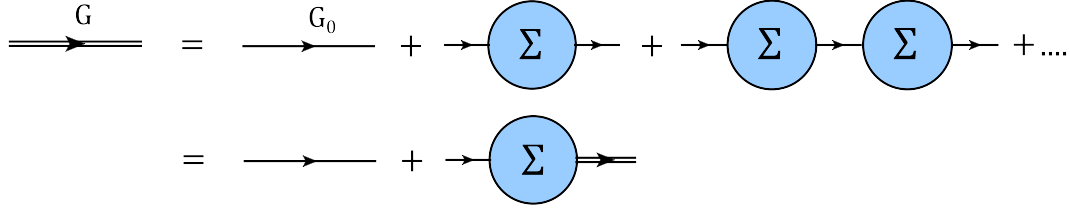


FIGURE 1.8: Diagrammatic representation of the Dyson equation: the non-interacting Green's function  $G_0$  (single line) is dressed with the self-energy  $\Sigma$ , giving the full, interacting Green's function  $G$  (double line).

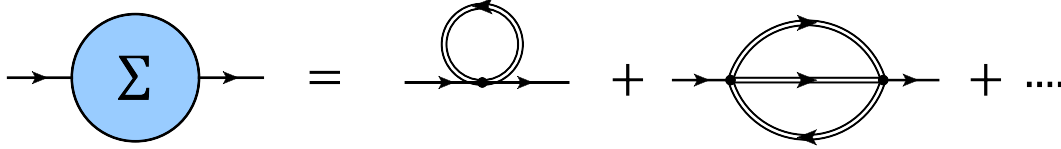


FIGURE 1.9: The self-energy contains all irreducible, skeleton Feynman diagrams. Please note that the internal Green's function lines composing the self-energy diagrams in this skeleton expansion are interacting Green's functions (double lines).

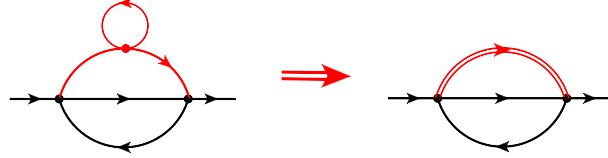


FIGURE 1.10: The (left) non-skeleton diagram is included in the (right) skeleton diagram through the interacting internal Green's function line (double line).

quantity  $\Sigma$  is the self-energy which—expressed in terms of  $G$ —contains all irreducible, skeleton Feynman diagrams. Skeleton diagrams are diagrams which do not contain any self-energy inclusions. Irreducible, on the other hand, means that one cannot split the Feynman diagram into two parts by cutting one internal fermionic line. The reducible Feynman diagrams are generated instead through the Dyson equation which is depicted diagrammatically in Fig. 1.8 and reads

$$\begin{aligned}
 G &= G_0 + G_0 \Sigma G_0 + G_0 \Sigma G_0 \Sigma G_0 + \dots \\
 &= G_0 + G_0 \Sigma (G_0 + G_0 \Sigma G_0 + \dots) \\
 &= G_0 + G_0 \Sigma G.
 \end{aligned} \tag{1.39}$$

So the full, interacting Green's function  $G$  can be obtained from the non-interacting one  $G_0$  and the self-energy  $\Sigma$  via  $G = \frac{1}{G_0^{-1} - \Sigma}$ .

In  $\mathbf{k}$ -space, the non-interacting Green's function can explicitly be written as

$$G_0(i\nu, \mathbf{k}) = \frac{1}{i\nu + \mu - \epsilon_{\mathbf{k}}}, \tag{1.40}$$

with  $i\nu$  being fermionic Matsubara frequencies  $i\nu = \frac{i(2n+1)\pi}{\beta}$ ,  $\mu$  the chemical potential

and  $\epsilon_{\mathbf{k}}$  the energy eigenvalues of the non-interacting problem. Consequently, the full interacting Green's function can simply be written as

$$G(i\nu, \mathbf{k}) = \frac{1}{i\nu + \mu - \epsilon_{\mathbf{k}} - \Sigma(i\nu, \mathbf{k})} . \quad (1.41)$$

Thus, all the information beyond the non-interacting problem is basically contained in the self-energy.

Of course, it is not possible to calculate the self-energy of the Hubbard model exactly by summing over all possible Feynman diagrams. However, the perturbative expansion in the form of Feynman diagrams provides an insight into the involved physical processes. Furthermore, it makes it possible to develop approximations which include only certain diagrams. In a classical perturbative approach, for example, one would include only the lowest-order diagrams. In DMFT instead, a whole class of diagrams is included up to all orders, i.e. in a non-perturbative way. In fact, DMFT includes all local, irreducible Feynman diagrams, as discussed in more detail in the following Sec. 1.6.2. One clear advantage of a diagrammatic approach like DMFT is the fact that its diagrammatic content is well-defined and thus it is clear which physical processes it can describe.

### 1.6.2 Diagrammatic content of DMFT

The DMFT self-energy contains all local, irreducible one-particle Feynman diagrams. One can understand this diagrammatic content from the fact that DMFT provides the exact solution for the Hubbard model in infinite dimensions or, equivalently, for infinite coordination number. Thus, to derive the DMFT we follow Ref. [38] and explicitly consider this limit. Let us start with the expectation value of the kinetic energy part in the Hubbard model in Eq. (1.35)

$$\langle \hat{H}_{kin} \rangle = -t \sum_{\langle \mathbf{R}, \mathbf{R}' \rangle, \sigma} \langle \hat{c}_{\mathbf{R}'\sigma}^\dagger \hat{c}_{\mathbf{R}\sigma} \rangle, \quad (1.42)$$

where  $\langle \mathbf{R}, \mathbf{R}' \rangle$  stands for a summation over nearest neighbors and the probability for an electron to hop from lattice site  $\mathbf{R}$  to  $\mathbf{R}'$  is given by  $|t|^2$ . The probability  $|t|^2$  obviously needs to add up to a value  $\mathcal{O}(1)$  when summed over all nearest neighbors. Thus, by increasing the coordination number  $z$  (the number of nearest neighbors) the hopping amplitude  $t$  needs to be rescaled in order to prevent the kinetic energy term from diverging. The Hubbard interaction term instead does not need any rescaling since it is purely local and thus independent of  $z$ . In 1989, Metzner and Vollhardt [5] have shown that the only scaling, for which the physics of the Hubbard model remains non-trivial in the case of infinite coordination number, is  $t \propto \frac{1}{\sqrt{z}}$ . This way, also the propagator scales

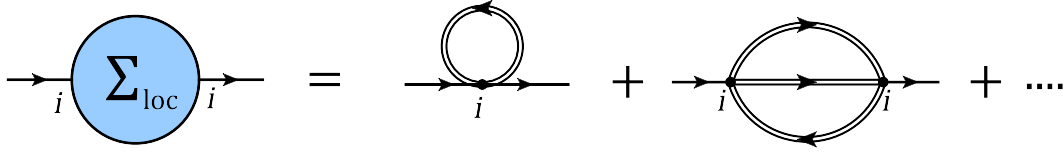


FIGURE 1.11: The DMFT self-energy contains all local irreducible Feynman diagrams. (Dots represent the bare Hubbard interaction  $U$  and  $i$  is a lattice site index.)

like  $\langle \hat{c}_{\mathbf{R}'\sigma}^\dagger \hat{c}_{\mathbf{R}\sigma} \rangle \propto \frac{1}{\sqrt{z}}$  and it can be shown that the self-energy becomes purely local [5], or equivalently, momentum-independent

$$\Sigma(i\nu, \mathbf{k}) \rightarrow \Sigma(i\nu). \quad (1.43)$$

Thus, the DMFT self-energy becomes purely local and contains all local, irreducible one-particle Feynman diagrams (see Fig. 1.11 where  $i$  is a lattice site index). These local diagrams capture all local electronic correlations in a non-perturbative way so that DMFT can e.g. account for local spin fluctuations.

### 1.6.3 Mapping onto an Anderson impurity model

One key to the success of DMFT lies in its mapping of the Hubbard model onto a single-site Anderson impurity model (AIM). Such a mapping is possible since the same local Feynman diagrams, which constitute the DMFT self-energy, can also be obtained from an AIM. This was realized in 1992 by Georges and Kotliar [6], who proposed a self-consistent mapping of the local DMFT Green's function on the Green's function of an AIM.

The Hamiltonian of the AIM describes an interacting impurity hybridizing with a bath of non-interacting electrons. In second quantization it reads

$$\hat{H} = \sum_{\mathbf{k}\sigma} \epsilon_{\mathbf{k}} a_{\mathbf{k}\sigma}^\dagger a_{\mathbf{k}\sigma} + \sum_{\mathbf{k}\sigma} V_{\mathbf{k}} \left( a_{\mathbf{k}\sigma}^\dagger c_\sigma + c_\sigma^\dagger a_{\mathbf{k}\sigma} \right) + U n_\uparrow n_\downarrow, \quad (1.44)$$

where  $a_{\mathbf{k}\sigma}^\dagger$  ( $a_{\mathbf{k}\sigma}$ ) are creation (annihilation) operators of non-interacting bath electrons with energy  $\epsilon_{\mathbf{k}}$  (for simplicity we assume that there exists only one band in the bath).  $c_\sigma^\dagger$  ( $c_\sigma$ ) instead create (annihilate) electrons at the interacting impurity site, and  $n_\sigma = c_\sigma^\dagger c_\sigma$ .  $V_{\mathbf{k}}$  quantifies the hybridization strength between the bath and the impurity, while  $U$  is the purely local Coulomb interaction between the localized electrons at the impurity site.

If the AIM is solved by quantum Monte Carlo simulations, which is the method of choice in this work, one usually switches to an action formalism. Then one can integrate out

the bath and arrive at a retarded interaction on the impurity, which can be described by a frequency-dependent, non-interacting Green's function  $\mathcal{G}^0(i\nu)$ . Given  $\mathcal{G}^0(i\nu)$ , the interacting Green's function of the Anderson impurity model  $G_{\text{AIM}}(i\nu)$  can be obtained via a multi-dimensional path integral of Grassmann variables  $\psi$  and  $\psi^\dagger$  [39]

$$G_{\text{AIM}}(i\nu) = -\frac{1}{Z} \int \mathcal{D}[\psi] \mathcal{D}[\psi^\dagger] \psi \psi^\dagger e^{\mathcal{A}[\psi, \psi^\dagger, (\mathcal{G}^0)^{-1}]}, \quad (1.45)$$

with the partition function  $Z$  and the action  $\mathcal{A}$

$$\begin{aligned} Z &= \int \mathcal{D}[\psi] \mathcal{D}[\psi^\dagger] e^{\mathcal{A}[\psi, \psi^\dagger, (\mathcal{G}^0)^{-1}]}, \\ \mathcal{A} &= \sum_{\sigma m} \psi_\sigma(i\nu) \mathcal{G}^0(i\nu)^{-1} \psi_\sigma^\dagger(i\nu) - U \sum_{\sigma\sigma'} \int_0^\beta d\tau \psi_\sigma^\dagger(\tau) \psi_{\sigma'}^\dagger(\tau) \psi_{\sigma'}(\tau) \psi_\sigma(\tau). \end{aligned} \quad (1.46)$$

Due to the high dimensionality of the fermionic configuration space, the integrals are evaluated stochastically by a Monte Carlo algorithm. The Hirsch-Fye quantum Monte Carlo (HF-QMC) [40] is based on a time discretization  $\Delta\tau$  of the integrals, which leads to a systematic error requiring an extrapolation  $\Delta\tau \rightarrow 0$ . The continuous-time quantum Monte-Carlo algorithm [41, 42], which is used in this work, instead avoids this time discretization error and also allows for computations at lower temperatures than HF-QMC.

**DMFT self-consistency cycle** As already mentioned, one can formulate a self-consistent scheme to determine the appropriate AIM which describes the respective Hubbard model in infinite dimensions. This self-consistent DMFT loop is depicted in Fig. 1.12 and is briefly described in the following.

One starts with a trial self-energy  $\Sigma(i\nu)$ , which might just be zero. This local self-energy  $\Sigma(i\nu)$ , which in the end—when self-consistency is reached—will be the DMFT self-energy, is used as an approximation for the full self-energy of the Hubbard model  $\Sigma(\nu, \mathbf{k})$ . Thus, the Green's function of the Hubbard model is computed as

$$G(i\nu, \mathbf{k}) = \frac{1}{i\nu + \mu - \epsilon_{\mathbf{k}} - \Sigma(i\nu)}, \quad (1.47)$$

with  $\mu$  being the chemical potential and  $\epsilon_{\mathbf{k}}$  the energies obtained from a DFT computation.<sup>10</sup>

Then the Hubbard model is mapped onto an Anderson impurity model by computing the local,  $\mathbf{k}$ -summed Green's function  $G(i\nu) = \sum_{\mathbf{k}} G(i\nu, \mathbf{k})$  and defining the non-interacting

<sup>10</sup>In the multi-orbital case,  $\epsilon_{\mathbf{k}}$  is replaced by the Wannier Hamiltonian  $H_W^{\mathbf{k}}$  of Eq. (1.25) and  $\Sigma(i\nu)$  becomes a matrix in the orbital degrees of freedom.

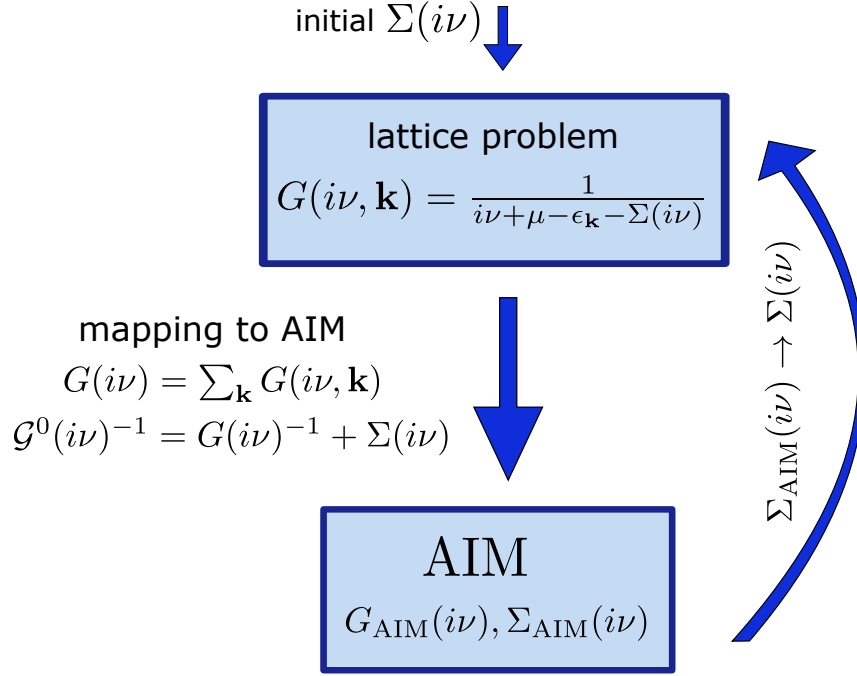


FIGURE 1.12: Schematic flow diagram of the DMFT algorithm.

Green's function of the AIM  $\mathcal{G}^0(i\nu)$  via the impurity Dyson equation as

$$\mathcal{G}^0(i\nu)^{-1} = G(i\nu)^{-1} + \Sigma(i\nu). \quad (1.48)$$

Next, the AIM has to be solved. This corresponds to solving the path integral in Eq. (1.45), which is usually the numerically most expensive step in the DMFT self-consistent loop. But once the Green's function of the AIM  $G_{\text{AIM}}(i\nu)$  is obtained, its self-energy can be computed using the impurity Dyson equation once again

$$\Sigma_{\text{AIM}}(i\nu) = \mathcal{G}^0(i\nu)^{-1} - G_{\text{AIM}}(i\nu)^{-1}. \quad (1.49)$$

This self-energy  $\Sigma_{\text{AIM}}(i\nu)$  is taken as the new self-energy of the Hubbard model  $\Sigma(i\nu, \mathbf{k}) \approx \Sigma(i\nu)$  and one re-enters the self-consistent loop again. Then the algorithm is iterated until a convergence criterion, e.g.  $\sum_{i\nu} |\Sigma_{N+1}(i\nu) - \Sigma_N(i\nu)| < \epsilon$ , is fulfilled.

## 1.7 DFT+DMFT double counting correction

DFT already takes into account some correlations, as part of the Hartree term and the exchange and correlation potential  $E_{xc}$ . Thus, in order to avoid considering local correlations twice within DFT+DMFT, a double-counting correction needs to be introduced, as depicted in Eq. (1.27). However, in practice it is impossible to exactly separate local from non-local correlation parts in DFT, since the latter is based on the electron density



and not on Feynman diagrams like DMFT. Thus, the double-counting of local electronic correlations within DFT+DMFT can only be removed in an approximative way.

The double-counting correction employed in this work is based on the so-called fully localized limit (FLL) correction, which was introduced by Anisimov *et al.* [43] for the LDA+ $U$  approach. This double-counting correction is based on the assumption that the atomic limit represents a good approximation for the localized orbitals employed in DMFT. Differentiating the total energy in this fully localized limit leads to the following double-counting correction:

$$\Sigma_{DC,m} = \frac{\bar{U}}{2} \left( n_m - \frac{1}{2} \right), \quad (1.50)$$

where  $n_m$  denotes the filling of orbital  $m$  and  $\bar{U}$  is an average Coulomb interaction parameter, which in a cubic symmetry and for  $L$  orbitals can be calculated as  $\bar{U} = \frac{U+(L-1)(U-2J)+(L-1)(U-3J)}{2L-1}$  [44]. Thus, the orbitals are shifted according to their filling: half filled orbitals are left unchanged, while fully filled (empty) orbitals are shifted to negative (positive) energies. When considering only degenerate orbitals connected by symmetry (e.g. the three  $t_{2g}$  orbitals), their filling  $n_m$  is obviously the same. In this case, the double-counting correction in Eq. (1.50) results in a global shift of all orbitals and can be absorbed in the chemical potential. In the general case, however, the double-counting correction leads to mutual shifts between the included orbital manifolds (e.g. between  $e_g$  and  $t_{2g}$  orbitals).

In this work, the double-counting correction is computed only once from the DFT fillings and is not updated during the DMFT self-consistency cycle. In this case, the double-counting correction can simply be absorbed in the Wannier Hamiltonian

$$\tilde{H}_{W,mm'}^{\mathbf{k}} = H_{W,mm'}^{\mathbf{k}} - \Sigma_{DC,m} \delta_{mm'}, \quad (1.51)$$

where  $\Sigma_{DC,m}$  is now computed with the DFT fillings  $\Sigma_{DC,m} = \frac{\bar{U}}{2} (n_m^{\text{DFT}} - \frac{1}{2})$ .

The question of the most appropriate double-counting correction is still an ongoing debate. Beside the FLL double counting correction, there exists e.g. also another commonly used double-counting correction "around mean-field" (AMF) [45]. In summary, one can say that the double-counting issue is one of the drawbacks of the DFT+DMFT approach since no fundamentally exact way of solving this problem exists. Thus, it introduces a degree of arbitrariness in the *ab initio* DFT+DMFT approach. One way to overcome the double-counting problem would be the combination of DMFT with the GW method in the so-called GW+DMFT approach [46, 47]. Since GW is a perturbative diagrammatic technique, the double-counting problem can in principle be solved exactly in GW+DMFT. Furthermore, the screened Coulomb interaction  $W$  is an essential part

of the  $GW$  method and can be computed consistently within the  $GW$ +DMFT approach. However, so far no fully self-consistent  $GW$  or  $GW$ +DMFT method has been implemented<sup>11</sup> and the existing schemes again rely on DFT, suffering from similar problems as DFT+DMFT in this respect.

## 1.8 Summary: DFT+DMFT flow

The necessary steps to perform a DFT+DMFT computation—ranging from the DFT computation, the Wannier projection and cRPA, to the actual DMFT—have already been discussed in detail in the previous sections. Here, however, the single steps are summarized and shown in their context in the flow diagram Fig. 1.13. This should finally provide a compact overview of the DFT+DMFT approach.

As depicted in the flow diagram in Fig. 1.13, in the first step a DFT computation for the material under investigation is performed. For this DFT computation, we use the program package Wien2k [19]. As discussed in Sec. 1.2, from the DFT computation one obtains the Kohn-Sham energies  $\epsilon_{n\mathbf{k}}$  and wave functions  $\psi_{n\mathbf{k}}$ . Please note that the effective potential  $V_{\text{eff}}$  in Fig. 1.13 contains the ionic potential of the lattice and the electronic exchange and correlation potential.

In the second step, the correlated band-subspace needs to be identified since within DFT+DMFT one first computes the whole band-structure of the material under investigation within DFT and then one treats its correlated bands, e.g. the partially filled  $3d$  bands of transition metal elements, within DMFT. This way, (local) electronic correlations are treated properly in the bands where they are expected to play an important role, and the numerical effort of the computation remains feasible since only a few bands are treated within DMFT while one stays with the DFT result for all the other bands. Thus, we perform a Wannier projection for the correlated bands, as described in detail in Sec. 1.4. For the Wannier projection, we use the wien2wannier interface [49] and the wannier90 program [50] which constructs maximally localized Wannier functions. This way, we obtain the Wannier Hamiltonian  $H_W^{\mathbf{R}-\mathbf{R}'}$ , which is a direct input for the DFT+DMFT multi-orbital Hubbard model.

Together with the Wannier projection, the Hubbard interaction parameters  $U$ ,  $J$  and  $U'$  need to be obtained from the DFT band-structure. This is done by means of the constrained random phase approximation (cRPA), as described in detail in Sec. 1.5. With  $U$ ,  $J$ ,  $U'$  and  $H_W^{\mathbf{R}-\mathbf{R}'}$  all necessary *ab initio* input for the multi-orbital Hubbard model is provided and one can finally proceed to the actual DMFT step.

<sup>11</sup>See, however, Ref. [48] for a partially self-consistent  $GW$ +DMFT scheme.

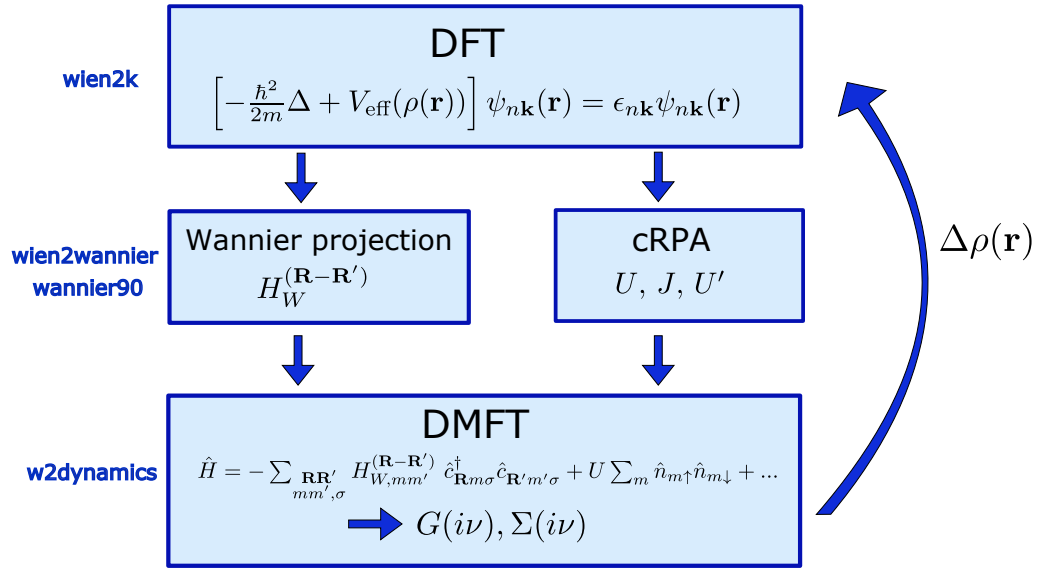


FIGURE 1.13: DFT+DMFT flow diagram

In DMFT, the multi-orbital Hubbard model is self-consistently mapped onto an auxiliary Anderson impurity model (AIM). For this inner DMFT self-consistency cycle and all details regarding DMFT please refer to Sec. 1.6. Here, it should just be mentioned that for the DMFT we use the w2dynamics program package [42, 51], which solves the AIM using continuous-time quantum Monte Carlo in the hybridisation expansion (CT-HYB) [41].

**Charge self-consistency** Once the DMFT self-energy  $\Sigma(i\nu)$  and Green's function  $G(i\nu)$  are obtained, a new charge distribution/electron density  $\rho(\mathbf{r})$  can be computed. The latter is directly connected to the Green's function via  $\rho(\mathbf{r}) = \lim_{\tau \rightarrow 0} G(\tau, \mathbf{r}, \mathbf{r}) = \lim_{\tau \rightarrow 0} \frac{1}{\beta} \sum_{i\nu} e^{-i\nu\tau} G(i\nu, \mathbf{r}, \mathbf{r})$ . Since we are interested in the difference of the charge distribution between DFT and DFT+DMFT, the quantity, which is computed, is

$$\Delta N(\mathbf{k}) = \frac{1}{\beta} \sum_{i\nu} (G(i\nu, \mathbf{k}) - G^{\text{DFT}}(i\nu, \mathbf{k})), \quad (1.52)$$

with the DMFT lattice Green's function  $G(i\nu, \mathbf{k}) = (i\nu + \mu - H_W^{\mathbf{k}} - \Sigma(i\nu))^{-1}$  and the DFT Green's function  $G^{\text{DFT}}(i\nu, \mathbf{k}) = (i\nu + \mu_{\text{DFT}} - H_W^{\mathbf{k}})^{-1}$ . Then,  $\Delta N(\mathbf{k})$  is transformed from the Wannier into the Bloch basis and into real space giving the difference in the charge distribution  $\Delta\rho(\mathbf{r})$

$$\Delta N(\mathbf{k}) \rightarrow \Delta\rho(\mathbf{r}). \quad (1.53)$$

If  $\Delta\rho(\mathbf{r})$  is not negligibly small, the Kohn-Sham energies and wave functions are updated according to the new  $\rho_{\text{new}}(\mathbf{r}) = \rho(\mathbf{r}) + \Delta\rho(\mathbf{r})$  and the DFT+DMFT cycle restarts again. For details regarding this charge-self-consistent DFT+DMFT scheme see Ref. [52]. For the DFT+DMFT studies in this work, however, no charge-self-consistency has been employed since changes in the electron density  $\Delta\rho(\mathbf{r})$  were small.

## 1.9 Spectral functions and analytical continuation

The (local) one-particle Green's function  $G(\omega)$  basically describes the process of probing an interacting many-body system with an additional particle and is thus directly connected to the spectral function of the system  $A(\omega)$  via

$$A(\omega) = -\frac{1}{\pi}\Im G(\omega). \quad (1.54)$$

The spectral function  $A(\omega)$ , which can be seen as the many-body analog of the electronic density of states, can directly be measured in photoemission spectroscopy (PES) experiments. Please note that the Green's function  $G(\omega)$  in Eq. (1.54) depends on real frequencies  $\omega$ , while the CT-QMC algorithm employed to solve the DMFT impurity problem computes the DMFT Green's function  $G(i\nu)$  on the Matsubara axis  $i\nu$ .<sup>12</sup> Thus, a transformation from imaginary to real frequencies  $i\nu \rightarrow \omega$  is needed. If  $G(i\nu)$  was known at infinitely many discrete Matsubara frequencies  $i\nu$  and with perfect precision, the problem of analytical continuation from  $i\nu$  to  $\omega$  would be well-defined and straightforward. However, since these conditions are not fulfilled for standard techniques, several methods to address the problem of analytical continuation have been developed.

One rather intuitive approach consists in directly fitting  $G(i\nu)$ , e.g. with a complex polynomial  $p(z)$  in the Padé approximation. Through the fit one then obtains an analytical expression for  $G(z)$ , from which  $G(\omega)$  can directly be obtained. However, without further improvements as e.g. in Ref. [53], this method usually works only for Green's functions  $G(i\nu)$  with very low numerical noise, and is thus not suited for QMC data. Instead, the method of choice for the analytical continuation of QMC data is usually the so-called maximum-entropy method [54].

<sup>12</sup>More precisely, the CT-QMC solver employed in this work computes the Green's function  $G(\tau)$  depending on imaginary time  $\tau$ .  $G(i\nu)$  is then obtained through a Fourier transformation.

**Maximum-entropy method** Starting from the relation between the Green's function on the Matsubara axis  $G(i\nu)$  and the spectral function  $A(\omega)$ <sup>13</sup>

$$G(i\nu) = \int d\omega \frac{-\frac{1}{\pi} \Im G(\omega)}{i\nu - \omega} = \int d\omega \frac{A(\omega)}{i\nu - \omega}, \quad (1.55)$$

one can, through a Fourier transform, derive a direct relation between  $G(\tau)$  and  $A(\omega)$

$$G(\tau) = \int d\omega \frac{A(\omega) e^{-\tau\omega}}{1 + e^{-\beta\omega}}. \quad (1.56)$$

Please note that the expression  $\frac{e^{-\tau\omega}}{1 + e^{-\beta\omega}}$  (with the inverse temperature  $\beta$ ) is often referred to as kernel function (for more details please refer to Ref. [55]). In principle, Eq. (1.56) represents a direct relation between the Green's function  $G(\tau)$  computed in QMC and the spectral function  $A(\omega)$ . However, Eq. (1.56) cannot be inverted straightforward in order to obtain the spectral function  $A(\omega)$ . Due to the exponential  $e^{-\tau\omega}$  in the kernel function, which for large  $\omega$  strongly suppresses the integrand, there usually exist many spectral functions  $A(\omega)$  which lead to essentially the same Green's function  $G(\tau)$ . Among all these possible spectral functions, the maximum-entropy method identifies the  $A(\omega)$  with the highest probability by introducing a likelihood criterion

$$p(A) \sim e^{-\frac{\chi^2}{2}} e^{\alpha S}. \quad (1.57)$$

In Eq. (1.57) the entropy term  $S$  appears, which gives the maximum-entropy method its name. It reads

$$S \sim \int d\omega A(\omega) \ln[A(\omega)]. \quad (1.58)$$

The term  $e^{-\frac{\chi^2}{2}}$  in Eq. (1.57) instead arises from the fact that one usually assumes a Gaussian distribution for the error of  $G(\tau)$  computed by QMC. For more details please refer to Ref. [55]. Here it should just be mentioned that among all possible spectral functions, which are in agreement with the  $G(\tau)$  computed in QMC, the maximum-entropy method chooses the  $A(\omega)$  with the highest entropy or, equivalently, the least features in the spectrum. This way, one avoids introducing artificial features in the spectrum, which are not sufficiently supported by the given data for  $G(\tau)$ .

**k-resolved spectral function** The **k**-resolved spectral function  $A(\omega, \mathbf{k}) = -\frac{1}{\pi} \Im G(\omega, \mathbf{k})$  can be obtained from the **k**-dependent DFT+DMFT Green's function on the real frequency axis

$$G(\omega, \mathbf{k}) = \left( \omega + \mu - H_W^{\mathbf{k}} - \Sigma(\omega) + i\delta \right)^{-1}, \quad (1.59)$$

<sup>13</sup>Eq. (1.55) is simply a special case of the general Cauchy integral formula for a complex Green's function  $G(z)$  which is analytic in the upper half plane and decays like  $1/|z|$  for large  $z$ .

with  $\mu$  being the chemical potential,  $H_W^{\mathbf{k}}$  the Wannier Hamiltonian and  $\Sigma(\omega)$  the DMFT self-energy on the real frequency axis. Since the QMC solver provides us with the self-energy on the Matsubara axis  $\Sigma(i\nu)$ , an analytical continuation is again needed to obtain  $\Sigma(\omega)$ . In order to analytically continue the self-energy  $\Sigma(i\nu)$ , I implemented an approach that makes use of the available maximum-entropy algorithm for analytically continuing  $G(\tau) \rightarrow A(\omega)$ . For this purpose, I construct a fictitious Green's function involving the DMFT Matsubara self-energy  $\Sigma(i\nu)$ , but without any Hamiltonian  $H_W^{\mathbf{k}}$ . This fictitious Green's function  $\tilde{G}(i\nu)$  reads

$$\tilde{G}(i\nu) = (i\nu - \Sigma(i\nu) - \tilde{\mu})^{-1}, \quad (1.60)$$

where  $\tilde{\mu}$  is a fictitious chemical potential, which is optimized in order to obtain a not too asymmetrical  $\tilde{G}(\tau)$ . Please note that, in contrast to the real Green's function in Eq. (1.59),  $\tilde{G}(i\nu)$  is orbital-diagonal since the QMC-solver employed in this work computes only orbital-diagonal self-energies  $\Sigma_{mm}(i\nu)$ . The fictitious  $\tilde{G}(\tau)$  corresponding to  $\tilde{G}(i\nu)$  is then obtained through a Fourier-transformation

$$\tilde{G}(\tau) = \frac{1}{\beta} \sum_{i\nu} e^{-i\nu\tau} \tilde{G}(i\nu). \quad (1.61)$$

Next,  $\tilde{G}(\tau)$  can be analytically continued by using the standard maximum-entropy method.<sup>14</sup> This way, one gets an artificial spectral function

$$\tilde{G}(\tau) \rightarrow \tilde{A}(\omega). \quad (1.62)$$

From  $\tilde{A}(\omega)$  one then obtains the fictitious Green's function on the real frequency axis  $\tilde{G}(\omega)$  through

$$\Im \tilde{G}(\omega) = -\pi \tilde{A}(\omega), \quad (1.63)$$

$$\Re \tilde{G}(\omega) = \frac{1}{\pi} \int d\omega' \frac{\Im \tilde{G}(\omega')}{\omega' - \omega}, \quad (1.64)$$

where Eq. (1.64) is a so-called Kramers-Kronig relation, a special case of Cauchy's integral formula, relating the real and the imaginary part of  $G(\omega)$ . Since  $\tilde{G}(\omega) = (\omega - \Sigma(\omega) - \tilde{\mu})^{-1}$ , the analytically continued self-energy can now directly be calculated as

$$\Sigma(\omega) = \omega - \tilde{\mu} - \tilde{G}^{-1}(\omega). \quad (1.65)$$

---

<sup>14</sup>The statistical error on  $\tilde{G}(i\nu)$  necessary for the maximum-entropy method is simply adapted from the true DMFT Green's function  $G(i\nu)$ . All orbital-diagonal components of  $\tilde{G}(\tau)$  are continued independently. Since currently no orbital-off-diagonal elements of  $\Sigma(i\nu)$  are provided, the problem of analytical continuation for orbital-off-diagonal elements does not arise. For a possible way to analytically continue orbital-off-diagonal elements see the appendix in Ref. [56]

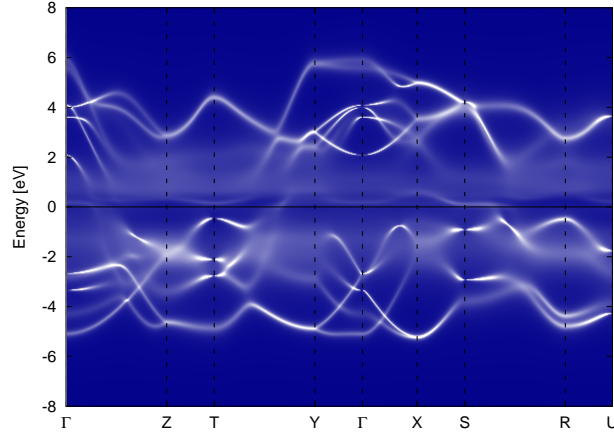


FIGURE 1.14:  $\mathbf{k}$ -resolved DFT+DMFT spectral function  $A(\omega, \mathbf{k})$  of paramagnetic  $\text{CrSb}_2$ .  $\text{CrSb}_2$  is a correlated, narrow-gap semiconductor with large thermopower at low temperatures, whose transport properties can be investigated within DFT+DMFT.

$\Sigma(\omega)$  is then used to obtain the  $\mathbf{k}$ -dependent Green's function on the real frequency axis  $G(\omega, \mathbf{k})$  according to Eq. (1.59). Finally, the  $\mathbf{k}$ -resolved spectral function is calculated as  $A(\omega, \mathbf{k}) = -\frac{1}{\pi} \Im G(\omega, \mathbf{k})$ .

I have implemented this approach for obtaining  $A(\omega, \mathbf{k})$  in the form of a python-script, which makes use of the maximum-entropy program by A. Sandvik [54] and is interfaced with w2dynamics. This methodology has subsequently been successfully applied to  $\text{CrSb}_2$  (see Fig. 1.14),  $\text{FeAl}$  (see Fig. 2.3) and to  $\text{SrRuO}_3/\text{SrTiO}_3$  heterostructures in Ref. [57].





## Chapter 2

# Screened moments and absence of ferromagnetism in FeAl

*In this chapter, I present the results of a DFT+DMFT study for the intermetallic FeAl, especially its magnetic properties. The latter are intriguing since DFT predicts the material to be ferromagnetic, while it is paramagnetic in experiment. I show that this discrepancy can be overcome by a better treatment of electronic correlations within DFT+DMFT. There, the absence of ferromagnetism in FeAl is explained by dynamical spin fluctuations that screen short-lived local magnetic moments of  $1.6 \mu_B$ . Please note that this chapter has been adapted from the article A. Galler et al., Phys. Rev. B 92, 205132 (2015). For the latter, which is partially building upon my Master thesis, I have done the calculations, analyzed the results and written the first version of the paper.*

### 2.1 Motivation

Intermetallic alloys of iron and aluminum have a high hardness with a much lower specific weight than steel. Because of this, their low costs, and resistance against corrosion and oxidation, FeAl alloys are often used as lightweight structural materials. Most puzzling are the magnetic properties. Here, experiments such as high-field Mössbauer investigations [58] indicate no magnetism for stoichiometric FeAl which forms a *B2* CsCl-type of lattice (two interpenetrating Fe and Al simple cubic lattices). Especially the fact that FeAl does not show ferromagnetism in experiment, while electronic structure calculations within spin-polarized density functional theory (DFT) predict a ferromagnetic ground state, has drawn attention to the material: independently of the band-structure code, DFT orbital basis set and exchange correlation potential, a ferromagnetic ground state with a magnetic moment at the Fe site of about  $0.7 \mu_B$  is found [58–62]. Even

though the energy difference between the ferromagnetic and the nonmagnetic state is rather small, the ferromagnetic state is stable over a wide volume range. In fact, only a reduction of the lattice constant by more than 10% would suppress ferromagnetism [63]. This high stability of the ferromagnetic phase in FeAl suggests that the deviation from experiment is not just a numerical inaccuracy, but requires a deeper understanding.

Different approaches have been used hitherto to explain the deviation between spin-polarized DFT and experiment. One explanation is based on the fact that the processes used to prepare FeAl often "freeze in" chemical disorder. That is, "real" FeAl is usually not fully ordered due to various lattice defects, such as vacancies and antisites, which in turn could have a significant effect on the magnetic properties of the material. Against this background, there exist several studies concerning the effects of disorder on the magnetic properties of FeAl [60, 62, 64, 65]. For example, in Ref. [64] the disorder is included via the coherent potential approximation (CPA) [66] in the Korringa, Kohn and Rostoker (KKR) framework [67, 68], with the paramagnetic phase described by the disordered local moment approximation (DLM) [69]. In agreement with previous DFT calculations, it has been found that ideal FeAl is ferromagnetic. However, even with a small degree of disorder the paramagnetic state, without net magnetization but nonzero local moments, becomes the stable configuration. Thus, disorder destroys the long-range ferromagnetic order in DFT.

However, no ferromagnetism has ever been observed for stoichiometric "real" FeAl, even for samples with very low defect concentration. Therefore, it still remains the question if perfectly ordered FeAl would really be ferromagnetic as predicted by DFT. Indeed, Mössbauer experiments [58] find magnetic moments only for Fe antistructure atoms (which means Fe atoms sitting on an Al lattice site) and their eight Fe neighbors.

Another possible explanation has been given in Ref. [63] using the DFT+ $U$  approach [45]. Usually, one would expect DFT+ $U$  to yield larger magnetic moments and a stronger tendency towards ferromagnetism than DFT. For  $U$  values ranging from 4 to 5 eV a nonmagnetic state however coexists with the ferromagnetic one in DFT+ $U$ . The ferromagnetic state even disappears for a rather large  $U = 5$  eV, which offers another explanation of the non-magnetic nature of FeAl. This rather unusual DFT+ $U$  result can be explained by the changes in the density of states (DOS): increasing  $U$  reduces the DOS at the Fermi level so that according to the Stoner criterion there is no ferromagnetism [63] even though the effective exchange is increased by  $U$  [70]. Hence, in a narrow range of  $U$ , there is no ferromagnetism in DFT+ $U$  [63].

In Ref. [70] it has been argued that this DFT+ $U$  result has to be taken with a grain of salt and it has been proposed for the first time that dynamical spin fluctuations suppress ferromagnetism in FeAl. This has been supported by a dynamical mean-field theory

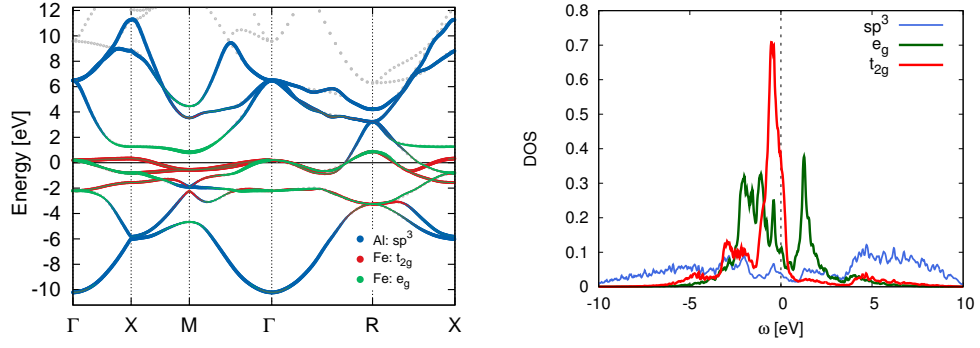


FIGURE 2.1: Electronic band-structure (left) and density of states (right) of FeAl within DFT. The color coding indicates the band character obtained from the Wannier projection.

(DMFT [5, 6]) calculation [70]. For  $U = 2$  eV, FeAl is found [70] to be paramagnetic in DFT+DMFT [38, 71–73]. However, Ref. [70] only shows a single DFT+DMFT result, the spectral function. The proposed spin fluctuations, the magnetic properties and susceptibility have not been calculated.

Considering these limited results as well as the improvements of DFT+DMFT in recent years, a more thorough analysis is in order. Beyond the first DFT+DMFT spectrum of Ref. [70], we study the local and bulk magnetic susceptibility, the magnetic moment and the  $k$ -resolved spectrum. We also explicitly calculate the local interactions *ab initio* by constrained random phase approximation (cRPA) and beyond Ref. [70] we include the calculated Hund’s exchange in DMFT with its full  $SU(2)$  symmetry, since it plays a pivotal role for the magnetic properties. Our results show that while there is a local moment of even  $1.6 \mu_B$  on short time scales, it is screened (suppressed) on longer time scales. This suppression of the local moment occurs on the fs time scale ( $\text{eV}^{-1}$ ) and explains why there is eventually no long-range ferromagnetic order.

## 2.2 Electronic structure within DFT

As a first step, we employ the Vienna *ab initio* Simulation Package (VASP) [16] with GGA-PBE functional [10] for calculating the band-structure and density of states of FeAl. The left panel of Fig. 2.1 shows the band-structure of FeAl around the Fermi level. The bands closest to the Fermi level have mainly Fe 3d character and are split into  $t_{2g}$  and  $e_g$  due to the cubic crystal field. For these bands we will later include electronic correlations by DMFT. However, since the Fe 3d bands strongly hybridize with the Al 3s and 3p states, we also include these Al bands (as non-interacting) in our low energy Hamiltonian. The corresponding Hamiltonian is obtained by a projection

onto nine maximally localized Wannier orbitals [50], which reproduce the DFT band-structure well.

The right panel of Fig. 2.1 shows the orbital resolved density of states. It can be seen that the central peak is mainly of  $t_{2g}$  character. As the Fe  $t_{2g}$  orbitals form only weak bonds with the nearest-neighbor Al atoms, they have a rather small energy dispersion. The Fe  $e_g$  states instead point towards the neighboring Fe atoms and hybridize more strongly. Hence they have a larger bandwidth and split into a bonding- and an antibonding-like part.

## 2.3 DMFT self-energy and spectral function

After obtaining the low energy Hamiltonian in the basis of Wannier functions, we perform DMFT calculations including the five Fe  $d$  orbitals and the 4 Al  $sp^3$  orbitals within a so-called  $dp$  model [74]. We supplement the DFT-based Wannier Hamiltonian in DMFT by a local  $d-d$  Kanamori interaction, but disregard  $d-p$  and  $p-p$  interactions beyond what is already contained in DFT. Note that the hopping terms of the Hamiltonian still contain the full information about the hybridization with the Al  $sp^3$  states and charge transfer between  $d$  and  $sp^3$  orbitals is allowed.

We calculate the screened many-body Coulomb interactions  $U$ ,  $U'$  and  $J$  by the constrained random phase approximation (cRPA) [32, 33], where we exclude only the Fe  $d$  states from the screening. This is appropriate as interactions are also applied only to these  $d$  states [75]. For our DMFT calculation, we use the average values for the intra-orbital Coulomb interaction  $U = 3.36$  eV, the inter-orbital Coulomb interaction  $U' = 2.36$  eV and the Hund's coupling  $J = 0.71$  eV. This yields a local,  $SU(2)$ -symmetric Kanamori interaction [27, 76]:

$$\begin{aligned} \hat{H}_{\text{loc}} = & U \sum_m \hat{n}_{m\uparrow} \hat{n}_{m\downarrow} + \sum_{m \neq m', \sigma \sigma'} (U' - \delta_{\sigma \sigma'} J) \hat{n}_{m\sigma} \hat{n}_{m'\sigma'} \\ & + J \sum_{m \neq m'} \left( \hat{c}_{m\uparrow}^\dagger \hat{c}_{m'\downarrow}^\dagger \hat{c}_{m\downarrow} \hat{c}_{m'\uparrow} + \hat{c}_{m\uparrow}^\dagger \hat{c}_{m\downarrow}^\dagger \hat{c}_{m'\downarrow} \hat{c}_{m'\uparrow} + h.c. \right). \end{aligned} \quad (2.1)$$

Here,  $\hat{c}_{m\sigma}^\dagger$  ( $\hat{c}_{m\sigma}$ ) creates (annihilates) an electron with spin  $\sigma$  in the Fe  $3d$  orbital  $m$ ;  $\hat{n}_{m\sigma} = \hat{c}_{m\sigma}^\dagger \hat{c}_{m\sigma}$ . We employ the double counting correction of the fully localized limit [43], and validate that a difference of 2.5 eV in the double counting does not change our findings (not shown).

For the solution of the DMFT impurity problem we use a continuous-time quantum Monte Carlo (CT-QMC) algorithm in its hybridization expansion (CT-HYB) in the

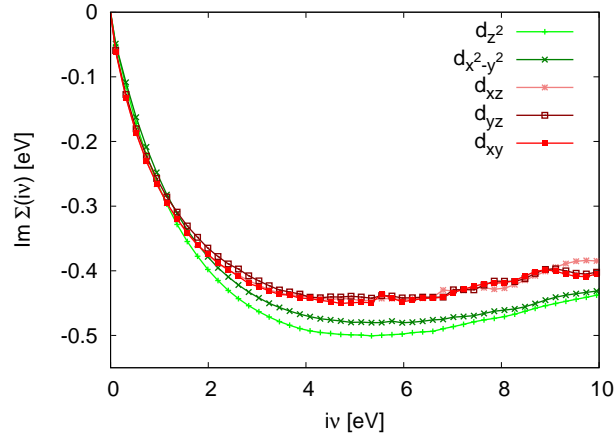


FIGURE 2.2: DMFT self-energies for the Fe  $d$  orbitals (at inverse temperature  $\beta = 30 \text{ eV}^{-1}$  corresponding to 390 K). The extracted quasiparticle weight is  $Z = 0.75$ .

version of Ref. [42], for a review see Ref. [41]. Especially with regard to the magnetic properties that we will compute, it is important to employ the rotationally invariant form of the interaction term  $H_{\text{loc}}$  above, including a pair-hopping and a spin-flip term, and not only density-density contributions. As for the CT-HYB, we note that it is essential to truncate the outer states for the evaluation of the local fermionic trace only at high energies, especially at high temperatures.

Fig. 2.2 shows the imaginary part of the DMFT self-energy  $\Sigma(i\nu)$  on the Matsubara axis for all five Fe  $d$  orbitals. In order to avoid all uncertainties related to an analytical continuation, we calculate the quasiparticle weight  $Z$  directly from the self-energy on the Matsubara axis  $Z = 1/(1 - \Im(\partial\Sigma(i\nu)/\partial(i\nu))|_{i\nu \rightarrow 0})$ . This yields a value of  $Z = 0.75$ , essentially the same for all  $3d$  orbitals. This  $Z$  value would indicate a rather weakly correlated material.

The corresponding spectral function  $A(\omega, \mathbf{k}) = -1/\pi \Im(G(\omega, \mathbf{k}))$  is shown in Fig. 2.3 on the real frequency axis, for which an analytic continuation using a stochastic version of the maximum entropy method has been used [54]. In comparison to the DFT DOS, both occupied and empty states are slightly shifted towards the Fermi energy due to the Fermi-liquid renormalization. There is no evidence of pronounced upper and lower Hubbard bands and one can only observe a weak increase of the spectral weight at high frequencies. In agreement with Ref. [70], we find that the spectral function at the Fermi level is essentially the same in DFT+DMFT as in DFT. We did not perform charge-self-consistent calculations since the difference in the occupation of the  $d$ -orbitals between the DFT-derived Hamiltonian and DMFT is very small. In DFT, we have 4.8 electrons in the  $t_{2g}$  and 2.5 electrons in the  $e_g$  states out of 11 electrons per unit cell, in DMFT the  $t_{2g}$  orbitals are occupied with 4.8 and the  $e_g$  orbitals with 2.6 electrons. Also the changes in the one-particle spectrum are rather small. Note, only if DMFT alters

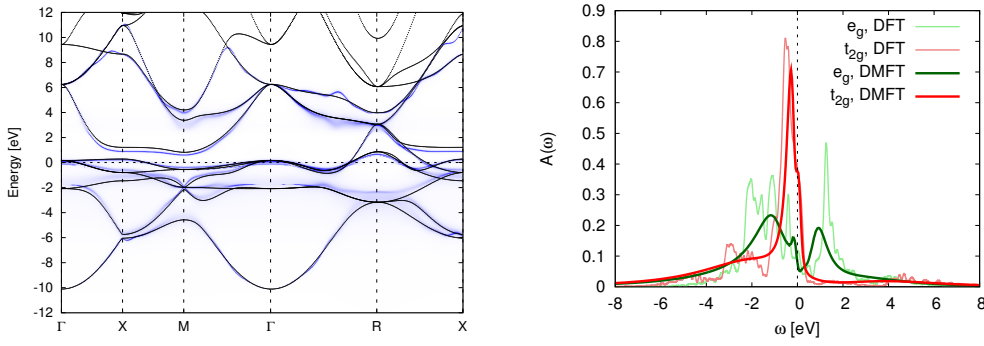


FIGURE 2.3: DMFT  $k$ -resolved (left) and  $k$ -integrated (right) spectral function at  $\beta = 30 \text{ eV}^{-1}$ , compared to DFT.

the spatial charge distribution  $\rho(\mathbf{r})$  considerably, charge self-consistency would have an effect. Thus, we expect changes by charge-self-consistency to be small.

Fig. 2.3 presents the corresponding  $k$ -resolved spectrum which shows that also the DFT+DMFT bands essentially follow the DFT band-structure. The most noteworthy effects are again a slight shift towards the Fermi level, i.e., a quasiparticle renormalization and a broadening of the bands, especially of the  $d$  bands located around the Fermi level. Hence, regarding only single-particle quantities, FeAl seems to exhibit only weak correlation effects. However, this picture changes when considering also two-particle quantities, namely the magnetic susceptibility.

## 2.4 DMFT magnetic properties

In order to study the magnetic properties of FeAl within DFT+DMFT, we compute the local magnetic susceptibility, represented by the two-particle spin-spin correlation function

$$\chi_{\text{loc}}(\tau) = \sum_{mn} \chi_{\text{loc}}^{mn}(\tau) = g^2 \sum_{mn} \left\langle \hat{S}_z^m(\tau) \hat{S}_z^n(0) \right\rangle \quad (2.2)$$

with  $m$  and  $n$  being the orbital indices of the five Fe  $d$  orbitals,  $\tau$  the imaginary time, and  $g \approx 2$  the gyromagnetic factor for the electronic spin.  $\hat{S}_z^m(\tau) = 1/2(\hat{n}_{m\uparrow}(\tau) - \hat{n}_{m\downarrow}(\tau))$  is the  $z$ -component of the spin operator of orbital  $m$ , expressed in terms of the corresponding density operators  $\hat{n}_{m\sigma} = \hat{c}_{m\sigma}^\dagger \hat{c}_{m\sigma}$ .

Technically speaking,  $\chi_{\text{loc}}(\tau)$  is obtained by first measuring the generalized magnetic susceptibility  $\chi_{\text{loc}}(i\omega, i\nu, i\nu')$  of the converged DMFT impurity model by means of CT-HYB quantum Monte Carlo sampling. Thereby,  $\chi_{\text{loc}}(i\omega, i\nu, i\nu')$  automatically contains all vertex corrections to the bare (DMFT) bubble spin susceptibility. The sum

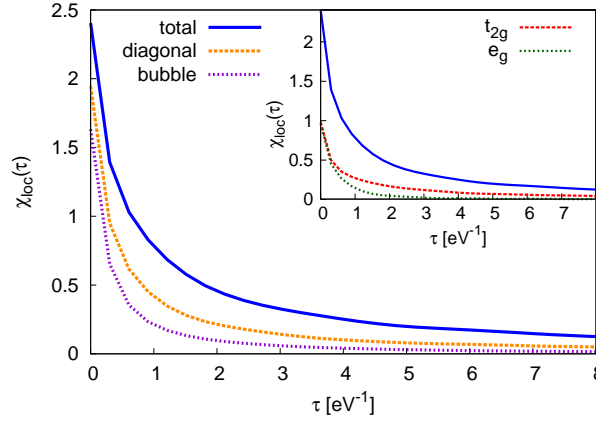


FIGURE 2.4: Local magnetic susceptibility  $\chi_{\text{loc}}$  as a function of (imaginary) time  $\tau$  for  $\beta = 30 \text{ eV}^{-1}$ . Besides the total susceptibility, also its diagonal and bare-bubble contribution are shown, as well as (in the inset) its  $e_g$  and  $t_{2g}$  contribution.

over the fermionic Matsubara frequencies  $\nu$  and  $\nu'$  and a Fourier transform,  $\chi_{\text{loc}}(\tau) = 1/\beta \sum_{i\omega} e^{-i\omega\tau} \chi(i\omega)$ , finally lead to  $\chi_{\text{loc}}(\tau)$ . Here, for the large frequency asymptotics, the bare bubble contribution, Eq. (2.3), which is known on a larger frequency grid and an additional fitting function of the form  $1/\nu^2$  have been used. The results for  $\chi_{\text{loc}}(\tau)$  are shown in Fig. 2.4 for  $\beta = 30 \text{ eV}^{-1}$  (for lower temperatures the numerically feasible frequency box becomes too small).

The solid, blue curve in Fig. 2.4 corresponds to the total magnetic susceptibility  $\chi_{\text{loc}}(\tau)$  of Eq. (2.2). The dashed, orange curve instead represents the orbital-diagonal contribution  $\sum_m \chi_{\text{loc}}^{mm}(\tau)$ . The dotted, purple curve is the bare-bubble contribution  $\chi_{0,\text{loc}}(\tau)$ , which neglects vertex corrections and is obtained by directly convoluting the DMFT Green functions  $G_m(i\nu)$ :

$$\chi_{0,\text{loc}}(i\omega) = -\frac{1}{\beta} \sum_{i\nu, m\sigma} G_{m\sigma}(i\nu) G_{m\sigma}(i\nu + i\omega) \quad (2.3)$$

The significant difference between the bare-bubble contribution and the susceptibility including vertex corrections in Fig. 2.4 reveals that electronic correlations actually play a major role in FeAl, more than it could be expected from the weak quasiparticle renormalization. Fig. 2.4 also shows that the enhancement of  $\chi_{\text{loc}}(\tau)$  stems approximately in equal parts from an enhancement of the intra-orbital contribution (diagonal part) and additional inter-orbital (off-diagonal) contributions, which are not present in the bare-bubble susceptibility.

The local susceptibilities in Fig. 2.4 show a rather fast and strong decay in  $\tau$ . Here, the value of  $\chi_{\text{loc}}(\tau)$  at  $\tau = 0$  can be interpreted in terms of the instantaneous, local magnetic moment. The observed decay in  $\tau$  reflects a dynamical screening of this local magnetic

moment due to quantum fluctuations. Thus, we can conclude that dynamical quantum fluctuations significantly reduce the local magnetic moment in FeAl.

Fitting  $\chi_{\text{loc}}(\tau)$  to an exponential between  $\tau = 0 \text{ eV}^{-1}$  and  $\tau = 5 \text{ eV}^{-1}$  yields a time scale for the screening of  $\tau_s = 1.03 \text{ eV}^{-1} = 4.02 \text{ fs}$ . The inverse of  $\tau_s$  is the energy scale associated with the screening which is essentially the bare bandwidth if we have a noninteracting system, the width of the central peak if we consider the interacting bubble, and the Kondo temperature for the interacting system with vertex corrections. This Kondo temperature is smaller than the width of the central peak [77]. Hence the decay with vertex corrections should be slower. Indeed, in Fig. 2.4 the total  $\chi_{\text{loc}}(\tau)$  decays slower than the bubble contribution. For a related analysis, how to interpret the susceptibility as a function of imaginary time and how the local, fluctuating magnetic moment reflects as a pronounced low-energy peak in the local neutron spectra, see Refs. [78–80].

In the inset of Fig. 2.4, we separate the  $e_g$  and  $t_{2g}$  contributions of the susceptibility. These two contributions are rather independent as one clearly sees from the longer time scale on which the  $t_{2g}$  susceptibility decays. This different decay rate can be explained by the considerably more narrow  $t_{2g}$  bandwidth and hence stronger correlations of the  $t_{2g}$  orbitals. If Hund’s exchange was the major player, on the other hand, one would expect a stronger coupling of  $e_g$  and  $t_{2g}$  susceptibility, and a decay on a similar time scale.

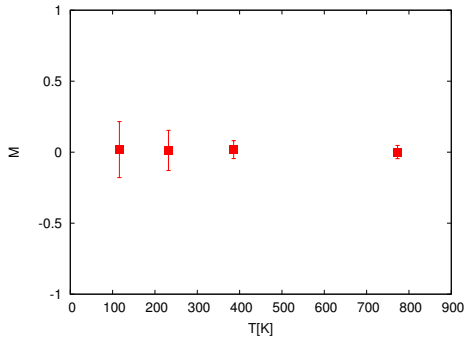


FIGURE 2.5: DFT+DMFT magnetization for different temperatures. The ferromagnetic moment is zero within the error bars.

This all suggests that the Hund’s rule exchange  $J$ , which mainly drives the inter-orbital contribution, is not exceedingly important in FeAl. This is in contrast to other Fe-based compounds such as the iron-based superconductor LaFeAsO [75, 78], which have been classified as Hund’s metals [76, 81].

From the local magnetic properties, we now turn to the bulk magnetic susceptibility and the long-range ordered ferromagnetic moment. Fig. 2.5 shows the ordered magnetic moment, which has been obtained by breaking the spin

symmetry in the first DMFT iteration so that the system can either stabilize a para- or ferromagnetic solution. As Fig. 2.5 clearly shows, the ordered ferromagnetic moment is zero down to a temperature of 100 K. Thus, in the investigated temperature range, FeAl is paramagnetic in DFT+DMFT, in agreement with experiment but in contrast to DFT.



This result is also supported by the calculation of the bulk ferromagnetic susceptibility in DFT+DMFT. To this end, we have applied a small magnetic field of  $H = 0.005 \text{ eV}$ , checked (for some temperatures) that this is still in the linear  $M$  vs.  $H$  regime (which further confirms the paramagnetic phase) and calculated  $\chi(\mathbf{q} = 0) = M/H$  at this  $H$ . This way all vertex corrections are included; and this quantity allows to determine whether there is a second order phase transition towards a ferromagnetic phase or not. Prospectively competing phases with a different wave vector  $\mathbf{q}$  are however not accessible this way.

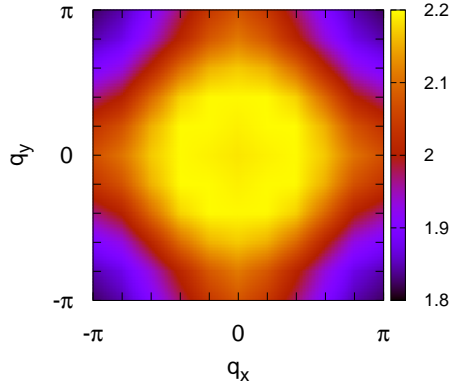


FIGURE 2.6: Susceptibility  $\chi_0(i\omega = 0, \mathbf{q})$  vs.  $q_x$  and  $q_y$  (at  $q_z = 0$ ) calculated from the DMFT  $d$ -electron Green functions at  $\beta = 100 \text{ eV}^{-1}$ . The maximum at  $\mathbf{q} = 0$  indicates that without vertex corrections ferromagnetism is the leading instability.

The full  $\mathbf{q}$ -dependent susceptibility  $\chi(i\omega, \mathbf{q})$  could in principle be obtained by solving the Bethe-Salpeter equation. Unfortunately, this is computationally too demanding for five orbitals at low temperatures. For the same reason the local susceptibility  $\chi_{\text{loc}}(\tau)$  could only be calculated reliably down to  $\beta = 30 \text{ eV}^{-1}$ . But to gain at least some insight whether ferromagnetism or magnetic phases with other  $\mathbf{q}$ -vectors prevail, we study the bare bubble susceptibility  $\chi_0(i\omega = 0, \mathbf{q}) = -\frac{1}{\beta} \frac{1}{N_k} \sum_{i\nu, \mathbf{k}, m, n, \sigma} G_{mn\sigma}(i\nu, \mathbf{k}) G_{nm\sigma}(i\nu, \mathbf{k} + \mathbf{q})$ , which does not include vertex corrections. The result shown in Fig. 2.6 indicates that  $\mathbf{q} = 0$  is the leading instability.<sup>1</sup> Thus, in the following we will focus on  $\chi(\mathbf{q} = 0)$ .

The temperature dependence of the susceptibility  $\chi(\mathbf{q} = 0) = M/H$  including vertex corrections is shown in Fig. 2.7. Upon decreasing temperature, we first notice an increase of the susceptibility. However, below 400K, the susceptibility decreases again. This clear trend of a *reduction* of the susceptibility by decreasing  $T$  makes the onset of a ferromagnetic order at lower temperatures extremely unlikely. We note that a marked low- $T$  reduction of  $\chi(\mathbf{q} = 0)$  has been also reported experimentally [84] and theoretically [85] in the iron-pnictide compound LaFeAsO. There, this behavior of  $\chi(\mathbf{q} = 0)$  coexists with an opposite (increasing) trend of the local magnetic susceptibility  $\chi_{\text{loc}}$  [85]. Hence, the unusual low- $T$  reduction of  $\chi(\mathbf{q} = 0)$  has been attributed to specific features of the one-particle spectral function of LaFeAsO, displaying significant temperature variations near the Fermi level. By performing the same analysis for FeAl we find, however, that the low- $T$  behavior of  $\chi_{\text{loc}}$  (inset of Fig. 2.7) and  $\chi(\mathbf{q} = 0)$  (main panel) is qualitatively

<sup>1</sup>While the Stoner criterion  $I\chi(q = 0) > 1$  would predict ferromagnetism for  $I = U$  or  $I = J$ , it is known that this criterion largely overestimates the tendency towards ferromagnetism [82, 83].

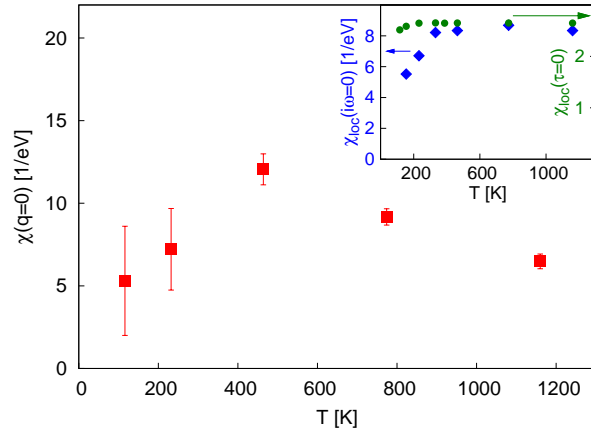


FIGURE 2.7: Ferromagnetic susceptibility  $\chi(q = 0)$  as a function of temperature. The inset shows the temperature dependence of the corresponding local quantities: the local magnetic susceptibility ( $\chi_{\text{loc}}(i\omega = 0)$ , diamonds) and the instantaneous one ( $\chi_{\text{loc}}(\tau = 0)$ , circles), from which the local magnetic moment can be estimated ( $\propto \sqrt{\chi_{\text{loc}}}$ ).

very similar: both show a visible reduction for  $T < 400\text{K}$ . In the very same temperature interval, a slight reduction of the instantaneous local moment ( $\chi_{\text{loc}}(\tau = 0)$ , inset) is also found, which is a typical behavior in the Fermi liquid regime, as described by the DMFT.

Hence, in FeAl, the role played by emerging low-energy structures of the spectral function appears to be less important than in LaFeAsO. Rather, the trend of  $\chi(\mathbf{q} = 0)$  in FeAl may simply reflect the corresponding low- $T$  reduction of the local magnetic moment ( $\propto \sqrt{\chi_{\text{loc}}}$ ), in particular of the screened one. The latter can be ascribed to the enhanced metallic coherence of the low-temperature region, which is a general effect of local correlations in the Fermi-liquid regime.

## Chapter 3

# Beyond DMFT: the dynamical vertex approximation ( $D\Gamma A$ )

*This chapter provides an introduction to the dynamical vertex approximation ( $D\Gamma A$ ), a diagrammatic extension of DMFT. After a general overview of extensions of DMFT, I will discuss the basic ideas of  $D\Gamma A$ , which has become a successful approach to non-local electronic correlations over the last years. Starting from the two-particle Green's function and the diagrammatic content of  $D\Gamma A$ , I will introduce both, its full parquet version and ladder approximation together with the most important equations. However, before presenting all the detailed equations of the newly developed *Abinitio* $D\Gamma A$  in the next chapter, this chapter should only give a schematic overview of  $D\Gamma A$  without going too much into details.*

### 3.1 Extensions of DMFT

The dynamical mean-field theory (DMFT) is without any doubt a very powerful method to study strongly correlated electron systems. By combining density functional theory and dynamical mean-field theory in the DFT+DMFT approach, it is possible to investigate the physical properties of materials with strong electronic correlations. In fact, within DFT+DMFT physical observables like the spectral function, magnetic susceptibility, optical conductivity or thermoelectric response of materials with up to or even more than five orbitals in the correlated subspace can be computed. These physical quantities can then be compared directly to experimental findings and often the agreement is already quantitative. Nevertheless, as DMFT remains a mean-field theory in

the spatial coordinates, it does not capture any non-local electronic correlations.<sup>1</sup> In DMFT the effect of electrons at different lattice sites on the electrons on one specific lattice site is considered only through a mean-field. However, in contrast to classical mean-field theories, DMFT avoids taking a time average, so it can account for all local, temporal electronic correlations.

The DMFT approach of considering neighboring lattice sites through a mean-field is exact in infinite dimensions and usually turns out to be a good approximation in 3d. However, in lower dimensions, e.g. in materials with a 2d or 1d structure or a preferred direction, a mean-field in space can be a very poor approximation. Superconducting cuprates with their layered crystal structure or oxide heterostructures are highly discussed examples for such low-dimensional structures. There, spatial electronic correlations, which cannot be taken into account by DMFT, are expected to play an important role. The same applies to materials close to a second-order phase transition, e.g. the transition from para- to ferromagnetism. In the latter case, the correlation length of the fluctuations corresponding to the emerging ferromagnetic order becomes very large and diverges at the transition. Thus, close to the phase transition non-local correlations are expected to play an important role and the purely local DMFT treatment is no longer satisfying. Furthermore, non-local correlations also arise in materials where the Coulomb interaction is not well screened. There, a non-local Coulomb interaction beyond the Hubbard model needs to be taken into account, leading to additional non-local electronic correlations among the electrons.

The inclusion of spatial electronic correlations seems to be necessary in order to investigate many intriguing physical phenomena in condensed matter physics. On the other hand, DMFT already provides an accurate treatment of all local electronic correlations within the Hubbard model and one does not want to sacrifice these merits. Thus, the goal is to build on DMFT and to develop extensions that can add non-local corrections on top of the local DMFT correlations.

**Cluster extensions** One possible and rather intuitive way to include spatial electronic correlations are cluster extensions of DMFT. There, the single DMFT impurity site is replaced by a cluster of sites. This way, all spatial electronic correlations within the cluster size are taken into account. There exist two different classes of cluster extensions, depending on whether they are formulated in real or in momentum space. In the so-called cellular DMFT (CDMFT) [86] the cluster is defined in real space while the dynamical cluster approximation (DCA) [87, 88] works with clusters in momentum

---

<sup>1</sup>When referring to *non-local* correlations or a *non-local* Coulomb interaction, the term *non-local* simply means *not local* and thus *with a spatial dependence*. However, please note that non-local electronic correlations can include both, classical correlations and quantum entanglement.

space. Compared to CDMFT, the DCA has the advantage of not breaking the lattice translational symmetry of the system. CDMFT, on the other hand, is better suited to treat natural units in anisotropic systems, such as the vanadium dimer in the  $M_1$  phase of  $\text{VO}_2$  [89].

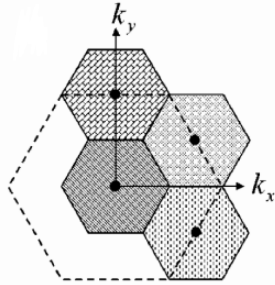


FIGURE 3.1: Here, for a DCA study of the half-filled Hubbard model on a triangular lattice, the first Brillouin zone has been divided into four coarse-grained cells yielding a four-site cluster. (Figure taken from Ref. [90].)

In order to get closer to the real lattice problem it is the best to have a cluster made of as many sites as possible. But of course there are numerical limitations regarding the number of cluster sites. For a single-band Hubbard model clusters with up to 100 sites are feasible [91], while for multi-band materials' computations only a few sites are possible. For  $\text{SrVO}_3$ —the material that we will investigate with the dynamical vertex approximation—only a cluster made of two sites has been considered in a DCA study so far [92]. This means that actual cluster DMFT computations can account only for short-range spatial electronic correlations. While

short-range fluctuations within the cluster size are treated very accurately, cluster DMFT studies need to completely neglect spatial long-range electronic correlations or have access to them only when reasonable cluster sizes are reached and extrapolations with respect to the cluster size can be performed. Certainly, close to a second-order phase transition, electronic correlations on all length scales should be considered.

**Diagrammatic extensions** Long-range electronic correlations can be taken into account by diagrammatic extensions of DMFT. The latter do not enlarge the DMFT impurity problem by adding additional impurity sites, but instead are adding additional non-local Feynman diagrams to the local DMFT self-energy. Since the diagrammatic content of DMFT is well known—the DMFT self-energy contains all local irreducible one-particle Feynman diagrams—non-local Feynman diagrams can systematically be added. There exist different methods of diagrammatic extensions, among them the  $GW$ +DMFT approach [46, 47], the dynamical vertex approximation (D $\Gamma$ A) [7], the dual fermion (DF) [93], the one-particle irreducible approach (1PI) [94], the Trilex [95] and the Quadrilex [96] method. While the  $GW$ +DMFT approach directly supplements the local DMFT self-energy with the non-local screened exchange diagram of  $GW$ , all other methods are based on the local two-particle vertex function, which can be obtained from the DMFT impurity model. The differences between the diagrammatic extensions based on the two-particle vertex function lay in the details: the considered vertex function (e.g. D $\Gamma$ A employs the fully irreducible, while the 1PI approach the one-particle irreducible

vertex), the involved one-particle Green's function (e.g. D $\Gamma$ A uses the DMFT lattice Green's function, while the DF approach the completely non-local Green's function) and the kind of the constructed non-local diagrams.

A detailed comparison of the different diagrammatic extensions and their merits can be found in Ref. [97]. In the following, I will instead focus on the dynamical vertex approximation (D $\Gamma$ A). The latter has already been successfully used for studying model systems such as the one-band Hubbard model. Among these D $\Gamma$ A studies, there are the investigation of the Mott metal-insulator transition in the 2d Hubbard model [9, 98, 99], a study of the critical exponents in the 3d Hubbard model and the breakdown of the paramagnetic Fermi-liquid regime at low temperatures due to spin fluctuations [8, 100], and the investigation of a possible separation of the D $\Gamma$ A self-energy into spatial and dynamical components [101, 102]. Here, in this thesis, the D $\Gamma$ A approach will be generalized to multi-orbital systems and a non-local Coulomb interaction, so that realistic materials' computations become feasible. This newly developed AbinitioD $\Gamma$ A method and its implementation will be presented in detail in Chap. 4. Before, however, I will give a brief and schematic introduction to the D $\Gamma$ A formalism following the discussion in Ref. [103].

## 3.2 An introduction to D $\Gamma$ A

The dynamical vertex approximation (D $\Gamma$ A) [7] is a diagrammatic extension of DMFT whose aim is to add non-local corrections to the local DMFT self-energy. The additional non-local Feynman diagrams are obtained from the two-particle Green's function and its corresponding vertex function. Thus, I will first introduce the two-particle Green's function and other important ingredients for the D $\Gamma$ A. Then, the basic ideas of the D $\Gamma$ A in its parquet and ladder version will be presented.

### 3.2.1 The two-particle Green's function

In analogy to the one-particle Green's function—which is the propagator of a single particle and the main building block of DMFT—the two-particle Green's function describes the propagation and interaction of two particles (or a particle and a hole). Similar to the one-particle Green's function which has already been introduced in Eq. (1.36),

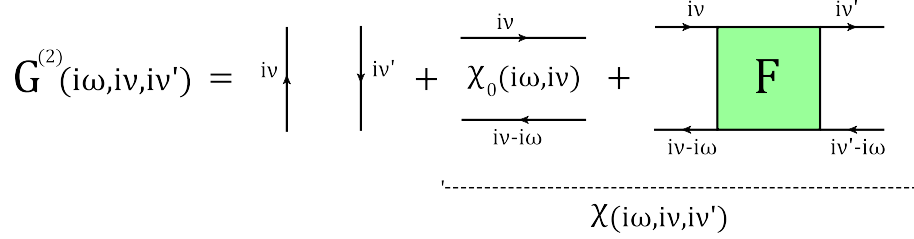


FIGURE 3.2: Diagrammatic representation of the two-particle Green's function:  $G^{(2)}(i\omega, i\nu, i\nu')$  consists of two disconnected, non-interacting terms and one connected, interacting term including the full vertex function  $F$ . As indicated, the connected term and the disconnected bubble term  $\chi_0(i\omega, i\nu)$  form the generalized susceptibility  $\chi(i\omega, i\nu, i\nu')$ .

the two-particle Green's function is defined as<sup>2</sup>

$$G_{\sigma_1\sigma_2\sigma_3\sigma_4}^{(2)}(\tau_1, \tau_2, \tau_3, \tau_4) = \langle \mathcal{T} [\hat{c}_{\sigma_1}(\tau_1) \hat{c}_{\sigma_2}^\dagger(\tau_2) \hat{c}_{\sigma_3}(\tau_3) \hat{c}_{\sigma_4}^\dagger(\tau_4)] \rangle. \quad (3.1)$$

Thus, it describes two particles being inserted in the system at (imaginary) times  $\tau_2$  and  $\tau_4$ , propagating in the system and then being extracted again at  $\tau_1$  and  $\tau_3$  respectively ( $\sigma_i$  are spin indices). Taking into account time translational invariance, we can set  $\tau_4 = 0$  yielding a two-particle Green's function depending on three times only. Then, a Fourier transformation of Eq. (3.1) gives a two-particle Green's function  $G_{\sigma_1\sigma_2\sigma_3\sigma_4}^{(2)}(i\omega, i\nu, i\nu')$  depending on three frequencies; two fermionic Matsubara frequencies,  $i\nu = \frac{i(2n+1)\pi}{\beta}$  and  $i\nu'$ , and one bosonic Matsubara frequency  $i\omega = \frac{i2n\pi}{\beta}$ . Furthermore, the fact that, in absence of spin-orbit interaction, the spin needs to be conserved, restricts the spin degrees of freedom and allows for the following combinations with two different spins only:

$$G_{\sigma\sigma'}^{(2)}(i\omega, i\nu, i\nu') = G_{\sigma\sigma'\sigma'\sigma}^{(2)}(i\omega, i\nu, i\nu'), \quad (3.2)$$

$$G_{\frac{\sigma}{\sigma'}}^{(2)}(i\omega, i\nu, i\nu') = G_{\sigma\sigma'\sigma'\sigma}^{(2)}(i\omega, i\nu, i\nu'). \quad (3.3)$$

In terms of Feynman diagrams the two-particle Green's function can be represented as shown in Fig. 3.2. It consists of two disconnected contributions—representing the independent propagation of the particles—and a connected part that stems from the interaction among the particles. The disconnected parts are simply pairs of one-particle Green's functions and can be written as  $G(i\nu)G(i\nu')$  and  $G(i\nu)G(i\nu - i\omega)$  respectively. The latter is the so-called bubble term  $\chi_0(i\omega, i\nu) = G(i\nu)G(i\nu - i\omega)$ . The connected part instead takes into account all possible interactions among the two particles, the so-called vertex corrections. In fact, the quantity  $F$  is the full vertex function and it

<sup>2</sup>Here, for simplicity, we restrict ourselves to the local, single-orbital two-particle Green's function (without any  $\mathbf{k}$ -dependence or orbital indices). For a detailed multi-orbital definition within AbinitioDFA please refer to Eq. (4.2).

consists of all connected two-particle diagrams. Thus, from a physical point of view,  $F$  can be seen as the scattering amplitude between two particles.

Usually one does not directly work with the two-particle Green's function, but rather with the generalized susceptibility  $\chi(i\omega, i\nu, i\nu')$ .<sup>3</sup> In order to obtain the latter, the disconnected term with  $G(i\nu)G(i\nu')$ —the first one in Fig. 3.2—needs to be subtracted from the two-particle Green's function. Indeed, the generalized susceptibility is formed by the last two contributions in Fig. 3.2, namely the disconnected bubble term  $\chi_0(i\omega, i\nu) = G(i\nu)G(i\nu - i\omega)$  and the connected part including the full vertex  $F$ . This diagrammatic relation can be easily translated into an equation<sup>4</sup>

$$\chi = \chi_0 + \chi_0 F \chi_0, \quad (3.4)$$

with  $\chi_0$  being the non-interacting (bubble) and  $\chi$  the full susceptibility. Thus, if the susceptibilities  $\chi$  and  $\chi_0$  are known, the full vertex function  $F$  can be obtained from Eq. (3.4).

### 3.2.2 The basic idea of DΓA

Since DΓA is a diagrammatic extension of DMFT, it builds on DMFT which accounts already very accurately for all local electronic correlations. In fact, the DMFT self-energy  $\Sigma_{\text{loc}}$  contains all local, irreducible, skeleton one-particle Feynman diagrams.

In DΓA the assumption of locality is raised one level higher: the fully irreducible two-particle vertex function  $\Lambda$  is assumed to be purely local.<sup>5</sup> Hence,  $\Lambda_{\text{loc}}$  contains all local, fully irreducible two-particle diagrams. The two diagrams explicitly shown in the diagrammatic series for  $\Lambda_{\text{loc}}$  in Fig. 3.4 are two of these fully irreducible two-particle diagrams and represent two possible ways of interaction among the two particles. Note that the first diagram—the lowest-order contribution to  $\Lambda_{\text{loc}}$ —is simply the local Coulomb interaction  $U$ . Thus, in analogy to the local Coulomb interaction  $U$  in DMFT, the fully irreducible vertex function  $\Lambda_{\text{loc}}$  represents the interaction part in DΓA.

The local, fully irreducible vertex function  $\Lambda_{\text{loc}}$  is one main building block of DΓA. The second necessary ingredient is the lattice DMFT Green's function  $G_{\text{DMFT}}(i\nu, \mathbf{k}) = 1/[i\nu + \mu - \epsilon_{\mathbf{k}} - \Sigma_{\text{DMFT}}(i\nu)]$ . With these two building blocks—the "interaction"  $\Lambda_{\text{loc}}$

<sup>3</sup>Physical susceptibilities, which depend just on one frequency argument, can be obtained from this generalized susceptibility via a summation over the two fermionic frequencies,  $\chi(i\omega) = 1/\beta^2 \sum_{i\nu, i\nu'} \chi(i\omega, i\nu, i\nu')$ .

<sup>4</sup>For clarity, in this introductory chapter all equations are written in a schematic way, in particular all spin and frequency arguments are omitted. For detailed equations see Chap. 4 about AbinitioDΓA.

<sup>5</sup>Full irreducibility at the two-particle level means that a two-particle diagram cannot be split into two parts by cutting two internal fermionic lines.



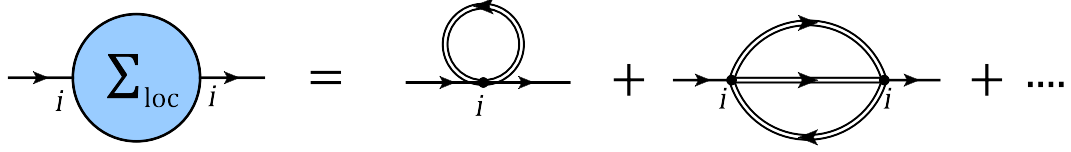


FIGURE 3.3: In DMFT, the self-energy  $\Sigma_{\text{loc}}$  is a purely local quantity containing all local, irreducible one-particle Feynman diagrams. Dots represent the local Hubbard interaction  $U$  and  $i$  is a lattice site index. Please also note that the double lines are dressed Green's functions, so they already contain DMFT self-energy inclusions.

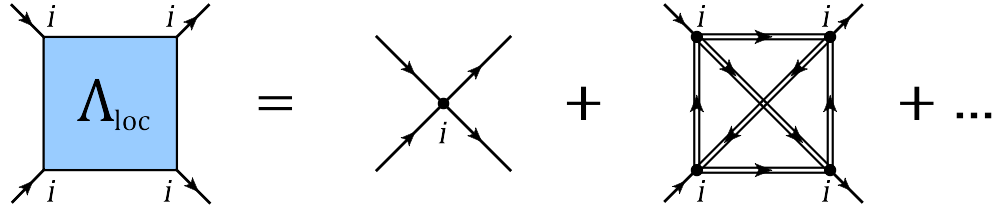


FIGURE 3.4: In DΓA the fully irreducible two-particle vertex  $\Lambda_{\text{loc}}$  is purely local. It consists of the bare interaction  $U$  and all fully irreducible two-particle diagrams of which the first (envelope) diagram is shown.

and the propagator  $G_{\text{DMFT}}$ —a huge variety of diagrams can be constructed. These diagrams form the non-local reducible vertex function  $F$ , which in turn leads—through the equation of motion—to the non-local ( $\mathbf{k}$ -dependent) DΓA self-energy  $\Sigma_{\text{DΓA}}(i\nu, \mathbf{k})$ .<sup>6</sup>

According to the type of diagrams included in  $F$ , two different DΓA schemes are distinguished. The so-called ladder-DΓA considers only ladder diagrams in a specific channel, which—roughly speaking—means that vertex functions (irreducible in the specific channel) are lined up in a row or column and connected by DMFT propagators. Considering only ladder diagrams in a specific channel can be well justified if it is clear in which channel the leading instabilities are expected to be. The full parquet version of the DΓA instead takes into account also more complicated “parquet-like” diagrams, which basically means ladder diagrams in multiple channels that are intertwined self-consistently with each other. Needless to say, the parquet version of the DΓA is more complete than the ladder scheme—it contains ladder diagrams in all channels and additional non-ladder-type diagrams—but is also much more demanding to realize. Thus, for realistic multi-orbital computations, we restrict ourselves to the ladder version of the DΓA. Nevertheless, for completeness and clarity, I will first introduce the full parquet version of the DΓA before switching to the ladder approximation which is eventually employed in the *ab initio* DΓA scheme.

<sup>6</sup>By considering higher-order  $n$ -particle vertex functions, DΓA would for  $n \rightarrow \infty$  eventually yield the exact solution of the lattice problem. But the computation of three- and more-particle vertex functions is numerically extremely demanding. Thus, at the moment DΓA does not take into account any higher-order vertex function than  $n=2$ .

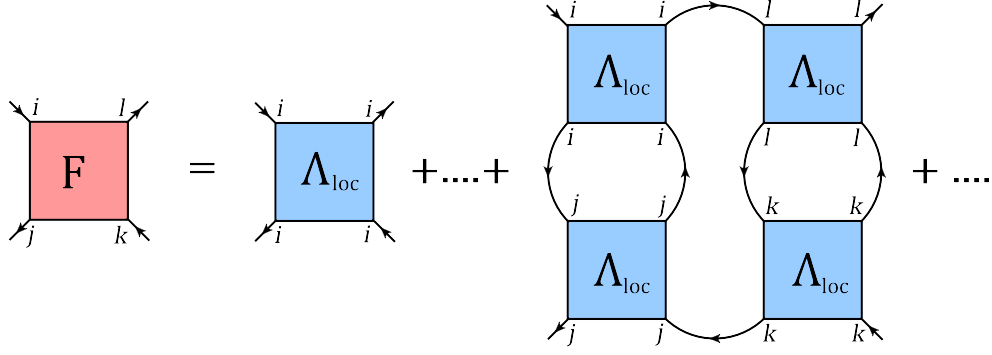


FIGURE 3.5: Two diagrams contributing to the full vertex  $F_{ijkl}$  in the parquet version of DΓA. The non-local  $F_{ijkl}$  is obtained by connecting local, fully irreducible vertices  $\Lambda_{iiii}$  (obtained from an auxiliary impurity model) with non-local DMFT Green's functions  $G_{ij}$ . (The indices  $i, j, k, l$  denote lattice sites.)

### 3.2.3 Full parquet version

The diagrams contributing to the full non-local vertex function  $F_{ijkl}$  are constructed by connecting the local, fully irreducible vertex function  $\Lambda_{iiii}$  with non-local DMFT Green's functions, i.e.  $G(i\nu, \mathbf{k}) = 1/[i\nu + \mu - \epsilon_{\mathbf{k}} - \Sigma_{\text{DMFT}}(i\nu)]$ . Thus, the non-locality of the full vertex function  $F_{ijkl}$ —represented by the four different site indices—can in principle be traced back to the non-local DMFT Green's functions used in the construction of the parquet- or ladder diagrams. The fully irreducible vertex  $\Lambda_{iiii}$  instead is purely local and can be obtained from an auxiliary Anderson impurity model. Fig. 3.5 shows two exemplary diagrams that contribute to  $F_{ijkl}$  if the full parquet version of DΓA is employed.

**Parquet decomposition** The diagrams contributing to the reducible vertex function  $F_{ijkl}$  can systematically be divided into four categories according to their reducibility. In analogy to the definition of one-particle-irreducibility, full irreducibility at the two-particle level means that a diagram cannot be split into two parts by cutting two internal fermionic lines. All fully irreducible two-particle diagrams are contained in the fully irreducible vertex function  $\Lambda$ , which we have already identified as one of the main building blocks of DΓA. All other diagrams present in  $F$  are reducible diagrams, but they can be further divided into three categories since at the two-particle level there exist three possibilities (called channels) to cut a diagram into two pieces. Thus, a diagram can be reducible in the particle-particle ( $pp$ ) channel, the particle-hole ( $ph$ ) channel or the transverse particle-hole ( $\overline{ph}$ ) channel. A diagram is always either fully irreducible or reducible in one channel. Thus,  $F$  can be written in the form of the so-called parquet equation

$$F = \Lambda + \phi_{pp} + \phi_{ph} + \phi_{\overline{ph}}, \quad (3.5)$$

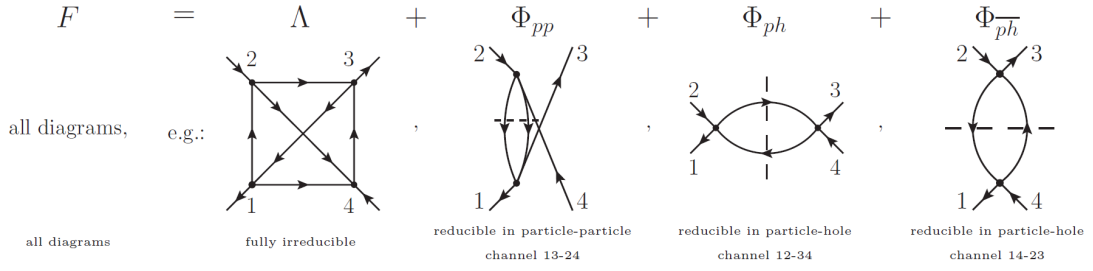


FIGURE 3.6: Diagrammatic illustration of the parquet equation. For each contribution (fully irreducible, reducible in  $pp$ ,  $ph$  or  $\overline{ph}$  channel) a low-order diagram is shown. (Figure reproduced from Ref. [104].)

where  $\Lambda$  represents the fully irreducible vertex function and  $\phi_r$  the reducible vertex functions in a certain channel  $r = (pp, ph, \overline{ph})$ . Fig. 3.6 shows lowest-order examples for each type of diagrams.

**Bethe-Salpeter equation** Another possibility is to divide the full vertex function  $F$  in reducible and irreducible diagrams in one channel  $r$

$$F = \Gamma_r + \phi_r, \quad (3.6)$$

where  $\Gamma_r$  is the irreducible vertex in a certain channel  $r = (pp, ph, \overline{ph})$  and  $\phi_r$  the corresponding reducible vertex. Thus,  $\Gamma_r$  contains all diagrams which are irreducible in channel  $r$  while  $\phi_r$  contains all reducible ones in that channel. Note that irreducible diagrams in a certain channel can still be reducible in another channel. For instance,  $\Gamma_{ph}$  contains all fully irreducible diagrams, but also all diagrams reducible in the  $pp$  or the  $\overline{ph}$  channel:  $\Gamma_{ph} = \Lambda + \phi_{pp} + \phi_{\overline{ph}}$ . Since the reducible diagrams in a certain channel can be expressed in terms of the corresponding irreducible ones and the full vertex via  $\phi_r = \Gamma_r \chi_0 F$ , we can write  $F$  in the form of a Dyson-like equation

$$F = \Gamma_r + \phi_r = \Gamma_r + \Gamma_r \chi_0 F, \quad (3.7)$$

where the bubble term is, in general, the product of two non-local Green's functions  $\chi_0 = GG$ . According to Eq. (3.7),  $F$  can be expressed as the sum of all irreducible diagrams in a specific channel  $\Gamma_r$  and the reducible diagrams in this channel  $\phi_r$ . And the latter can be obtained by connecting the irreducible diagrams  $\Gamma_r$  with the full vertex  $F$  via a pair of one-particle Green's functions  $\chi_0 = GG$ . Eq. (3.7) is the so-called Bethe-Salpeter equation which is—besides the parquet equation—another crucial ingredient for the D $\Gamma$ A.

Before turning to another relation needed in D $\Gamma$ A—the equation of motion—let me just add a remark on the channel decomposition of  $F$ . We have already seen that all

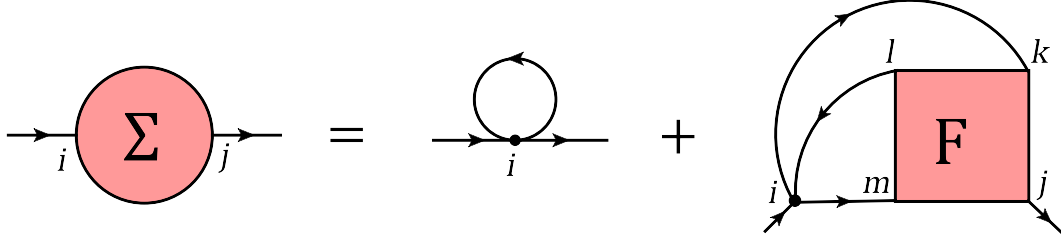


FIGURE 3.7: Diagrammatic representation of the equation of motion. The non-local DΓA self-energy  $\Sigma_{ij}$  is obtained from the full vertex  $F_{ijkl}$  and the DMFT Green's functions  $G_{ij}$ .

reducible two-particle diagrams can be divided into diagrams reducible in the  $ph$ ,  $\overline{ph}$  or  $pp$  channel. If we take into account also the spin-dependence, the definition of channels needs to be extended. By considering SU(2) symmetry, there are three independent spin combinations  $\uparrow\uparrow$ ,  $\uparrow\downarrow$ ,  $\overline{\uparrow\downarrow}$ . Together with the  $ph$ ,  $\overline{ph}$  and  $pp$  channel this would lead to nine possible combinations. However, by considering further symmetries (e.g. the so-called crossing symmetry), it turns out that there are only four independent channels, which are usually defined in the following way:

$$\Gamma_d^{\nu\nu'\omega} = \Gamma_{ph,\uparrow\uparrow}^{\nu\nu'\omega} + \Gamma_{ph,\uparrow\downarrow}^{\nu\nu'\omega}, \quad (3.8)$$

$$\Gamma_m^{\nu\nu'\omega} = \Gamma_{ph,\uparrow\uparrow}^{\nu\nu'\omega} - \Gamma_{ph,\uparrow\downarrow}^{\nu\nu'\omega}, \quad (3.9)$$

$$\Gamma_s^{\nu\nu'\omega} = \Gamma_{pp,\uparrow\downarrow}^{\nu\nu'\omega} - \Gamma_{pp,\uparrow\uparrow}^{\nu\nu'\omega}, \quad (3.10)$$

$$\Gamma_t^{\nu\nu'\omega} = \Gamma_{pp,\uparrow\downarrow}^{\nu\nu'\omega} + \Gamma_{pp,\uparrow\uparrow}^{\nu\nu'\omega}. \quad (3.11)$$

Defined in this way, the Bethe-Salpeter equations in the so-called (d)ensity, (m)agnetic, (s)inglet and (t)riplet channel decouple.

**Equation of motion** Finally, an additional relation—the Schwinger-Dyson equation of motion—is needed to perform DΓA. The Schwinger-Dyson equation of motion connects the full vertex function  $F$  with the self-energy  $\Sigma$  and reads

$$\Sigma = \frac{Un}{2} + (U\chi_0 F)G. \quad (3.12)$$

Thus, in DΓA the equation of motion (3.12) is used to obtain the non-local self-energy  $\Sigma$  from the full, non-local vertex function  $F$  through a convolution with non-local DMFT Green's functions  $G$ . In fact,  $F$  is contracted by  $\chi_0 = GG$  and a third Green's function  $G$  (for a diagrammatic illustration of the equation of motion see Fig. 3.7).

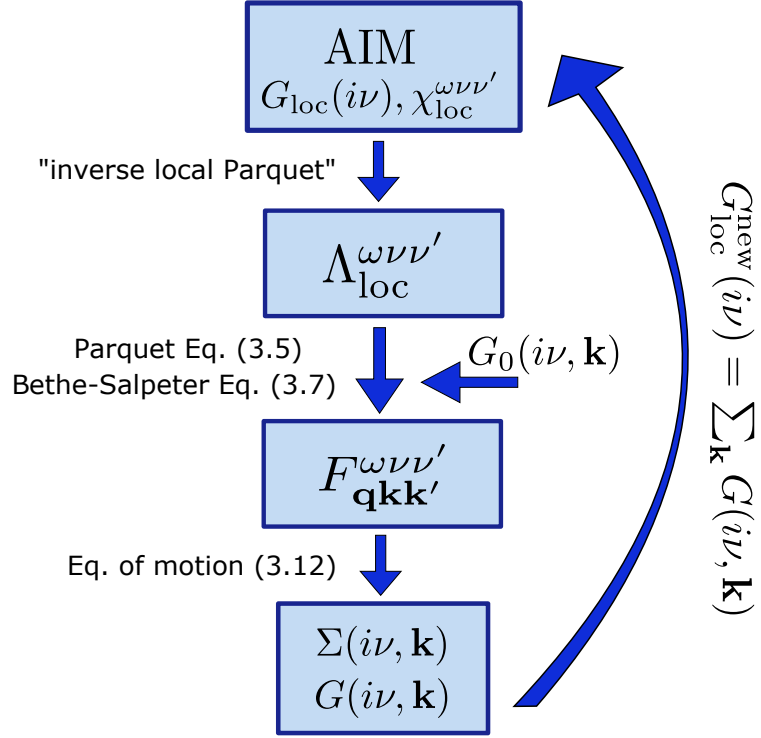


FIGURE 3.8: Flow diagram of the DGA algorithm in its full parquet version.

**Parquet-DGA flow** To conclude this section, a schematic flow diagram of the DGA algorithm is depicted in Fig. 3.8. It shows how the relations presented so far are employed.

In a first step, an auxiliary Anderson impurity model (AIM) is solved by using an appropriate impurity solver, e.g. exact diagonalization (ED) or continuous-time quantum Monte Carlo (CT-HYB). A converged DMFT solution—and thus the AIM which the lattice problem is mapped onto in DMFT—is usually a reasonable starting point for DGA. However, compared to DMFT, in DGA not only the one-particle impurity Green’s function  $G_{\text{loc}}(i\nu)$ , but also the two-particle Green’s function or the corresponding generalized susceptibility  $\chi_{\text{loc}}^{\omega\nu\nu'}$  need to be computed. Clearly, the computation of  $\chi_{\text{loc}}^{\omega\nu\nu'}$  is numerically much more demanding than the computation of  $G_{\text{loc}}(i\nu)$ , especially for multi-orbital systems. In fact, this is one of the bottlenecks of the DGA algorithm.

In a second step, the fully irreducible vertex of the impurity model  $\Lambda_{\text{loc}}^{\omega\nu\nu'}$  needs to be extracted from  $\chi_{\text{loc}}^{\omega\nu\nu'}$ . This procedure is referred to as “inverse local parquet” in Fig. 3.8 and is done by first computing the irreducible vertices  $\Gamma_r$  and the corresponding reducible ones  $\phi_r$  in all channels using the local Bethe-Salpeter equation (3.7). Then, the fully irreducible vertex  $\Lambda_{\text{loc}}^{\omega\nu\nu'}$  can be obtained through the local version of the parquet equation (3.5).

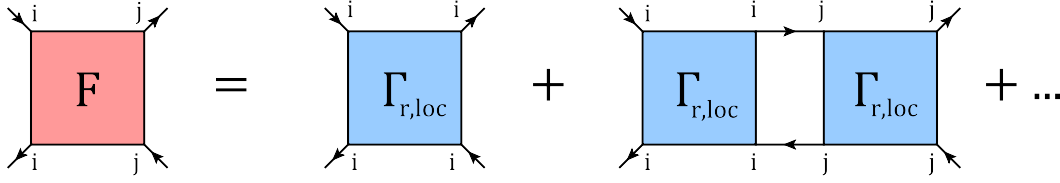


FIGURE 3.9: In ladder-DΓA, the full non-local vertex  $F$  consists of ladder diagrams in a specific channel  $r$ . The ladder diagrams are formed by local, irreducible vertex functions  $\Gamma_{r,\text{loc}}$  connected with non-local DMFT Green's functions  $G_{ij}$ .

In the next step, the full non-local vertex of the lattice  $F_{\mathbf{q}\mathbf{k}\mathbf{k}'}^{\omega\nu\nu'}$  needs to be computed from  $\Lambda_{\text{loc}}^{\omega\nu\nu'}$  and the non-interacting lattice Green's function  $G_0(i\nu, \mathbf{k}) = 1/[i\nu + \mu - \epsilon_{\mathbf{k}}]$ . Thereby,  $\Lambda_{\text{loc}}^{\omega\nu\nu'}$  is assumed to be the fully irreducible vertex of the lattice.  $F_{\mathbf{q}\mathbf{k}\mathbf{k}'}^{\omega\nu\nu'}$  can be obtained by employing the parquet (3.5) and the Bethe-Salpeter equations (3.7) in all channels. From  $F_{\mathbf{q}\mathbf{k}\mathbf{k}'}^{\omega\nu\nu'}$  the  $\mathbf{k}$ -dependent self-energy  $\Sigma(i\nu, \mathbf{k})$  can then directly be calculated via the equation of motion (3.12). The way of obtaining  $F_{\mathbf{q}\mathbf{k}\mathbf{k}'}^{\omega\nu\nu'}$  and  $\Sigma(i\nu, \mathbf{k})$  from  $\Lambda_{\text{loc}}^{\omega\nu\nu'}$  and  $G_0(i\nu, \mathbf{k})$  is an iterative procedure itself.<sup>7</sup> Beside the computation of  $\chi_{\text{loc}}^{\omega\nu\nu'}$ , it is the second numerical bottleneck of the DΓA algorithm.

Once  $\Sigma(i\nu, \mathbf{k})$  and the corresponding  $G(i\nu, \mathbf{k})$  are obtained, we can, in principle, recompute the local Green's function  $G_{\text{loc}}^{\text{new}}(i\nu) = \sum_{\mathbf{k}} G(i\nu, \mathbf{k})$ , which in turn defines a new AIM. Thus, the self-consistent loop starts again from the beginning and is iterated till convergence of  $\Sigma(i\nu, \mathbf{k})$  is reached.

This full, self-consistent DΓA scheme is numerically extremely demanding. Especially for realistic multi-orbital systems it is currently not feasible. Thus, usually one employs a simplified version of DΓA, the so-called ladder-DΓA approximation which is discussed in the next section.

### 3.2.4 Ladder approximation

In the ladder approximation of DΓA, only a certain type of non-local diagrams is considered. In fact, in ladder-DΓA the full non-local vertex  $F$  contains only ladder diagrams in a specific channel. These ladder diagrams are obtained by aligning local irreducible vertex functions  $\Gamma_{r,\text{loc}}$  in the channel  $r$  under consideration and connecting them with non-local one-particle DMFT Green's functions  $G_{ij}$ . Thereby, the local irreducible vertex function  $\Gamma_{r,\text{loc}}$  is obtained from the DMFT impurity model and the ladder diagrams

<sup>7</sup>In a self-consistent loop  $G$ ,  $F$  and  $\Gamma_r$  are first initialized with reasonable values (e.g. the non-interacting lattice Green's function  $G_0$  and the local Hubbard  $U$ ). Then, the reducible vertices  $\phi_r$  can be obtained by means of  $\phi_r = \Gamma_r \chi_0 F$ . Through the parquet equation (3.5) these  $\phi_r$  define a new  $F^{\text{new}}$ . With this  $F^{\text{new}}$ , new  $\Gamma_r^{\text{new}}$  are defined through  $\Gamma_r^{\text{new}} = F^{\text{new}} - \phi_r$  and a new lattice self-energy  $\Sigma^{\text{new}}$  can be computed via the equation of motion (3.12). Through the Dyson equation a new  $G^{\text{new}}$  can be obtained. Then the self-consistent-loop starts again and is iterated till convergence of  $\Sigma/G$  is reached [105].

are constructed through the Bethe-Salpeter equation (3.7) which has already been introduced and is discussed in more detail here.

The Bethe-Salpeter equation actually describes a summation of ladder diagrams. By translating Fig. 3.9 into an equation, one ends up with

$$\begin{aligned}
 F &= \Gamma_{r,\text{loc}} + \Gamma_{r,\text{loc}}\chi_0\Gamma_{r,\text{loc}} + \Gamma_{r,\text{loc}}\chi_0\Gamma_{r,\text{loc}}\chi_0\Gamma_{r,\text{loc}} + \dots \\
 &= \Gamma_{r,\text{loc}} + \Gamma_{r,\text{loc}}\chi_0\left(\Gamma_{r,\text{loc}} + \Gamma_{r,\text{loc}}\chi_0\Gamma_{r,\text{loc}} + \dots\right) \\
 &= \Gamma_{r,\text{loc}} + \Gamma_{r,\text{loc}}\chi_0 F,
 \end{aligned} \tag{3.13}$$

which is exactly the Bethe-Salpeter equation that has already been introduced in Eq. (3.7). The only difference is that here  $\Gamma_r$  has been replaced by the local  $\Gamma_{r,\text{loc}}$ , that can be obtained from the DMFT impurity model. Please also note that in the ladder approximation the full vertex  $F$  in Fig. 3.9 includes only scattering processes of a particle and a hole from one common lattice site  $i$  to another common lattice  $j$ , since  $\Gamma_{r,\text{loc}}$  is a purely local quantity. In Fourier space, this means that  $F$  depends only on the transferred momentum  $\mathbf{q}$  and not on the momenta of the incoming particle and hole  $\mathbf{k}$  and  $\mathbf{k}'$ .

In the present ladder-D $\Gamma$ A scheme, we solve the Bethe-Salpeter equation in the  $r = ph$  channel. However, in addition also non-local ladders in the  $\overline{ph}$  channel are taken into account. The  $\overline{ph}$ -ladders can be obtained from the  $ph$ -ladders through symmetry considerations. However, all diagrams in the  $pp$  channel are assumed to be purely local. This means that, compared to the full parquet version of D $\Gamma$ A, not only the fully irreducible vertex  $\Lambda$ , but also  $\phi_{pp}$  is assumed to be local

$$F_{\text{lad}} = \Lambda_{\text{loc}} + \phi_{pp,\text{loc}} + \phi_{ph} + \phi_{\overline{ph}}. \tag{3.14}$$

Assuming all diagrams in the  $pp$  channel to be purely local, can be justified if the leading instabilities in the system under investigation are not connected to this channel. The non-local ordering instabilities in the  $ph$  and  $\overline{ph}$  channel are associated with (anti)ferromagnetism, magnons or charge density waves, while the non-local  $pp$  ladder can describe attractive pairing (e.g. superconductivity) and localization effects. If the latter are not expected to be dominant in the system under consideration, non-local ladder diagrams in the  $pp$  can be neglected. However, since one often does not know the leading instabilities in a system *a priori*, it would be better to consider non-local diagrams in all channels—as it is done in the full parquet version of D $\Gamma$ A. But, since from a numerical point of view the full parquet scheme is not (yet) feasible for multi-orbital systems, the ladder approximation makes it possible to pioneer insight into non-local correlation phenomena in realistic materials. By keeping in mind which kind of physics is captured and making sure that at least the contribution of the lowest-order non-local

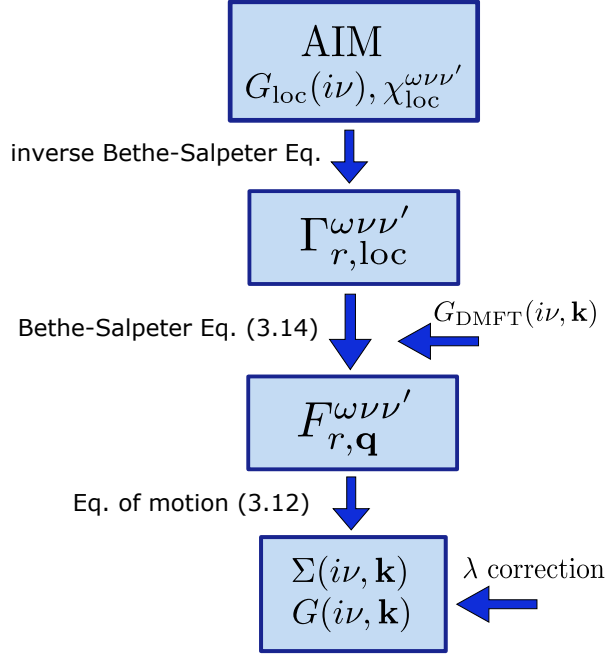


FIGURE 3.10: Flow diagram of the ladder-DΓA algorithm.

diagrams, that have been disregarded, is small, the ladder approximation can be a good approximation to perform DΓA.

**Ladder-DΓA flow** The ladder-DΓA computations performed so far—including the ones in this thesis—are "one-shot" computations starting from a converged DMFT solution. The corresponding flow diagram of the algorithm is depicted in Fig. 3.10 and briefly described in the following.

In a first step, the DMFT impurity model needs to be solved. This yields the local DMFT Green's function  $G_{\text{loc}}(i\nu)$  and the generalized susceptibility  $\chi_{\text{loc}}^{\omega\nu\nu'}$ . In contrast to the full parquet scheme introduced earlier, it is necessary to start the ladder-DΓA flow from a converged DMFT solution. In fact, since there is no self-consistent cycle, the ladder-DΓA scheme starts from a DMFT solution and adds non-local electronic correlations on top of it.

In the second step, the local irreducible vertex  $\Gamma_{r,\text{loc}}^{\omega\nu\nu'}$  in the  $ph$ -channel is extracted from  $\chi_{\text{loc}}^{\omega\nu\nu'}$  by inverting the local Bethe-Salpeter equation.

Next, the Bethe-Salpeter equation is used to construct the full non-local vertex function  $F_{\mathbf{q}}^{\omega\nu\nu'}$ . This is done exactly in the way it is depicted in Fig. 3.9 and formulated in Eq. (3.13). Thus, non-local ladder diagrams are constructed from the local  $\Gamma_{r,\text{loc}}^{\omega\nu\nu'}$  and the  $\mathbf{k}$ -dependent DMFT Green's function  $G_{\text{DMFT}}(i\nu, \mathbf{k})$ .



From the full vertex  $F_{\mathbf{q}}^{\omega\nu\nu'}$ , the ladder-D $\Gamma$ A self-energy  $\Sigma(i\nu, \mathbf{k})$  is then obtained through the Schwinger-Dyson equation of motion (3.12).

**$\lambda$ -correction** The fact that there is no self-consistency in ladder-D $\Gamma$ A is reflected in an enhanced asymptotic behavior of the lattice self-energy. Thus, in order to restore the  $1/i\nu$  asymptotic behavior of the ladder-D $\Gamma$ A self-energy, a correction needs to be introduced. This correction of the self-energy can be done in the form of a so-called Moriyasque  $\lambda$ -correction. For details about this correction please refer to Ref. [103]. Here it should just be mentioned that the  $\lambda$ -correction is done at the level of the physical susceptibilities  $\chi_{r,\mathbf{q}}^{\omega} = 1/\beta^2 \sum_{\nu\nu'} \chi_{r,\mathbf{q}}^{\omega\nu\nu'}$ , since it is always desirable to apply such an effective correction to a real physical observable. Correcting the physical susceptibilities in a way that mimics self-consistency at the two particle level ( $\chi_{r,\text{loc}}^{\omega} = \sum_{\mathbf{q}} \chi_{r,\mathbf{q}}^{\lambda,\omega}$ ), turns out to cure the asymptotic behavior of the ladder-D $\Gamma$ A self-energies. Please note, however, that in this thesis no  $\lambda$ -correction has been employed since for the AbinitioD $\Gamma$ A study of SrVO<sub>3</sub> in Chap. 5 the corrections turned out to be very small.



## Chapter 4

# *Ab initio* dynamical vertex approximation

*In this chapter, the *ab initio* dynamical vertex approximation (AbinitioD $\Gamma$ A) is presented in detail. AbinitioD $\Gamma$ A is the extension of D $\Gamma$ A to *ab initio* materials' calculations and represents a unifying framework: it includes both, GW and DMFT-type of diagrams, but also important non-local correlations beyond, e.g. non-local spin fluctuations. The development and implementation of this new methodology has been one main part of this thesis. Thus, in the first part of this chapter, all multi-orbital equations are derived and the corresponding diagrams are shown. Then, in the second part, I discuss some implementational details regarding the newly developed AbinitioD $\Gamma$ A program. Finally, in the end of this chapter, I show the results of some test cases and benchmarks.*

### 4.1 Derivation of the equations

The *ab initio* dynamical vertex approximation (AbinitioD $\Gamma$ A) is the extension and application of the D $\Gamma$ A formalism to realistic multi-orbital systems. It allows us to perform *ab initio* materials calculations beyond DFT+DMFT [38] or GW+DMFT [46] by including electronic correlations on all length scales. In principle, a fully self-consistent AbinitioD $\Gamma$ A scheme would be desirable. However, from a numerical point of view, the D $\Gamma$ A in its full parquet version is currently not feasible for multi-orbital systems. Thus, the AbinitioD $\Gamma$ A in its current implementation adopts the ladder-D $\Gamma$ A approximation presented in the previous Chap. 3.2.4. Besides the multi-orbital structure, the AbinitioD $\Gamma$ A approach includes a non-local Coulomb interaction  $V^{\mathbf{q}}$  beyond the local Coulomb interaction  $U$  of the Hubbard model. This non-local  $V^{\mathbf{q}}$  accounts for the spatial dependence of the Coulomb interaction and can be computed *ab initio* by using

constrained random phase approximation (cRPA) [24, 36]. Together with this non-local Coulomb interaction, AbinitioDFA contains all DMFT diagrams, all  $GW$  diagrams and other non-local electronic correlations beyond. In this respect, AbinitioDFA represents a unifying framework.

Here, the AbinitioDFA formalism will be presented step by step starting from the solution of the DMFT impurity model. Then, the inclusion of the non-local Coulomb interaction and the diagrammatic extension through the Bethe-Salpeter equation will be explained. Finally, the equation of motion, that gives the  $\mathbf{k}$ -dependent AbinitioDFA self-energy, is discussed. While the previous chapter provided an overview of DFA and tried to avoid any details, here the AbinitioDFA equations will be presented in full detail, including, in particular, all orbital indices.

#### 4.1.1 Extracting the local irreducible vertex $\Gamma_{\text{loc}}$

The starting point of AbinitioDFA is a converged DMFT computation for the material under investigation. Since AbinitioDFA adopts the ladder approximation of DFA which does not include any self-consistency, the DMFT starting point is really important. Thus, in a first step, a DFT+DMFT study for the material under investigation is performed. This way, the materials' DFT bandstructure, the low-energy Hamiltonian  $H_W^{\mathbf{k}}$  in the basis of maximally localized Wannier functions, and the local DMFT self-energy  $\Sigma(i\nu)$  and one-particle Green's function  $G(i\nu)$  are obtained. Of course, the DMFT cycle involves self-consistency over the one-particle quantities (see Sec. 1.6.3). After convergence of  $\Sigma(i\nu)$  and  $G(i\nu)$  is reached, the two-particle Green's function  $G^{(2)}$  of the DMFT impurity model, which is a necessary ingredient for DFA, is computed. Please note that the two-particle Green's function of the impurity model is computed only once, the DMFT cycle does not involve any self-consistency over two-particle quantities.

**Local Green's functions and symmetries** The multi-orbital definitions of the local one- and two-particle Green's functions read

$$G_{\sigma,lm}(\tau) \equiv -\left\langle \mathcal{T} \left[ \hat{c}_{l\sigma}(\tau) \hat{c}_{m\sigma}^\dagger(0) \right] \right\rangle, \quad (4.1)$$

$$G_{\substack{lmml' \\ \sigma_1\sigma_2\sigma_3\sigma_4}}^{(2)}(\tau_1, \tau_2, \tau_3) \equiv \left\langle \mathcal{T} \left[ \hat{c}_{l\sigma_1}(\tau_1) \hat{c}_{m\sigma_2}^\dagger(\tau_2) \hat{c}_{m'\sigma_3}(\tau_3) \hat{c}_{l'\sigma_4}^\dagger(0) \right] \right\rangle, \quad (4.2)$$

where  $(lmml')$  are orbital indices and  $\sigma_i$  denotes spin. Furthermore,  $\tau \in [0, \beta)$  denotes imaginary time (with the inverse temperature  $\beta$ ) and  $\mathcal{T}$  is the time ordering operator. The computation of the multi-orbital two-particle Green's function in Eq. (4.2) is done

with a continuous-time quantum Monte Carlo solver in the hybridisation expansion (CT-HYB) [106, 107]. This step is numerically very demanding, especially if a non-density-density type of interaction (such as the Kanamori interaction) is employed. In practice, it is done by extending the CT-HYB with a so-called worm algorithm and improved estimators [108, 109].

The fact that, in the absence of spin-orbit coupling, the spin is conserved, reduces the spin degrees of freedom of  $G^{(2)}$  in Eq. (4.2) to the following combinations

$$G_{\sigma\sigma',lmm'l'}^{(2)}(\tau_1, \tau_2, \tau_3) \equiv G_{\substack{lmm'l' \\ \sigma\sigma\sigma'\sigma'}}^{(2)}(\tau_1, \tau_2, \tau_3), \quad (4.3)$$

$$G_{\frac{\sigma\sigma'}{\sigma\sigma'},lmm'l'}^{(2)}(\tau_1, \tau_2, \tau_3) \equiv G_{\substack{lmm'l' \\ \sigma\sigma'\sigma'\sigma}}^{(2)}(\tau_1, \tau_2, \tau_3). \quad (4.4)$$

If we further restrict ourselves to the paramagnetic case, i.e. exclude magnetic long-range order, we can make use of the SU(2) symmetry

$$G_{\sigma\sigma'}^{(2)} = G_{(-\sigma)(-\sigma')}^{(2)} = G_{\sigma'\sigma}^{(2)}, \quad (4.5)$$

$$G_{\sigma\sigma}^{(2)} = G_{\sigma(-\sigma)}^{(2)} + G_{\sigma(-\sigma)}^{(2)}. \quad (4.6)$$

One particularly useful choice of spin combinations are the (d)ensity and (m)agnetic (m) channel

$$G_d^{(2)} = G_{\sigma\sigma}^{(2)} + G_{\sigma(-\sigma)}^{(2)}, \quad (4.7)$$

$$G_m^{(2)} = G_{\sigma\sigma}^{(2)} - G_{\sigma(-\sigma)}^{(2)}. \quad (4.8)$$

By considering SU(2) symmetry (Eqs. (4.5) and (4.6)), the density and magnetic channel can explicitly be written as

$$G_d^{(2)} = \frac{1}{2} \left( G_{\uparrow\uparrow}^{(2)} + G_{\downarrow\downarrow}^{(2)} + G_{\uparrow\downarrow}^{(2)} + G_{\downarrow\uparrow}^{(2)} \right), \quad (4.9)$$

$$G_m^{(2)} = \frac{1}{2} \left( G_{\uparrow\downarrow}^{(2)} + G_{\downarrow\uparrow}^{(2)} \right). \quad (4.10)$$

In CT-HYB, the two-particle Green's function is computed in  $\tau$ -space. Since AbinitioDFA, in its actual implementation, is formulated in frequency space, a Fourier transformation is needed. In the  $ph$ -notation, the Fourier transformation with respect to  $\tau$  is defined as

$$G_{\sigma\sigma',lmm'l'}^{\omega\nu\nu'} = \int_0^\beta \int_0^\beta \int_0^\beta d\tau_1 d\tau_2 d\tau_3 e^{i\nu\tau_1} e^{-i(\nu-\omega)\tau_2} e^{i(\nu'-\omega)\tau_3} G_{\sigma\sigma',lmm'l'}^{(2)}(\tau_1, \tau_2, \tau_3), \quad (4.11)$$

where  $\nu$  and  $\nu'$  denote fermionic and  $\omega$  bosonic Matsubara frequencies. In the chosen frequency convention,  $\omega$  corresponds to a longitudinal transfer of energy from one particle-hole pair ( $ml$ ) to the other ( $m'l'$ ). For simplicity, the superscript (2) has been

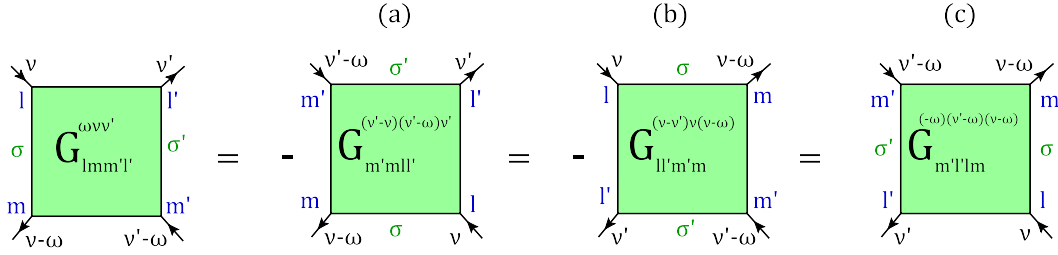


FIGURE 4.1: The crossing symmetries describe the invariance of the two-particle Green's function (up to a global minus sign) under an exchange of (a) the two annihilation or (b) creation operators. In (c) both, annihilation and creation operators, have been exchanged resulting in a full swap of the incoming and outgoing particle labels. In addition to the frequencies  $\omega\nu\nu'$ , also spin  $\sigma\sigma'$  (in green) and orbital indices  $lmm'l'$  (in blue) are shown.

omitted in  $G_{\sigma\sigma',lmm'l'}^{\omega\nu\nu'}$  since the three frequency indices  $\omega\nu\nu'$  already imply that it is a two-particle Green's function.

With respect to the frequencies, the two-particle Green's function also fulfills the so-called crossing symmetries

$$G_{\sigma\sigma',lmm'l'}^{\omega\nu\nu'} = -G_{\sigma'\sigma,m'mll'}^{(\nu'-\nu)(\nu'-\omega)\nu'} \quad (4.12)$$

$$= -G_{\sigma\sigma',ll'm'm}^{(\nu-\nu')\nu(\nu-\omega)} \quad (4.13)$$

$$= G_{\sigma'\sigma,m'l'l'm}^{(-\omega)(\nu'-\omega)(\nu-\omega)}, \quad (4.14)$$

which are a consequence of the Pauli principle for indistinguishable fermions. Exchanging two annihilation [Eq. (4.12)] or creation [Eq. (4.13)] operators in the two-particle Green's function results only in an additional minus sign. In the last crossing relation in Eq. (4.14), both, the creation and the annihilation operators, have been exchanged resulting in a full swap of the incoming and outgoing particle labels. For clarity, the crossing relations are also visualized in Fig. 4.1.

Please note that if we replace the frequency indices  $\omega\nu\nu'$  with bosonic and fermionic compound indices  $qkk'$ , where  $q = (\mathbf{q}, \omega)$ ,  $k = (\mathbf{k}, \nu)$  and  $k' = (\mathbf{k}', \nu')$ , we obtain the *non-local* Green's function. All relations presented so far—including the crossing symmetries in Eqs. (4.12)-(4.14)—can be generalized to the non-local case by this index replacement. Here, however, I stick to the frequency indices  $\omega\nu\nu'$  because this section is devoted to the extraction of  $\Gamma_{\text{loc}}$  from the *local* two-particle impurity Green's function.

The two-particle Green's function itself can be divided into three contributions: two disconnected parts and one connected part. Thus, it can be written as

$$G_{\sigma\sigma',lmm'l'}^{\omega\nu\nu'} = \delta_{\omega 0} G_{\sigma,l m}^{\nu} G_{\sigma',m'l'}^{\nu'} - \delta_{\sigma\sigma'} \delta_{\nu\nu'} G_{\sigma,ll'}^{\nu} G_{\sigma,m'm}^{\nu-\omega} + G_{\sigma\sigma',lmm'l'}^{\text{con } \omega\nu\nu'}. \quad (4.15)$$

$$G_{\sigma\sigma', l m m' l'}^{\omega\nu\nu'} = \text{[disconnected part 1]} + \text{[disconnected part 2]} + \text{[connected part } \chi_{\text{loc}}^{\text{con}} \text{]}.$$

FIGURE 4.2: Ingredients of the local two-particle Green's function  $G_{\sigma\sigma', l m m' l'}^{\omega\nu\nu'}$  in Eq. (4.15). The latter consists of two disconnected and one connected part including the full vertex function  $F_{\text{loc}}$ . Together, the disconnected part denoted with  $\chi_{0,\text{loc}}$  and the connected part  $G^{\text{con}}$  form the generalized susceptibility  $\chi_{\text{loc}}$ . (The frequency convention follows the *ph*-notation.)

The disconnected parts are simply pairs of one-particle Green's functions and represent the non-interacting part of the two-particle Green's function. Thus, they describe the independent propagation of two particles—or a particle and a hole. The connected part  $G^{\text{con}}$  instead contains the full vertex function  $F$  and describes all scattering events. In Fig. 4.2 this relation is shown diagrammatically.

Please note that all one-particle Green's function lines  $G^\nu$  in Fig. 4.2 and Eq. (4.15) are the interacting local DMFT Green's functions. Thus, they are already dressed with the local DMFT self-energy  $\Sigma^\nu$ . Furthermore, in the current implementation, the local DMFT self-energy and Green's function are assumed to be diagonal in the orbital indices:  $G_{\sigma,lm}^\nu \delta_{lm}$  and  $\Sigma_{\sigma,lm}^\nu \delta_{lm}$ . This assumption is based on the fact that most DMFT solvers—in particular the employed w2dynamics CT-HYB solver [42, 51]—consider only orbital-diagonal hybridization functions, which lead to orbital-diagonal DMFT self-energies  $\Sigma_{\sigma,lm}^\nu \delta_{lm}$  and Green's functions  $G_{\sigma,lm}^\nu \delta_{lm}$  (e.g. for  $t_{2g}$  orbitals in a cubic crystal field this holds exactly). In the AbinitioDFA implementation, some small technical advantages, which will briefly be discussed in Sec. 4.2.3, arise with this approximation. However, it is in principle easy to generalize the implementation to orbital-off-diagonal local DMFT self-energies and Green's functions. Hence, here the equations will be presented in general, without assuming  $G_{\sigma,lm}^\nu$  to be orbital-diagonal.

**Local Bethe-Salpeter equation** As it can be seen from Fig. 4.2, the generalized susceptibility  $\chi_{\text{loc}}^{\omega\nu\nu'}$  can be obtained by subtracting the first disconnected term  $\delta_{\omega 0} G_{\sigma,lm}^\nu G_{\sigma',m'l'}^{\nu'}$  from the two-particle Green's function. Thus, the generalized susceptibility  $\chi_{\text{loc}}^{\omega\nu\nu'}$  consists of the disconnected part denoted with  $\chi_{0,\text{loc}}$  in Fig. 4.2 and of the connected part

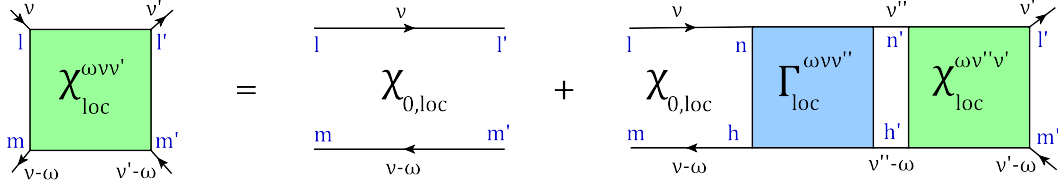


FIGURE 4.3: The local Bethe-Salpeter equation depicted in this figure allows to extract the local irreducible vertex  $\Gamma_{\text{loc}}^{\omega vv'}$  from the generalized susceptibility  $\chi_{\text{loc}}^{\omega vv'}$ .

$G^{\text{con}}$

$$\chi_{0,lm m' l'}^{\omega \nu \nu'} = -\beta G_{ll'}^{\nu} G_{m' m}^{\nu-\omega} \delta_{\nu \nu'}, \quad (4.16)$$

$$G_{r,lm m' l'}^{\text{con } \omega \nu \nu'} = \sum_{nn' hh'} \chi_{0,lm hn}^{\omega \nu \nu} F_{r,nh h' n'}^{\omega \nu \nu'} \chi_{0,n' h' m' l'}^{\omega \nu' \nu'}. \quad (4.17)$$

Please note that all quantities in Eqs. (4.16) and (4.17) are local, even if they do not carry an explicit subscript "loc". Furthermore, the index  $r \in \{d, m\}$  in Eq. (4.17) refers to the particle-hole (d)ensity or (m)agnetic channel since the Bethe-Salpeter equations of AbinitioDΓA are formulated in these channels. By putting Eqs. (4.16) and (4.17) together

$$\chi_{r,lm m' l'}^{\omega \nu \nu'} = \chi_{0,lm m' l'}^{\omega \nu \nu'} \delta_{\nu \nu'} + \sum_{nn' hh'} \chi_{0,lm hn}^{\omega \nu \nu} F_{r,nh h' n'}^{\omega \nu \nu'} \chi_{0,n' h' m' l'}^{\omega \nu' \nu'}, \quad (4.18)$$

and using that

$$\begin{aligned} F_{r,lm m' l'}^{\omega \nu \nu'} &= \Gamma_{r,lm m' l'}^{\omega \nu \nu'} + \phi_{r,lm m' l'}^{\omega \nu \nu'} \\ &= \Gamma_{r,lm m' l'}^{\omega \nu \nu'} + \sum_{nn' hh' \nu''} \Gamma_{r,lm hn}^{\omega \nu \nu''} \chi_{0,nh h' n'}^{\omega \nu'' \nu''} F_{r,n' h' m' l'}^{\omega \nu'' \nu'}, \end{aligned} \quad (4.19)$$

one obtains the Bethe-Salpeter equation for the local generalized susceptibilities in the density and magnetic channel

$$\boxed{\chi_{r,lm m' l'}^{\omega \nu \nu'} = \chi_{0,lm m' l'}^{\omega \nu \nu'} \delta_{\nu \nu'} + \sum_{nn' hh' \nu''} \chi_{0,lm hn}^{\omega \nu \nu''} \Gamma_{r,nh h' n'}^{\omega \nu \nu''} \chi_{r,n' h' m' l'}^{\omega \nu'' \nu'},} \quad (4.20)$$

which is diagrammatically depicted in Fig. 4.3.

The local irreducible vertex function  $\Gamma_{\text{loc}}^{\omega \nu \nu'}$ , which is one main building block of AbinitioDΓA, can now be extracted through an inversion of Eq. (4.20). It is supplemented with the non-local Coulomb interaction  $V^{\mathbf{q}}$  and then used to build the non-local ladder diagrams forming the full non-local vertex function  $F^{\mathbf{q}kk'}$  of the lattice. These steps will be described in more detail in the next sections.



### 4.1.2 The non-local Coulomb interaction $V^{\mathbf{q}}$

Before introducing the non-local Coulomb interaction  $V^{\mathbf{q}}$ , let us first briefly recall the general definition of the Coulomb interaction

$$\hat{U} = \frac{1}{2} \sum_{\substack{\mathbf{R}_1, \mathbf{R}_2, \mathbf{R}_3, \mathbf{R}_4 \\ ll'mm' \\ \sigma\sigma'}} U_{lm'ml'}(\mathbf{R}_1, \mathbf{R}_2, \mathbf{R}_3, \mathbf{R}_4) \hat{c}_{\mathbf{R}_3 m' \sigma}^\dagger \hat{c}_{\mathbf{R}_1 l \sigma'}^\dagger \hat{c}_{\mathbf{R}_2 m \sigma'} \hat{c}_{\mathbf{R}_4 l' \sigma}, \quad (4.21)$$

where  $\mathbf{R}$  denotes the lattice site,  $ll'mm'$  are orbital and  $\sigma\sigma'$  spin indices. The Coulomb interaction fulfills a "particle swapping" symmetry

$$U_{lm'ml'}(\mathbf{R}_1, \mathbf{R}_2, \mathbf{R}_3, \mathbf{R}_4) = U_{m'l'm}(\mathbf{R}_3, \mathbf{R}_4, \mathbf{R}_1, \mathbf{R}_2), \quad (4.22)$$

which corresponds to a swap of the incoming and the outgoing particle. Defining the Fourier transform with respect to  $\mathbf{R}$  in the same way as for  $G^{(2)}$ , yields

$$U_{lm'ml'}^{\mathbf{q}\mathbf{k}\mathbf{k}'} = \sum_{\mathbf{R}_1, \mathbf{R}_2, \mathbf{R}_3} e^{i\mathbf{k}\mathbf{R}_1} e^{-i(\mathbf{k}-\mathbf{q})\mathbf{R}_2} e^{i(\mathbf{k}'-\mathbf{q})\mathbf{R}_3} U_{lm'ml'}(\mathbf{R}_1, \mathbf{R}_2, \mathbf{R}_3, \mathbf{0}); \quad (4.23)$$

or the interaction operator

$$\hat{U} = \frac{1}{2} \sum_{\substack{\mathbf{q}\mathbf{k}\mathbf{k}' \\ ll'mm' \\ \sigma\sigma'}} U_{lm'ml'}^{\mathbf{q}\mathbf{k}\mathbf{k}'} \hat{c}_{\mathbf{k}'-\mathbf{q}m'\sigma}^\dagger \hat{c}_{\mathbf{k}l\sigma'}^\dagger \hat{c}_{\mathbf{k}-\mathbf{q}m\sigma'} \hat{c}_{\mathbf{k}l'\sigma}, \quad (4.24)$$

where  $\hat{c}_{\mathbf{k}l\sigma} = \sum_{\mathbf{R}} e^{i\mathbf{k}\mathbf{R}} \hat{c}_{\mathbf{R}l\sigma}$ . If we neglect the orbital overlap between adjacent unit cells and, in particular, do not consider any non-local exchange, the  $\mathbf{k}$ -point dependence of the Coulomb interaction can be simplified so that the creation and annihilation operators are paired up at site  $\mathbf{0}$  and  $\mathbf{R}$ . This yields a local  $U$  and a purely non-local  $V^{\mathbf{q}}$

$$U_{lm'ml'} \equiv U_{lm'ml'}(\mathbf{0}, \mathbf{0}, \mathbf{0}, \mathbf{0}), \quad (4.25)$$

$$V_{lm'ml'}^{\mathbf{q}} \equiv \sum_{\mathbf{R} \neq \mathbf{0}} e^{i\mathbf{R}\mathbf{q}} U_{lm'ml'}(\mathbf{R}, \mathbf{R}, \mathbf{0}, \mathbf{0}). \quad (4.26)$$

Here, the swapping symmetry reduces to  $U_{lm'ml'} = U_{m'l'm}$  and  $V_{lm'ml'}^{\mathbf{q}} = V_{m'l'm}^{-\mathbf{q}}$ . In practice, the local and non-local Coulomb interaction in Eqs. (4.25) and (4.26) are obtained *ab initio* by using the constrained random phase approximation (cRPA) [35]. For details concerning the cRPA method please refer to Sec. 1.5.

In AbinitioDFA, the local irreducible vertex function  $\Gamma^{\omega\nu\nu'}$  is supplemented by the non-local Coulomb interaction of Eq. (4.26). From a physical point of view, this is a natural extension of  $\Gamma^{\omega\nu\nu'}$  since the latter can be seen as the effective interaction in AbinitioDFA. In fact, the local vertex  $\Gamma^{\omega\nu\nu'}$  already contains the local Coulomb interaction  $U$  as its

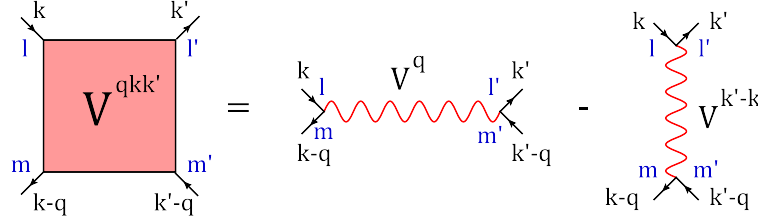


FIGURE 4.4: The crossing-symmetric non-local Coulomb interaction  $\mathbf{V}^{qkk'}$  consists of two terms:  $V^q$  and  $V^{k'-k}$ .

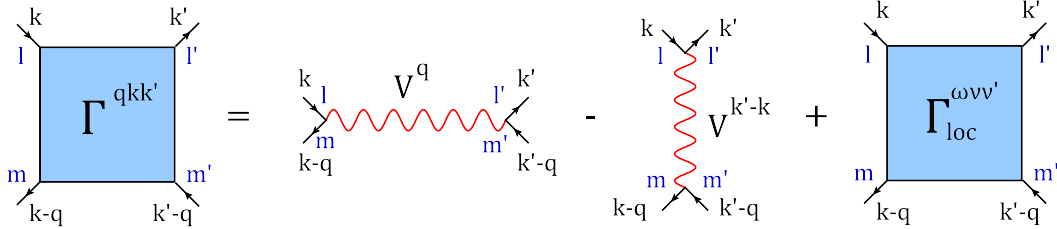


FIGURE 4.5: The local irreducible vertex  $\Gamma_{loc}^{\omega\nu\nu'}$  is supplemented by the non-local Coulomb interaction  $\mathbf{V}^{qkk'}$ .

lowest order contribution. In this sense, in AbinitioDFA the irreducible vertex function is approximated by its local contribution, except for the lowest order term which is taken with its full spatial dependence. However, before the non-local Coulomb interaction is added to  $\Gamma^{\omega\nu\nu'}$ , it needs to be written in the form of a crossing-symmetric vertex. In its crossing-symmetric form, the non-local Coulomb interaction has two contributions

$$\mathbf{V}_{\sigma\sigma',lmm'l'}^{qkk'} = \beta^{-2}(V_{lm'm'l'}^q - \delta_{\sigma\sigma'}V_{mm'll'}^{k'-k}), \quad (4.27)$$

where  $V^q$  depends only on  $\mathbf{q}$ , while the second term  $V^{k'-k}$  depends on  $\mathbf{k}' - \mathbf{k}$ .  $\mathbf{V}^{qkk'}$  can now directly be added to the local irreducible vertex function  $\Gamma^{\omega\nu\nu'}$ , which has been extracted from the DMFT impurity model,

$$\boxed{\Gamma_{\sigma\sigma',lmm'l'}^{qkk'} = \Gamma_{\sigma\sigma',lmm'l'}^{\omega\nu\nu'} + \mathbf{V}_{\sigma\sigma',lmm'l'}^{qkk'}} \quad (4.28)$$

Please note, however, that in the present AbinitioDFA implementation we neglect the  $V^{k'-k}$  term—similar to the  $GW$  approach where  $V^{k'-k}$  is also neglected. This approximation considerably simplifies the AbinitioDFA equations and reduces the numerical effort, as will be shown in the next section.

### 4.1.3 Construction of the full vertex $F^q$

**Non-local Bethe-Salpeter equation** After extracting  $\Gamma_{r,loc}^{\omega\nu\nu'}$  from the DMFT two-particle Green's function and supplementing it with the non-local interaction  $V^q$ , the

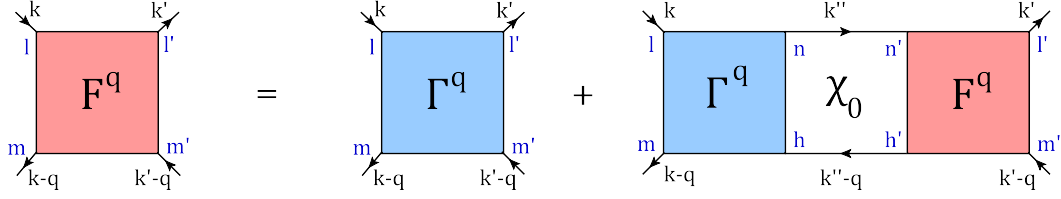


FIGURE 4.6: The non-local Bethe-Salpeter equation is used to obtain the full vertex function  $F^{q\nu\nu'}$ . Please note that here only the longitudinal particle-hole channel is shown, while finally the transversal particle-hole channel is also included.

full vertex of the lattice  $F_r^{qkk'}$  can be obtained through the non-local Bethe-Salpeter equation. The latter is given by

$$\begin{aligned} F_{r,lm m'l'}^{qkk'} &= \Gamma_{r,lm m'l'}^{qkk'} + \phi_{r,lm m'l'}^{qkk'} \\ &= \Gamma_{r,lm m'l'}^{qkk'} + \sum_{nn'h'h'} \Gamma_{r,lm hn}^{qkk''} \chi_{0,nhh'n'}^{qk''k'''} F_{r,n'h'm'l'}^{qk''k'''}, \end{aligned} \quad (4.29)$$

where  $\Gamma_r^{qkk'}$  is the local irreducible vertex in the density or magnetic channel  $r \in \{d, m\}$ , which has been extended by a non-local Coulomb interaction according to Eq. (4.28). Please also note that  $qkk'$  are compound indices that contain also the frequencies  $\omega\nu\nu'$ .  $\chi_0^{qkk}$  is a product of two interacting lattice Green's functions

$$\chi_{0,lm m'l'}^{qkk} = -\beta G_{ll'}^k G_{m'm}^{k-q} \delta_{kk'}, \quad (4.30)$$

where  $G_{ll'}^k$  can explicitly be obtained via  $G_{ll'}^k = \left( i\nu + \mu - H_W^k - \Sigma^\nu \right)_{ll'}^{-1}$ , with  $H_W^k$  being the Wannier Hamiltonian, and  $\Sigma^\nu$  and  $\mu$  the DMFT self-energy and chemical potential, respectively.

Here, we focus on the longitudinal particle-hole ( $ph$ ) channel, since the AbinitioDFA formulation mostly works in this channel. Thus, all quantities without an explicit  $\overline{ph}$  subscript refer to the  $ph$  channel. Let us emphasize, however, that the transversal particle-hole  $\overline{ph}$  channel is finally recovered through the use of the crossing symmetries so that the final expression for the AbinitioDFA self-energy also contains non-local ladder diagrams in the  $\overline{ph}$  channel. The particle-particle ( $pp$ ) channel instead is assumed to be purely local. Thus, the particle-particle diagrams contributing to AbinitioDFA are only the purely local ones contained in  $\Gamma^{\omega\nu\nu'}$ .

The non-local Bethe-Salpeter equation (4.29) can be considerably simplified if  $\Gamma^{qkk'}$  does not depend on the momenta  $\mathbf{k}$  and  $\mathbf{k}'$ . Indeed, this dependence arises only from the second (crossed)  $V^{\mathbf{k}'-\mathbf{k}}$  term in Eq. (4.27) which is neglected e.g. in the  $GW$  approach [110]. If we follow  $GW$  and neglect this term, or average it over  $\mathbf{k}$  (which gives zero since  $V$

was defined as purely non-local), the vertex (in the two spin channels  $r \in \{d, m\}$ ) reads

$$\boxed{\Gamma_{r,lm m'l'}^{q\nu\nu'} = \Gamma_{r,lm m'l'}^{\omega\nu\nu'} + 2\beta^{-2}V_{lm'm'l'}^{\mathbf{q}}\delta_{r,d}.} \quad (4.31)$$

Please note that the non-local Coulomb interaction is present only in the density channel, since we have neglected  $V^{\mathbf{k}'-\mathbf{k}}$ . In fact, the remaining  $V^{\mathbf{q}}$  is not spin-dependent and thus cancels in the magnetic channel  $\Gamma_m = \Gamma_{\sigma\sigma} - \Gamma_{\sigma(-\sigma)}$ .

With this simplification, the non-local Bethe-Salpeter equation becomes

$$F_{r,lm m'l'}^{qkk'} = \Gamma_{r,lm m'l'}^{q\nu\nu'} + \sum_{\substack{nn'h'h' \\ \mathbf{k}''}} \Gamma_{r,lm hn}^{q\nu\nu''} \chi_{0,nhh'n'}^{qk''k'''} F_{r,n'h'm'l'}^{qk''k'}. \quad (4.32)$$

The property that  $\Gamma_r$  is independent of  $\mathbf{k}$  and  $\mathbf{k}'$  carries over to the full vertex in Eq. (4.32). Thus, we can sum over  $\mathbf{k}''$  in Eq. (4.32) and obtain

$$\begin{aligned} F_{r,lm m'l'}^{q\nu\nu'} &= \Gamma_{r,lm m'l'}^{q\nu\nu'} + \phi_{r,lm m'l'}^{q\nu\nu'} \\ &= \Gamma_{r,lm m'l'}^{q\nu\nu'} + \sum_{\substack{nn'h'h' \\ \nu''}} \Gamma_{r,lm hn}^{q\nu\nu''} \chi_{0,nhh'n'}^{q\nu''\nu'''} F_{r,n'h'm'l'}^{q\nu''\nu'}, \end{aligned} \quad (4.33)$$

where

$$\chi_{0,lm m'l'}^{q\nu\nu} = \sum_{\mathbf{k}} \chi_{0,lm m'l'}^{qkk} = -\beta \sum_{\mathbf{k}} G_{ll'}^{\mathbf{k}} G_{m'm}^{\mathbf{k}-\mathbf{q}}. \quad (4.34)$$

Eq. (4.33) is also depicted diagrammatically in Fig. (4.6).

**Compound indices and matrix equations** At this point we now combine the left (right) orbital indices and fermionic Matsubara frequencies into a single compound index  $\{ml, \nu\}$  ( $\{m'l', \nu'\}$ ), as it is also done in the numerical implementation of the equations. This way, all employed quantities can be written in matrix form, e.g.  $F_{r,lm m'l'}^{q\nu\nu'} \rightarrow F_{r\{ml\nu\}\{m'l'\nu'\}}^q \rightarrow F_r^q$ . Thus, Eq. (4.33) can be written as a matrix equation in terms of compound indices

$$F_r^q = \Gamma_r^q + \Gamma_r^q \chi_0^q F_r^q. \quad (4.35)$$

The full vertex  $F_r^q$  can now, in principle, be extracted from Eq. (4.35) through a simple matrix inversion

$$\boxed{F_r^q = [(\Gamma_r^q)^{-1} - \chi_0^q]^{-1}.} \quad (4.36)$$

However, as recently shown in Ref. [99], the  $\Gamma_{\text{loc}}$  extracted from a self-consistent DMFT calculation contains an infinite set of diverging components (please remind that  $\Gamma_{\text{loc}}$  is contained in  $\Gamma^q$ ). In order to avoid the numerical complications associated with these

divergencies, we use Eqs. (4.19) and (4.31) to substitute  $\Gamma_r^q$  in Eq. (4.36) by

$$\Gamma_r^q = \frac{F_r^\omega}{\mathbf{1} + \chi_0^\omega F_r^\omega} + 2\beta^{-2} V^q \delta_{r,d}. \quad (4.37)$$

This yields for the full vertex  $F_r^q$  in the density and magnetic channel

$$F_d^q = \left( F_d^\omega + 2\beta^{-2} V^q (\mathbf{1} + \chi_0^\omega F_d^\omega) \right) \left[ \mathbf{1} - \chi_0^{nl,q} F_d^\omega - 2\beta^{-2} \chi_0^q V^q (\mathbf{1} + \chi_0^\omega F_d^\omega) \right]^{-1}, \quad (4.38)$$

$$F_m^q = F_m^\omega \left[ \mathbf{1} - \chi_0^{nl,q} F_m^\omega \right]^{-1}, \quad (4.39)$$

where the purely non-local  $\chi_0^{nl}$  has been defined as

$$\chi_0^{nl,q} \equiv \chi_0^q - \chi_0^\omega. \quad (4.40)$$

This formulation is equivalent to Eq. (4.36) but circumvents the aforementioned divergencies in  $\Gamma_{\text{loc}}$ , since the latter does no longer have to be inverted explicitly.

**Including the  $\overline{ph}$  channel through the crossing symmetries** The full non-local vertices in Eqs. (4.38) and (4.39) are not crossing-symmetric, since they were generated through the Bethe-Salpeter equation in the particle-hole channel only. In fact, the Bethe-Salpeter equation carries only the "swapping" symmetry of the two-particle Green's function in Eq. (4.14) over to  $\Gamma$  and  $\phi$ , but not the other two crossing symmetries in Eqs. (4.12) and (4.13). However, the crossing symmetry of the full non-local  $\mathbf{F}$  can be restored by explicitly adding the corresponding diagrams of the transversal particle-hole channel (as it has been done before for a single orbital in Refs. [7, 111]). Thus, in the parquet equation (3.5), we add the reducible contributions  $\phi$  in the particle-hole and transversal particle-hole channel, and subtract their respective local contributions which are already contained in the local  $F$ :

$$\mathbf{F}_{d,lm m' l'}^{qkk'} = F_{d,lm m' l'}^{\omega\nu\nu'} + \mathbf{V}_{d,lm m' l'}^{qkk'} + (\phi_{d,lm m' l'}^{q\nu\nu'} - \phi_{d,lm m' l'}^{\omega\nu\nu'}) + (\phi_{ph,d,lm m' l'}^{qkk'} - \phi_{ph,d,lm m' l'}^{\omega\nu\nu'}). \quad (4.41)$$

Please note that again all quantities in the transversal particle-hole channel carry an explicit subscript  $\overline{ph}$ , while for the longitudinal particle-hole channel the  $ph$  subscript is omitted, since the latter is the "default" channel for the formulation of the AbinitioDFA equations. In Eq. (4.41) all diagrams in the particle-particle channel and all fully irreducible diagrams, except  $\mathbf{V}^{qkk'}$ , are considered to be local. The bare non-local interaction vertex  $\mathbf{V}^{qkk'}$  defined in Eq. (4.27) has to be added explicitly to the parquet equation since it is neither part of the reducible vertices  $\phi_{ph}$  and  $\phi_{\overline{ph}}$ , nor the local  $F$ .

Now we resolve the local and non-local Bethe-Salpeter equations (4.19) and (4.33) for  $\phi_d^{\omega\nu\nu'}$  and  $\phi_d^{q\nu\nu'}$ , and then explicitly express  $\Gamma_d^{q\nu\nu'}$  through Eq. (4.31). This yields

$$\begin{aligned} (\phi_{d,lm m'l'}^{q\nu\nu'} - \phi_{d,lm m'l'}^{\omega\nu\nu'}) &= (F_{d,lm m'l'}^{q\nu\nu'} - \Gamma_{d,lm m'l'}^{q\nu\nu'}) - (F_{d,lm m'l'}^{\omega\nu\nu'} - \Gamma_{d,lm m'l'}^{\omega\nu\nu'}) \\ &= (F_{d,lm m'l'}^{q\nu\nu'} - \Gamma_{d,lm m'l'}^{\omega\nu\nu'} - 2\beta^{-2}V_{lm'ml'}^q) - (F_{d,lm m'l'}^{\omega\nu\nu'} - \Gamma_{d,lm m'l'}^{\omega\nu\nu'}) \\ &= F_{d,lm m'l'}^{nl,q\nu\nu'} - 2\beta^{-2}V_{lm'ml'}^q, \end{aligned} \quad (4.42)$$

where the purely non-local vertex  $F^{nl}$  has been defined as

$$F_{r,lm m'l'}^{nl,q\nu\nu'} \equiv F_{r,lm m'l'}^{q\nu\nu'} - F_{r,lm m'l'}^{\omega\nu\nu'}. \quad (4.43)$$

We can optimize the AbinitioDΓA computations by expressing the difference in the transversal particle-hole channel  $\overline{ph}$  in Eq. (4.41), namely  $(\phi_{ph,d}^{qkk'} - \phi_{ph,d}^{\omega\nu\nu'})$ , in terms of the longitudinal particle-hole channel  $ph$ . Thus, we make use of the fact that the transversal particle-hole channel ( $\overline{ph}$ ) is by definition crossing-symmetric to the particle-hole channel, i.e. antisymmetric to the particle-hole channel with respect to a relabeling of the two incoming or outgoing particles. In particular, this yields

$$\phi_{ph,\sigma\sigma',lm m'l'}^{\omega\nu\nu'} = -\phi_{\sigma'\sigma,m'mll'}^{(\nu'-\nu)(\nu'-\omega)\nu'}. \quad (4.44)$$

By using the definition of the density and magnetic channel in Eqs. (4.7) and (4.8), and by applying the SU(2) symmetry in Eq. (4.6) and the symmetry relation in Eq. (4.44), one can explicitly express the  $\overline{ph}$  density channel in terms of the  $ph$  density and magnetic channel. This yields

$$\begin{aligned} \phi_{ph,d,lm m'l'}^{\omega\nu\nu'} &= \phi_{ph,\sigma\sigma,lm m'l'}^{\omega\nu\nu'} + \phi_{ph,\sigma(-\sigma),lm m'l'}^{\omega\nu\nu'} \\ &= -\phi_{\sigma\sigma,m'mll'}^{(\nu'-\nu)(\nu'-\omega)\nu'} - \phi_{\sigma(-\sigma),m'mll'}^{(\nu'-\nu)(\nu'-\omega)\nu'} \\ &= -\frac{1}{2} \left( \phi_{d,m'mll'}^{(\nu'-\nu)(\nu'-\omega)\nu'} + \phi_{m,m'mll'}^{(\nu'-\nu)(\nu'-\omega)\nu'} \right) - \phi_{m,m'mll'}^{(\nu'-\nu)(\nu'-\omega)\nu'} \\ &= -\frac{1}{2} \phi_{d,m'mll'}^{(\nu'-\nu)(\nu'-\omega)\nu'} - \frac{3}{2} \phi_{m,m'mll'}^{(\nu'-\nu)(\nu'-\omega)\nu'}, \end{aligned} \quad (4.45)$$

or in the non-local case

$$\phi_{ph,d,lm m'l'}^{qkk'} = -\frac{1}{2} \phi_{d,m'mll'}^{(k'-k)(k'-q)k'} - \frac{3}{2} \phi_{m,m'mll'}^{(k'-k)(k'-q)k'}. \quad (4.46)$$

By subtracting Eq. (4.45) from (4.46) and expressing all terms by  $F$ —similar as we did for Eq. (4.42)—, we obtain

$$(\phi_{ph,d,lmm'l'}^{qkk'} - \phi_{ph,d,lmm'l'}^{\omega\nu\nu'}) = -\frac{1}{2}F_{d,m'mll'}^{nl,(k'-k)(\nu'-\omega)\nu'} - \frac{3}{2}F_{m,m'mll'}^{nl,(k'-k)(\nu'-\omega)\nu'} + \beta^{-2}V_{m'lm'l'}^{k'-k}. \quad (4.47)$$

Eqs. (4.42) and (4.47) can now be used in Eq. (4.41) to finally give

$$\boxed{\mathbf{F}_{d,lmm'l'}^{qkk'} = F_{d,lmm'l'}^{\omega\nu\nu'} + F_{d,lmm'l'}^{nl,q\nu\nu'} - \frac{1}{2}F_{d,m'mll'}^{nl,(k'-k)(\nu'-\omega)\nu'} - \frac{3}{2}F_{m,m'mll'}^{nl,(k'-k)(\nu'-\omega)\nu'}}. \quad (4.48)$$

Please note that the two non-crossing symmetric contributions to the bare non-local interaction  $V$  in Eq. (4.42) and (4.47) add up to become exactly  $V^{qkk'}$  as defined in Eq. (4.27). This is a unique property of the simplification employed in Eq. (4.31).

#### 4.1.4 Equation of motion

Once the crossing-symmetric full vertex function  $F^{qkk'}$  is obtained, the AbinitioDFA self-energy can be calculated through the Schwinger-Dyson equation of motion, which has already been introduced in Eq. (3.12) for the single-orbital case. In order to derive the multi-orbital Schwinger-Dyson equation, we first compare the  $\tau$ -derivative of  $G_{\sigma,lm}^k(\tau)$  in the Heisenberg equation of motion with the Dyson equation. This yields

$$\begin{aligned} [\Sigma G]_{\sigma,mm'}^k(\tau) &= \left\langle \mathcal{T} \left[ \left[ \hat{U}^{\text{full}}, \hat{c}_{\mathbf{k}m\sigma}(\tau) \right] \hat{c}_{\mathbf{k}m'\sigma}^\dagger(0) \right] \right\rangle \\ &= \sum_{\substack{lh n \sigma' \\ \mathbf{q} \mathbf{k}'}} (U_{mlhn} + V_{mlhn}^{\mathbf{q}}) \left\langle \mathcal{T} \left[ \hat{c}_{\mathbf{k}'-\mathbf{q}l\sigma'}^\dagger(\tau) \hat{c}_{\mathbf{k}-\mathbf{q}h\sigma}(\tau) \hat{c}_{\mathbf{k}'n\sigma'}(\tau) \hat{c}_{\mathbf{k}m'\sigma}^\dagger(0) \right] \right\rangle \\ &= \lim_{\tau' \rightarrow \tau^+} \sum_{\substack{lh n \sigma' \\ \mathbf{q} \mathbf{k}'}} (U_{mlhn} + V_{mlhn}^{\mathbf{q}}) G_{\sigma'\sigma,nlhm'}^{qk'k}(\tau, \tau', \tau). \end{aligned} \quad (4.49)$$

The limit in Eq. (4.49) can be taken by splitting the two-particle Green's function into its connected and disconnected parts

$$\begin{aligned} [\Sigma G]_{\sigma,mm'}^k(\tau) &= \sum_{\substack{lh n \sigma' \\ \mathbf{q} \mathbf{k}'}} (U_{mlhn} + V_{mlhn}^{\mathbf{q}}) \times \left[ G_{\sigma'\sigma,nlhm'}^{\text{con } qk'k}(\tau, \tau, \tau) + \right. \\ &\quad \left. + \delta_{\mathbf{q}0} n_{\sigma',ln}^{\mathbf{k}'} G_{\sigma',hm'}^{\mathbf{k}}(\tau) - \delta_{\sigma\sigma'} \delta_{\mathbf{k}\mathbf{k}'} n_{\sigma,lh}^{\mathbf{k}-\mathbf{q}} G_{\sigma,nm'}^{\mathbf{k}}(\tau) \right], \end{aligned} \quad (4.50)$$

where  $n_{mm'} = \langle \hat{c}_m^\dagger \hat{c}_{m'} \rangle$ . As Eq. (4.50) already indicates, the two disconnected parts of the two-particle Green's function will finally give the Hartree and the Fock contribution to the AbinitioDFA self-energy. In the next step, we take the Fourier transform of

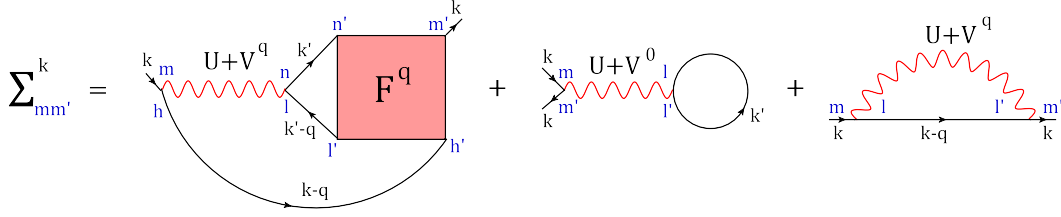


FIGURE 4.7: The AbinitioDFA self-energy is obtained from the full vertex  $F^{\mathbf{q}}$  through the Schwinger-Dyson equation of motion. In addition, the Hartree and Fock contributions are added, which can be traced back to the disconnected parts of the two-particle Green's function.

Eq. (4.50) with respect to  $\tau$ :

$$[\Sigma G]_{\sigma,mm'}^k = \sum_{\substack{lh n \sigma' \\ \mathbf{q} \mathbf{k}'}} (U_{mlhn} + V_{mlhn}^{\mathbf{q}}) \times \left[ \int_0^\beta e^{i\nu\tau} G_{\sigma'\sigma, n l h m'}^{\text{con } \mathbf{q} \mathbf{k}' \mathbf{k}}(\tau, \tau, \tau) d\tau + \delta_{\mathbf{q}0} n_{\sigma',ln}^{\mathbf{k}'} G_{\sigma',hm'}^k - \delta_{\sigma\sigma'} \delta_{\mathbf{k}\mathbf{k}'} n_{\sigma, lh}^{\mathbf{k}-\mathbf{q}} G_{\sigma, nm'}^k \right]. \quad (4.51)$$

Since the connected part is continuous, it is possible to obtain the equal time component in Eq. (4.51) by simply summing up the bosonic and the left fermionic Matsubara frequencies

$$\int_0^\beta d\tau e^{i\nu\tau} G_{\sigma'\sigma, n l m'}^{\text{con } \mathbf{q} \mathbf{k}' \mathbf{k}}(\tau, \tau, \tau) = \frac{1}{\beta^2} \sum_{\omega\nu'} G_{\sigma'\sigma, n l m'}^{\text{con } \mathbf{q} \mathbf{k}' \mathbf{k}}. \quad (4.52)$$

In order to obtain the multi-orbital Schwinger-Dyson equation for the self-energy, one now just needs to multiply Eq. (4.51) with  $G^{-1}$  from the right. This yields

$$\Sigma_{\sigma,mm'}^k = \Sigma_{\sigma,mm'}^{\text{HF } \mathbf{k}} + \Sigma_{\sigma,mm'}^{\text{con } \mathbf{k}}, \quad (4.53)$$

$$\Sigma_{\sigma,mm'}^{\text{con } \mathbf{k}} = \beta^{-2} \sum_{\substack{ll'hn \\ \sigma' \mathbf{q} \mathbf{k}'}} (U_{mlhn} + V_{mlhn}^{\mathbf{q}}) G_{\sigma'\sigma, n l h l'}^{\text{con } \mathbf{q} \mathbf{k}' \mathbf{k}} [G_{\sigma'}^k]_{l'm'}^{-1}. \quad (4.54)$$

$\Sigma^{\text{HF}}$  is the static Hartree-Fock contribution to the self-energy, which stems from the disconnected parts of Eq. (4.51) and reads

$$\Sigma_{\sigma,mm'}^{\text{HF } \mathbf{k}} = \sum_{ll' \mathbf{k}' \sigma'} (U_{mlm'l'} + V_{mlm'l'}^{\mathbf{q}=0}) n_{\sigma', ll'}^{\mathbf{k}'} - \sum_{ll' \mathbf{q}} (U_{mll'm'} + V_{mll'm'}^{\mathbf{q}}) n_{\sigma, ll'}^{\mathbf{k}-\mathbf{q}}. \quad (4.55)$$

The connected part of the self-energy  $\Sigma^{\text{con}}$  we express in terms of the full vertex  $F$  using the relation in Eq. (4.17). This yields

$$\Sigma_{mm'}^{\text{con } \mathbf{k}} = -\beta^{-1} \sum_{ll'nn'hh' \mathbf{q} \mathbf{k}'} (U_{mlhn} + V_{mlhn}^{\mathbf{q}}) \chi_{0, n l l' n'}^{\mathbf{q} \mathbf{k}' \mathbf{k}} F_{d, n l' l' h' m'}^{\mathbf{q} \mathbf{k}' \mathbf{k}} G_{hh'}^{\mathbf{k}-\mathbf{q}}. \quad (4.56)$$

This relation is depicted diagrammatically in Fig. (4.7), together with the static Hartree and Fock contribution of Eq. (4.55).



In order to derive the version of the equation of motion that is actually implemented, Eq. (4.56) is split into contributions stemming from the longitudinal and the transversal particle-hole channel, as well as  $U$  and  $V^{\mathbf{q}}$  terms. Explicitly:

$$\Sigma^{Uloc,k} \equiv -\beta^{-1} \sum_{\mathbf{q}\nu'} U \chi_0^{\mathbf{q}\nu'\nu'} F_d^{\omega\nu'\nu} G^{\mathbf{k}-\mathbf{q}}, \quad (4.57)$$

$$\Sigma^{Vloc,k} \equiv -\beta^{-1} \sum_{\mathbf{q}\nu'} V^{\mathbf{q}} \chi_0^{\mathbf{q}\nu'\nu'} F_d^{\omega\nu'\nu} G^{\mathbf{k}-\mathbf{q}}, \quad (4.58)$$

$$\Sigma^{ph,k} \equiv -\beta^{-1} \sum_{\mathbf{q}\nu'} (U + V^{\mathbf{q}}) \chi_0^{\mathbf{q}\nu'\nu'} F_d^{nl,\mathbf{q}\nu'\nu} G^{\mathbf{k}-\mathbf{q}}, \quad (4.59)$$

$$\Sigma^{U\overline{ph},k} \equiv -\beta^{-1} \sum_{\mathbf{q}\nu'} \tilde{U} \chi_0^{\mathbf{q}\nu'\nu'} \left( \frac{1}{2} F_d^{nl,\mathbf{q}\nu'\nu} + \frac{3}{2} F_m^{nl,\mathbf{q}\nu'\nu} \right) G^{\mathbf{k}-\mathbf{q}}, \quad (4.60)$$

$$\Sigma^{V\overline{ph},k} \equiv -\beta^{-1} \sum_{\mathbf{q}\nu'} \tilde{V}^{\mathbf{k}'-\mathbf{k}} \chi_0^{\mathbf{q}\mathbf{k}'\mathbf{k}'} \left( \frac{1}{2} F_d^{nl,\mathbf{q}\nu'\nu} + \frac{3}{2} F_m^{nl,\mathbf{q}\nu'\nu} \right) G^{\mathbf{k}-\mathbf{q}}, \quad (4.61)$$

where all orbital indices, which remain the same as in Eq. (4.56), have been suppressed for clarity. Please note that  $\tilde{U}_{lm'l'm} = U_{lm'ml'}$  and similarly for  $V$ . The self-energy contribution  $\Sigma^{Uloc,k}$  in Eq. (4.57) contains the local DMFT self-energy  $\Sigma_{\text{DMFT}}^{\nu}$ . In fact, with the purely non-local  $\chi_0^{nl,\mathbf{q}\nu\nu}$  defined in Eq. (4.40), we can rewrite Eq. (4.57) as

$$\begin{aligned} \Sigma^{Uloc,k} &= -\beta^{-1} \sum_{\mathbf{q}\nu'} U \left( \chi_0^{\omega\nu'\nu'} + \chi_0^{nl,\mathbf{q}\nu'\nu'} \right) F_d^{\omega\nu'\nu} G^{\mathbf{k}-\mathbf{q}} \\ &= \Sigma_{\text{DMFT}}^{\nu} - \beta^{-1} \sum_{\mathbf{q}\nu'} U \chi_0^{nl,\mathbf{q}\nu'\nu'} F_d^{\omega\nu'\nu} G^{\mathbf{k}-\mathbf{q}}. \end{aligned} \quad (4.62)$$

Furthermore, in the non-local Bethe-Salpeter ladders we have, in Eq. (4.31) and similar to  $GW$ , included  $V^{\mathbf{q}}$  but not  $V^{\mathbf{k}'-\mathbf{k}}$ . Against this background it is reasonable to omit the contribution  $\Sigma^{V\overline{ph}}$  of Eq. (4.61).

**Formulation with three-leg vertices** In the following we will take advantage of the particular momentum and frequency structure of the Schwinger-Dyson equation to optimize the numerical calculation of the self-energy. Thus, we define three three-leg vertices (cf. Refs. [95, 111]) with increasing order of non-local character:

$$\gamma_{r,lmn'l'}^{\omega\nu} \equiv \sum_{n'h'\nu'} \chi_{0,lmn'h'}^{\omega\nu'\nu'} F_{r,h'n'm'l'}^{\omega\nu'\nu}, \quad (4.63)$$

$$\gamma_{r,lmn'l'}^{\mathbf{q}\nu} \equiv \sum_{n'h'\nu'} \chi_{0,lmn'h'}^{nl,\mathbf{q}\nu'\nu'} F_{r,h'n'm'l'}^{\omega\nu'\nu}, \quad (4.64)$$

$$\eta_{r,lmn'l'}^{\mathbf{q}\nu} \equiv \sum_{n'h'\nu'} \chi_{0,lmn'h'}^{\mathbf{q}\nu'\nu'} F_{r,h'n'm'l'}^{\mathbf{q}\nu'\nu} - \chi_{0,lmn'h'}^{\omega\nu'\nu'} F_{r,h'n'm'l'}^{\omega\nu'\nu}. \quad (4.65)$$

The completely local  $\gamma^{\omega\nu}$  can directly be extracted from the impurity solver [109, 112].  $\gamma^{\mathbf{q}\nu}$  instead contains the local full vertex connected to a purely non-local  $\chi_0^{nl,\mathbf{q}\nu\nu}$  as

defined in Eq. (4.40). The three-leg vertex  $\eta^{q\nu}$  describes the full vertex connected to the full  $\chi_0^{q\nu\nu}$ , but with  $\gamma_r^\omega$ —which means all purely local diagrams—removed.  $\eta^{q\nu}$  can be calculated efficiently from Eqs. (4.38) and ((4.39)) using a matrix inversion and  $\gamma_r^\omega$ :

$$\eta_r^q = (\vec{\mathbf{1}} + \gamma_r^\omega) \left( \left[ \mathbf{1} - \chi_0^{nl,q} F_r^\omega - 2\beta^{-2} \chi_0^q V^q (\vec{\mathbf{1}} + \gamma_r^\omega) \delta_{rd} \right]^{-1} - \mathbf{1} \right), \quad (4.66)$$

where  $\vec{\mathbf{1}}_{lmm'l'} = \delta_{ll'} \delta_{mm'}$ . Now the contributions to the AbinitioDFA self-energy can be written in terms of the three-leg quantities defined in Eqs. (4.63)-(4.65):

$$\Sigma^{Uloc,k} = \Sigma_{\text{DMFT}}^\nu - \beta^{-1} \sum_q U \gamma_d^q G^{k-q}, \quad (4.67)$$

$$\Sigma^{Vloc,k} = -\beta^{-1} \sum_q V^q (\gamma_d^q + \gamma_d^\omega) G^{k-q}, \quad (4.68)$$

$$\Sigma^{ph,k} = -\beta^{-1} \sum_q \left( U + V^q \right) (\eta_d^q - \gamma_d^q) G^{k-q}, \quad (4.69)$$

$$\Sigma^{U\overline{ph},k} = \beta^{-1} \sum_q \tilde{U} \left[ \frac{1}{2} (\eta_d^q - \gamma_d^q) + \frac{3}{2} (\eta_m^q - \gamma_m^q) \right] G^{k-q}. \quad (4.70)$$

By gathering the terms and using the crossing symmetry of the local  $F$  in  $\gamma^q$ , one finally obtains the AbinitioDFA self-energy in the compact form, which is actually implemented in the AbinitioDFA program,

$$\begin{aligned} \Sigma^{\text{DFA}} &= \Sigma^{Uloc,k} + \Sigma^{Vloc,k} + \Sigma^{ph,k} + \Sigma^{U\overline{ph}} \\ &= \Sigma_{\text{DMFT}}^\nu - \beta^{-1} \sum_q \left( U + V^q - \frac{\tilde{U}}{2} \right) \eta_d^q G^{k-q} + \\ &\quad + \beta^{-1} \sum_q \frac{3}{2} \tilde{U} \eta_m^q G^{k-q} - \beta^{-1} \sum_q \left( V^q \gamma_d^\omega - U \gamma_d^q \right) G^{k-q}. \end{aligned} \quad (4.71)$$

## 4.2 Implementational details

One main part of this PhD thesis has been the implementation of the AbinitioDFA equations presented in the previous section. Thus, in the following I will discuss some algorithmic details concerning the newly developed AbinitioDFA program. These rather technical issues will facilitate future developments and extensions.

Fig. 4.8 presents an overview of the AbinitioDFA algorithm in its current implementation. There, all necessary steps are depicted in the form of a flow-diagram. In addition, important names of employed programs and input/output files are given. The single steps will be discussed in detail in the following.

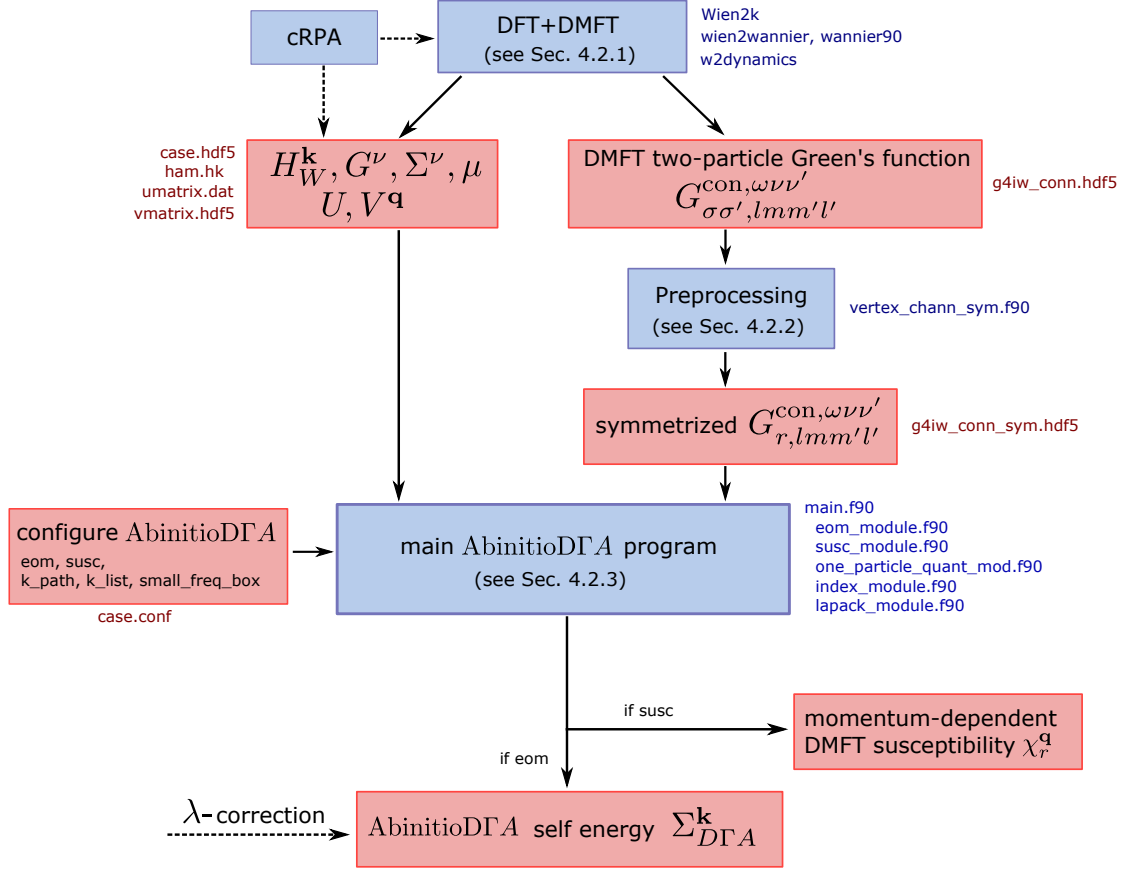


FIGURE 4.8: Flow diagram of the AbinitioDFA algorithm. Programs are indicated as blue boxes with the main program and module names listed on the right. The input/output data files instead are indicated in red.

#### 4.2.1 DFT+DMFT computation

As Fig. 4.8 shows, the starting point of AbinitioDFA is a converged DFT+DMFT calculation for the material under investigation. Here, we use the Wien2k program package [19, 113] to perform the DFT computation, the wien2wannier interface [49] and wannier90 [50] to construct the Wannier Hamiltonian  $H_W^k$ , and the w2dynamics CT-QMC program [42, 51] to solve the DMFT impurity model. This way, we obtain all single-particle quantities which are used in AbinitioDFA: the wien2wannier Hamiltonian  $H_W^k$ , the local DMFT one-particle Green's function  $G^\nu$  and self-energy  $\Sigma^\nu$ , as well as the chemical potential  $\mu$ . The wien2wannier Hamiltonian  $H_W^k$  is stored in the file *ham.hk*, while all the other DMFT single-particle quantities can be found in the *hdf5* file *case.hdf5* which has the usual w2dynamics output format. The local and non-local Coulomb interaction  $U$  and  $V^q$  can also be obtained *ab initio* by using the constrained random phase approximation (cRPA) [114, 115]. For details about the cRPA method please refer to Sec. 1.5. The four-index  $U$  and  $V^q$  are currently stored in two separate files *umatrix.dat* and *vmatrix.hdf5*.

After convergence of the DFT+DMFT computation, the connected part of the DMFT two-particle Green's function  $G^{\text{con}}$  is computed which is a numerically very demanding task. In practice,  $G^{\text{con}}$  is calculated within the w2dynamics program package by extending the CT-HYB with a worm algorithm and improved estimators [108, 109]. Then it is stored in the file *g4iw\_conn.hdf5*, whose structure will be discussed in the following.

**Storage of the DMFT two-particle Green's function** The connected part of the local two-particle Green's function  $G_{\sigma_1\sigma_2\sigma_3\sigma_4,lm m'l'}^{\text{con } \omega\nu\nu'}$ , which is measured in CT-HYB, is a very large quantity and needs a lot of storage capacity. In fact, in its most general form it has four orbital indices  $lm m'l'$  and four spin indices  $\sigma_1\sigma_2\sigma_3\sigma_4$ , and it depends on three Matsubara frequencies  $\omega\nu\nu'$ . Due to numerical limitations,  $G^{\text{con}}$  cannot be measured on an arbitrary big Matsubara frequency grid. However, in order to obtain decent results within AbinitioDFA, the size of the bosonic and fermionic frequency boxes should be reasonably big in order to reach the asymptotic region of  $G^{\text{con}}$ . Furthermore, to deserve the name "multi-orbital", the two-particle Green's function will capture at least 2-3 orbitals. If we assume the case of three orbitals—e.g. the three  $t_{2g}$  orbitals in  $\text{SrVO}_3$ —, then we have  $3^4 = 81$  orbital degrees of freedom, together with  $2^4 = 16$  spin degrees of freedom. However, the orbital and spin degrees of freedom are usually restricted by the symmetry of the interaction of the local DMFT impurity problem. The Kanamori interaction in Eq. (2.1), which we usually employ, allows only for orbital combinations where two orbitals are the same ( $ijjj$ ,  $ijij$ ,  $ijji$ ). Thus, for three orbitals, the number of possible orbital combinations is reduced to 21. Furthermore, according to Eqs. (4.3) and (4.4), also the spin degrees of freedom are reduced to six per orbital combination. Hence, in total, the originally 81x16 spin-orbital combinations are reduced to 21x6=126 non-zero components in the three-orbital case.

**Group structure of the file *g4iw\_conn.hdf5*** In an attempt to decrease the amount of storage for  $G^{\text{con}}$ , we store only its non-zero spin-orbital components in *hdf5* file format. The latter is a hierarchical data model, which allows us to handle complex and large amounts of data in an effective way. In particular, it allows us to create groups that contain datasets. This feature we use to store the non-zero spin-orbital components of  $G_{\sigma_1\sigma_2\sigma_3\sigma_4,lm m'l'}^{\text{con } \omega\nu\nu'}$  in the form of a "lookup-table". This means that we translate the band and spin indices of  $G_{\sigma_1\sigma_2\sigma_3\sigma_4,lm m'l'}^{\text{con } \omega\nu\nu'}$  into a single index  $\Omega$  through a unique transformation:

$$\sigma_1\sigma_2\sigma_3\sigma_4,lm m'l' \leftrightarrow \Omega. \quad (4.72)$$

For each spin-orbital component we can now simply "look up" the corresponding  $\Omega$  and also the other way around (this is done by the subroutines *component2index* and

groupname $\Omega$		$G_{\Omega}^{\text{con } \omega\nu\nu'}$
00001	→	$G_{\uparrow\uparrow\uparrow\uparrow,1111}^{\text{con } \omega\nu\nu'}$
00008	→	$G_{\uparrow\uparrow\downarrow\downarrow,1111}^{\text{con } \omega\nu\nu'}$
00015	→	$G_{\uparrow\uparrow\uparrow\uparrow,1122}^{\text{con } \omega\nu\nu'}$
00022	→	$G_{\uparrow\uparrow\downarrow\downarrow,1122}^{\text{con } \omega\nu\nu'}$
⋮		⋮

FIGURE 4.9: Structure of the file *g4iw\_conn.hdf5*, which contains the two-particle impurity Green's function  $G^{\text{con}}$  measured in CT-HYB (w2dynamics). Each group named by the combined index  $\Omega$  contains the corresponding non-zero spin-orbital component of  $G^{\text{con}}$ . Shown are the first four groups in the SrVO<sub>3</sub>-file. Note that many spin-orbital combinations do not exist, e.g.  $\Omega = 2$  which corresponds to  $G_{\uparrow\uparrow\uparrow\uparrow,1111}^{\text{con } \omega\nu\nu'}$ , and are hence not stored.

*index2component*, respectively). The combined index  $\Omega$  is at the same time also the name of the group in the file *g4iw\_conn.hdf5* where  $G_{\sigma_1\sigma_2\sigma_3\sigma_4,lmm'l'}^{\text{con } \omega\nu\nu'} = G_{\Omega}^{\text{con } \omega\nu\nu'}$  is stored. Thus, *g4iw\_conn.hdf5* contains as many groups as there are non-zero spin-orbital components in  $G_{\sigma_1\sigma_2\sigma_3\sigma_4,lmm'l'}^{\text{con } \omega\nu\nu'}$ . Each of these groups contains a dataset with the corresponding  $G_{\Omega}^{\text{con } \omega\nu\nu'}$  for all bosonic and fermionic Matsubara frequencies. For example, for SrVO<sub>3</sub> the structure of the *g4iw\_conn.hdf5* file is shown in Fig. 4.9. For SrVO<sub>3</sub> in a paramagnetic  $t_{2g}$  setup with Kanamori interactions, the file contains 126 groups and thus 126 non-zero spin-orbital components of  $G^{\text{con}}$ . Together with a box of 120 bosonic and fermionic Matsubara frequencies, this yields 4GB.

Please note that this way of storing the two-particle impurity Green's function is not limited to density or Kanamori kind of interactions. It can also be used for a general, full Coulomb interaction. In case of the latter, the file would simply contain more non-zero spin-orbital components of  $G^{\text{con}}$ , which means more groups.

#### 4.2.2 Preprocessing of the AbinitioDFA input data

Before starting the main AbinitioDFA program, the file *g4iw\_conn.hdf5* containing the connected part of the two-particle impurity Green's function  $G^{\text{con}}$  is pre-processed. The format of *g4iw\_conn.hdf5*, which is produced by the w2dynamics program package and has been presented above, is in principle a good starting point for performing AbinitioDFA. However, the preprocessing script *vertex\_chann\_sym.f90* prepares the AbinitioDFA input data—namely  $G^{\text{con}}$ —in a way that best fits the needs of the main

AbinitioDFA program. In this preprocessing step, the connected part of the two-particle impurity Green's function is symmetrized [SU(2) and orbital symmetry] and transformed into the density and magnetic channel. The modified  $G^{\text{con}}$ , obtained in this way, is organized again in a suitable *hdf5* group structure and written to a new file called *g4iw\_conn\_sym.hdf5*, as discussed in the following and depicted in Fig. 4.10.

**Symmetrization** Since all AbinitioDFA equations have been formulated in the particle-hole density and magnetic channel, we can work in these channels right from the beginning. Thus, already in the preprocessing script I construct  $G_r^{\text{con}}$  in the density and magnetic channel  $r \in \{d, m\}$ . If SU(2) symmetry is implied, I can use Eqs. (4.9) and (4.10) to define  $G_r^{\text{con}}$  in the density and magnetic channel as

$$G_d^{\text{con}} = \frac{1}{2} \left( G_{\uparrow\uparrow\uparrow\uparrow}^{\text{con}} + G_{\downarrow\downarrow\downarrow\downarrow}^{\text{con}} + G_{\uparrow\uparrow\downarrow\downarrow}^{\text{con}} + G_{\downarrow\downarrow\uparrow\uparrow}^{\text{con}} \right), \quad (4.73)$$

$$G_m^{\text{con}} = \frac{1}{2} \left( G_{\uparrow\downarrow\downarrow\uparrow}^{\text{con}} + G_{\downarrow\uparrow\uparrow\downarrow}^{\text{con}} \right). \quad (4.74)$$

Working in the density and magnetic channel and implying SU(2) symmetry from the beginning, has the advantage that spin indices do not need to be considered any more. Instead, we are left with a channel index  $r \in \{d, m\}$  only. Thus, the quantities, that will in the following be processed in the main AbinitioDFA program, have less indices and are smaller from a storage point of view—a clear advantage considering that these quantities are in general very large. Furthermore, in Eqs. (4.73) and (4.74) we already take the SU(2) average over several components measured in CT-HYB which clearly improves the statistics of the two-particle Green's function and thus the quality of the data.

A further improvement regarding the statistics of the two-particle Green's function can be achieved by symmetrizing over equivalent orbitals. Thus, in addition to the SU(2) symmetry, the AbinitioDFA preprocessing script also considers orbital symmetries and explicitly symmetrizes  $G_r^{\text{con}}$  over equivalent orbitals, e.g. the  $t_{2g}$  orbitals in SrVO<sub>3</sub>. This orbital-symmetrization can, however, be switched off by setting *su2\_only=.true.* in the preprocessing script *vertex\_chann\_sym.f90*.

**Group structure of the file *g4iw\_conn\_sym.hdf5*** Fig. 4.10 shows the group structure of *g4iw\_conn\_sym.hdf5*, which contains the symmetrized  $G_r^{\text{con}}$  in the density and magnetic channel. The file contains separate groups with the density and the magnetic channel. Furthermore, the data is split in subgroups for each bosonic frequency (index  $i\omega$ ). This is a reasonable choice since the AbinitioDFA algorithm is parallelized over

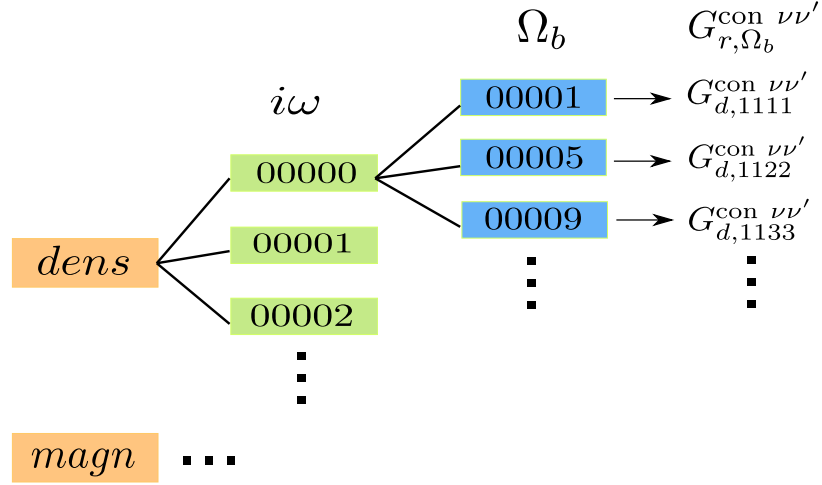


FIGURE 4.10: Group structure of the file *g4iw\_conn\_sym.hdf5*, which contains the SU(2)- and orbital-symmetrized  $G^{\text{con}}$  in the density and magnetic channel.  $i\omega$  refers to the bosonic frequency index, while  $\Omega_b$  is a combined index of the four orbital indices  $lmm'l'$ . Shown are the first few entries in the SrVO<sub>3</sub> file (three orbitals, Kanamori interaction).

the bosonic Matsubara frequency and, organized in this way, the data can be addressed quickly when reading a specific bosonic frequency slice of  $G_r^{\text{con}}$ .

Each bosonic frequency group contains subgroups with the non-zero orbital components of  $G_{r,lmm'l'}^{\text{con } \nu\nu'}$ . These orbital subgroups are labeled by the combined orbital index  $\Omega_b$ . The latter is defined through a similar index transformation as in Eq. (4.72), but involving only orbital indices. This yields

$$lmm'l' \leftrightarrow \Omega_b. \quad (4.75)$$

Thus, the four orbital indices  $lmm'l'$  are transformed into the combined index  $\Omega_b$ .

In the case of SrVO<sub>3</sub>, the number of components is reduced from 126 non-zero spin-orbital components in the original *g4iw\_conn.hdf5* file to 21 orbital components for each channel in *g4iw\_conn\_sym.hdf5*. This reduction by a factor of three is also obvious from the definition of the density and magnetic channel in Eqs. (4.73) and (4.74), where six components are mapped onto two. Clearly, the size of the *g4iw\_conn\_sym.hdf5* file is hence also significantly reduced compared to *g4iw\_conn.hdf5*.

Since the preprocessing script *vertex\_chann\_sym.f90* reads from and writes to *hdf5* files, it uses the *hdf5* library for Fortran. In order to keep the script more clear, most operations related to the *hdf5* library for Fortran have been moved to a separate module named *hdf5\_module.f90*. The latter contains e.g. subroutines named *create\_component* and *add\_to\_component*, which are then directly used in the preprocessing script.

Currently, *vertex\_chann\_sym.f90* is pre-processing only the two-particle Green's function stored in *g4iw\_conn.hdf5*.<sup>1</sup> The single-particle quantities like the local DMFT self-energy and Green's function instead are directly fed into the main AbinitioDFA program from the separate file *case.hdf5* produced by w2dynamics. Certainly, it could be a good idea to pre-process also the single-particle quantities in the existing preprocessing script. Then the latter would produce one single file, which contains all the necessary input data in the format needed by the main AbinitioDFA program. This would have the advantage that changes in the CT-HYB (w2dynamics) output would affect only the preprocessing script. If necessary, the script could even be modified to pre-process data obtained from another DMFT solver.

### 4.2.3 The main AbinitioDFA program

**Configuration** The main AbinitioDFA program is configured in the file *case.conf*. There one can specify, among others, if one wants to compute the AbinitioDFA self-energy (*eom* = *.true.*) and/or momentum-dependent DMFT susceptibilities (*susc* = *.true.*), which I will briefly introduce in the end of this section. Both quantities can be computed on a regular k-grid (default), or for specific user-defined k-points or a k-path (if *k\_list* = *.true.*, the corresponding k-path is read from the file *klist.dat*). However, before performing actual AbinitioDFA computations, it is recommended to check if the local version of the Schwinger-Dyson equation of motion reproduces the local DMFT self-energy  $\Sigma^\nu$ . This can be done by inserting only the purely local, three-leg  $\gamma^\omega$  defined in Eq. (4.63) in the equation of motion.<sup>2</sup>

Since the main AbinitioDFA program named *main.f90* has to execute many tasks, it is split into several modules. There exists a module for the computation of the equation of motion *eom\_module.f90*, and another one for computing the momentum-dependent susceptibilities *susc\_module.f90*. Furthermore, all subroutines involving one-particle Green's functions and non-interacting susceptibilities  $\chi_0$  are gathered in the module *one\_particle\_quant\_mod.f90*. Finally, there exists also a module *index\_module.f90* for the

<sup>1</sup>Since the file *g4iw\_conn.hdf5* is very large, the pre-processing script *vertex\_chann\_sym.f90* is reading the groups in the file—which correspond to the non-zero spin-orbital components of  $G^{\text{con}}$ —not all at once, but iteratively one after the other. Thus, the first group, e.g.  $G_{\uparrow\uparrow\uparrow,1111}^{\text{con } \omega\nu\nu'}$  in Fig. 4.9, is read and a routine checks if the component goes into the density or the magnetic channel according to Eqs. (4.73) and (4.74) (e.g.  $G_{\uparrow\uparrow\uparrow,1111}^{\text{con } \omega\nu\nu'}$  contributes to the density channel). Next, the "orbital-only" combined index  $\Omega_b$  is computed and the component is written into the corresponding groups in the file *g4iw\_conn\_sym.hdf5*. Then the script proceeds with the next spin-orbital component in *g4iw\_conn.hdf5*. Please note that the orbital-symmetrization implemented in *vertex\_chann\_sym.f90* is based on the same scheme and is done simultaneously.

<sup>2</sup>Currently, this check is done with a separate script, but it will eventually be included in the main AbinitioDFA program.



$\mathbf{k}$ - $\mathbf{q}$  index search needed e.g. to construct the  $\mathbf{k}$ - $\mathbf{q}$ -dependent non-interacting susceptibility of Eq. (4.77), and another module *lapack\_module.f90* for matrix inversions.<sup>3</sup> The main tasks of these modules will be discussed in detail in the following.

**Implemented equations** As the flow diagram in Fig. 4.8 clearly shows, the main AbinitioDFA program *main.f90* needs as an input the symmetrized two-particle impurity Green's function in the density and magnetic channel stored in *g4iw\_conn\_sym.hdf5*. In addition, also the Wannier Hamiltonian  $H_W^{\mathbf{k}}$  and the local DMFT one-particle Green's function  $G^\nu$ , self-energy  $\Sigma^\nu$  and chemical potential  $\mu$ , which are stored in the files *ham.hk* and *case.hdf5*, are needed. Furthermore, the local and non-local Coulomb interaction  $U$  and  $V^{\mathbf{q}}$  are read from the files *umatrix.dat* and *vmatrix.hdf5*, respectively.

$H_W^{\mathbf{k}}$  and the DMFT self-energy  $\Sigma^\nu$  and chemical potential  $\mu$  are used to compute the  $\mathbf{k}$ -dependent DMFT Green's function

$$G_{ll'}^{\mathbf{k}} = \left( i\nu + \mu - H_W^{\mathbf{k}} - \Sigma^\nu \right)_{ll'}^{-1}, \quad (4.76)$$

which in turn is used to construct the  $\mathbf{q}$ -dependent bubble  $\chi_0^{q\nu\nu}$ . The latter represents the generalized susceptibility without vertex corrections and reads

$$\chi_{0,lmml'}^{q\nu\nu} = -\beta \sum_{\mathbf{k}} G_{ll'}^{\mathbf{k}} G_{m'm}^{\mathbf{k}-\mathbf{q}}. \quad (4.77)$$

In AbinitioDFA,  $\chi_0^{q\nu\nu}$  is needed to construct the full, non-local vertex function  $F^{\mathbf{q}}$  through the non-local Bethe-Salpeter equation. Please note that in Eq. (4.77) a summation over  $\mathbf{k}$  is performed resulting in a  $\mathbf{k}$ -independent  $\chi_0^{q\nu\nu}$ . This simplification of assuming  $\chi_0^{q\nu\nu}$  to be only  $\mathbf{q}$ -dependent is possible because the  $\mathbf{k} - \mathbf{k}'$  dependence of the non-local Coulomb interaction has been neglected (see Sec. 4.1.2 and 4.1.3).

The local DMFT Green's function instead is used to construct the local bubble

$$\chi_{0,lmml}^{\omega\nu\nu} = -\beta G_{ll'}^\nu G_{m'm}^{\nu-\omega} \delta_{ll'} \delta_{mm'}. \quad (4.78)$$

Here, the local DMFT Green's functions are assumed to be orbital-diagonal  $G_{ll'}^\nu \delta_{ll'}$ . By subtracting Eq. (4.78) from Eq. (4.77), one obtains the purely non-local  $\chi_0^{nl,q\nu\nu} = \chi_0^{q\nu\nu} - \chi_0^{\omega\nu\nu}$ .

The local and non-local  $\chi_0$ 's introduced so far are important ingredients to obtain the three-leg vertices  $\gamma^{\omega\nu}$ ,  $\gamma^{q\nu}$  and  $\eta^{q\nu}$ , which have been defined in Eqs. (4.63)-(4.66) and

<sup>3</sup>The main AbinitioDFA program will eventually become even more modularized. Thus, parts of the main program, e.g. the computation of the Bethe-Salpeter equation, will be moved into modules.

are repeated here for clarity:

$$\gamma_{r,lmn'l'}^{\omega\nu} = \sum_{n'h'\nu'} \chi_{0,lmn'h'}^{\omega\nu'\nu'} F_{r,h'n'm'l'}^{\omega\nu'\nu}, \quad (4.79)$$

$$\gamma_{r,lmn'l'}^{q\nu} = \sum_{n'h'\nu'} \chi_{0,lmn'h'}^{nl,q\nu'\nu'} F_{r,h'n'm'l'}^{\omega\nu'\nu}, \quad (4.80)$$

$$\eta_{r,lmn'l'}^{q\nu} = \sum_{n'h'\nu'} \chi_{0,lmn'h'}^{q\nu'\nu'} F_{r,h'n'm'l'}^{q\nu'\nu} - \chi_{0,lmn'h'}^{\omega\nu'\nu'} F_{r,h'n'm'l'}^{\omega\nu'\nu}. \quad (4.81)$$

Please note that  $\gamma^{\omega\nu}$  is a completely local three-leg vertex which can, in principle, directly be extracted from the impurity solver. Since at the moment  $\gamma^{\omega\nu}$  is, however, not yet provided by the w2dynamics impurity solver, the current version of the AbinitioDFA program explicitly computes  $\gamma^{\omega\nu}$  from  $F^{\omega\nu'\nu}$  according to Eq. (4.79).

The computation of the three-leg vertices in Eqs. (4.79)-(4.81) clearly also involves the local DMFT vertex function  $F^{\omega\nu\nu'}$ —one of the most important ingredients to perform AbinitioDFA.  $F^{\omega\nu\nu'}$  can be obtained from the connected part of the two-particle impurity Green's function  $G^{\text{con}}$ , which is stored in the file *g4iw\_conn\_sym.hdf5*, by

$$F_{r,lmn'l'}^{\omega\nu\nu'} = [(\chi_0^\omega)^{-1}]_{lmm'l'}^{\nu\nu} G_{r,lmn'l'}^{\text{con } \omega\nu\nu'} [(\chi_0^\omega)^{-1}]_{l'm'm'l'}^{\nu'\nu'}, \quad (4.82)$$

which diagrammatically corresponds to an "amputation" of the left and the right legs of  $G^{\text{con}}$ . For the computation of the purely local  $\gamma^{\omega\nu}$  in Eq. (4.79) instead, only the right legs of  $G^{\text{con}}$  need to be "amputated", i.e.  $\gamma_{r,lmn'l'}^{\omega\nu} = \sum_{\nu'} G_{r,lmn'l'}^{\text{con } \omega\nu\nu'} [(\chi_0^\omega)^{-1}]_{l'm'm'l'}^{\nu'\nu'}$ .

Furthermore, in order to compute  $\eta^{q\nu}$  in Eq. (4.81), one needs also the q-dependent vertex function  $F^{q\nu'\nu}$  which can be obtained from the non-local Bethe-Salpeter equation. As discussed in detail in Sec. 4.1.4, one can explicitly insert the corresponding expression for  $F^{q\nu'\nu}$  in Eq. (4.81) and rewrite  $\eta^q$  in the compact form

$$\eta_r^q = (\vec{1} + \gamma_r^\omega) \left( \left[ \mathbf{1} - \chi_0^{nl,q} F_r^\omega - 2\beta^{-2} \chi_0^q V^q (\vec{1} + \gamma_r^\omega) \delta_{rd} \right]^{-1} - \mathbf{1} \right), \quad (4.83)$$

which involves only a single matrix inversion. Eq. (4.83) is actually the way how  $\eta^q$  is computed in the main AbinitioDFA program.

The three-leg vertices  $\gamma^{\omega\nu}$ ,  $\gamma^{q\nu}$  and  $\eta^{q\nu}$  can then directly be used in the equation of motion in order to obtain the AbinitioDFA self-energy. In fact, the implemented form

of the equation of motion, which has already been introduced in Eq. (4.71), reads

$$\begin{aligned}
\Sigma^{\text{D}\Gamma\text{A}} &= \Sigma^{Uloc,k} + \Sigma^{Vloc,k} + \Sigma^{ph,k} + \Sigma^{U\overline{ph}} \\
&= \Sigma_{\text{DMFT}}^\nu - \beta^{-1} \sum_{\mathbf{q}} \left( U + V^{\mathbf{q}} - \frac{\tilde{U}}{2} \right) \eta_d^{\mathbf{q}} G^{k-\mathbf{q}} + \\
&\quad + \beta^{-1} \sum_{\mathbf{q}} \frac{3}{2} \tilde{U} \eta_m^{\mathbf{q}} G^{k-\mathbf{q}} - \beta^{-1} \sum_{\mathbf{q}} \left( V^{\mathbf{q}} \gamma_d^\omega - U \gamma_d^{\mathbf{q}} \right) G^{k-\mathbf{q}}, \quad (4.84)
\end{aligned}$$

and is realized in the module *eom\_module.f90* of the main AbinitioDΓA program. In the following, I will focus on the explicit numerical implementation of the equations presented so far and discuss some operations and characteristics of the main AbinitioDΓA program in detail.

**Parallelization** The AbinitioDΓA algorithm can be parallelized over the combined bosonic index  $\mathbf{q} = (\mathbf{q}, \omega)$ , since the three-leg vertices  $\gamma^{\omega\nu}$ ,  $\gamma^{\mathbf{q}\nu}$  and  $\eta^{\mathbf{q}\nu}$  can be computed separately for each  $\mathbf{q}$ , and in the equation of motion one finally simply sums over all  $\mathbf{q}$ -contributions. Thus, the combined index  $\mathbf{q}$  is used to distribute the AbinitioDΓA algorithm over several nodes/cores with an MPI-parallelization. Each core then processes a different range of  $\mathbf{q}$ -indices and reads in only the data slices of *g4iw\_conn\_sym.hdf5* that are actually needed.<sup>4</sup>

**Compound indices** The main AbinitioDΓA program makes use of compound indices so that all equations can be implemented in the form of matrix operations. The employed compound indices are obtained by transforming the four orbital and two fermionic frequency indices of  $F_{lmm'l'}^{\omega\nu\nu'}$  into two compound indices. Thereby, the two left orbital indices  $lm$  and the left fermionic frequency index  $\nu$  are combined into one compound index  $\{ml, \nu\}$ , while the two right orbital indices  $m'l'$  and the right fermionic frequency index  $\nu'$  form the second compound index  $\{m'l', \nu'\}$ .<sup>5</sup> This way,  $F_{lmm'l'}^{\omega\nu\nu'}$  can be written in matrix form  $F_{\{m'l', \nu'\}\{ml, \nu\}}^\omega$ , as illustrated in Fig. 4.11. Please note that in the local  $F_{lmm'l'}^{\omega\nu\nu'}$  many matrix elements are zero, since the Kanamori interaction allows only for entries where two orbitals are the same. These zero matrix elements are exactly the orbital components not present in *g4iw\_conn\_sym.hdf5*. However, in order to perform straightforward matrix operations, one needs to work with the whole matrix including

<sup>4</sup>The main AbinitioDΓA program does not read  $G_{lmm'l'}^{\text{con } \omega\nu\nu'}$  all at once from the file *g4iw\_conn\_sym.hdf5*. Since  $G_{lmm'l'}^{\text{con } \omega\nu\nu'}$  is a purely local quantity which does not depend on  $\mathbf{q}$  but only on  $\omega$ , a corresponding slice of  $G_{lmm'l'}^{\text{con } \omega\nu\nu'}$  needs to be read only when the bosonic Matsubara frequency  $\omega$  in the loop over the combined index  $\mathbf{q} = (\mathbf{q}, \omega)$  changes.

<sup>5</sup>Please note that the bosonic frequency  $\omega$  does not enter the compound index; the AbinitioDΓA program is parallelized over the "external" index  $\mathbf{q} = (\mathbf{q}, \omega)$ .

$$F_{ml'l'm'}^{\nu\nu'} = \begin{matrix} & \{m'l', \nu'\} \\ & 11, \nu'_1 & 12, \nu'_1 & 21, \nu'_1 & 22, \nu'_1 & 11, \nu'_2 & 12, \nu'_2 & 21, \nu'_2 & 22, \nu'_2 & \dots \\ \{ml, \nu\} & 11, \nu_1 & F_{1111}^{\nu_1\nu'_1} & F_{1112}^{\nu_1\nu'_1} & F_{1121}^{\nu_1\nu'_1} & F_{1122}^{\nu_1\nu'_1} & & & & \\ & 12, \nu_1 & F_{2111}^{\nu_1\nu'_1} & F_{2112}^{\nu_1\nu'_1} & F_{2121}^{\nu_1\nu'_1} & F_{2122}^{\nu_1\nu'_1} & & & & \\ & 21, \nu_1 & F_{1211}^{\nu_1\nu'_1} & F_{1212}^{\nu_1\nu'_1} & F_{1221}^{\nu_1\nu'_1} & F_{1222}^{\nu_1\nu'_1} & \blacksquare & \blacksquare & \blacksquare & \\ & 22, \nu_1 & F_{2211}^{\nu_1\nu'_1} & F_{2212}^{\nu_1\nu'_1} & F_{2221}^{\nu_1\nu'_1} & F_{2222}^{\nu_1\nu'_1} & & & & \\ & 11, \nu_2 & & & & F_{1111}^{\nu_2\nu'_2} & & & & \\ & 12, \nu_2 & & & & & \blacklozenge & \blacklozenge & \blacklozenge & \\ & 21, \nu_2 & & \blacksquare & & & & & & \\ & 22, \nu_2 & & \blacksquare & & & & & & \\ & \vdots & & & & & & & & \end{matrix}$$

FIGURE 4.11: By using compound indices  $\{ml, \nu\}$  and  $\{m'l', \nu'\}$ ,  $F_{lmm'l'}^{\omega\nu\nu'}$  can be written in matrix form (in the graphics, the "external" bosonic frequency  $\omega$  has been omitted for simplicity). Explicitly shown is the first orbital block ( $\nu = \nu_1, \nu' = \nu'_1$ ) in the case of two orbitals. Please note that many entries are zero if density or Kanamori interactions are employed, e.g.  $F_{1112}^{\nu_1\nu'_1} = 0$  and  $F_{1121}^{\nu_1\nu'_1} = 0$ .

$$\chi_{0,lmm'l'}^{\nu\nu'} = \begin{matrix} & \{m'l', \nu'\} \\ & 11, \nu'_1 & 12, \nu'_1 & 21, \nu'_1 & 22, \nu'_1 & 11, \nu'_2 & 12, \nu'_2 & 21, \nu'_2 & 22, \nu'_2 & \dots \\ \{ml, \nu\} & 11, \nu_1 & \chi_{0,1111}^{\nu_1\nu'_1} & \chi_{0,1112}^{\nu_1\nu'_1} & \chi_{0,1121}^{\nu_1\nu'_1} & \chi_{0,1122}^{\nu_1\nu'_1} & & & & \\ & 12, \nu_1 & \chi_{0,2111}^{\nu_1\nu'_1} & \chi_{0,2112}^{\nu_1\nu'_1} & \chi_{0,2121}^{\nu_1\nu'_1} & \chi_{0,2122}^{\nu_1\nu'_1} & & & & \\ & 21, \nu_1 & \chi_{0,1211}^{\nu_1\nu'_1} & \chi_{0,1212}^{\nu_1\nu'_1} & \chi_{0,1221}^{\nu_1\nu'_1} & \chi_{0,1222}^{\nu_1\nu'_1} & & & & \\ & 22, \nu_1 & \chi_{0,2211}^{\nu_1\nu'_1} & \chi_{0,2212}^{\nu_1\nu'_1} & \chi_{0,2221}^{\nu_1\nu'_1} & \chi_{0,2222}^{\nu_1\nu'_1} & & & & \\ & 11, \nu_2 & & & & \chi_{0,1111}^{\nu_2\nu'_2} & \chi_{0,1112}^{\nu_2\nu'_2} & \chi_{0,1121}^{\nu_2\nu'_2} & \chi_{0,1122}^{\nu_2\nu'_2} & \\ & 12, \nu_2 & & & & \chi_{0,2111}^{\nu_2\nu'_2} & \chi_{0,2112}^{\nu_2\nu'_2} & \chi_{0,2121}^{\nu_2\nu'_2} & \chi_{0,2122}^{\nu_2\nu'_2} & \\ & 21, \nu_2 & & & & \chi_{0,1211}^{\nu_2\nu'_2} & \chi_{0,1212}^{\nu_2\nu'_2} & \chi_{0,1221}^{\nu_2\nu'_2} & \chi_{0,1222}^{\nu_2\nu'_2} & \\ & 22, \nu_2 & & & & \chi_{0,2211}^{\nu_2\nu'_2} & \chi_{0,2212}^{\nu_2\nu'_2} & \chi_{0,2221}^{\nu_2\nu'_2} & \chi_{0,2222}^{\nu_2\nu'_2} & \\ & \vdots & & & & & & & & \ddots \end{matrix}$$

FIGURE 4.12: Matrix structure of the bubble terms  $\chi_{0,lmm'l'}^{nl,q\nu\nu'}$ ,  $\chi_{0,lmm'l'}^{q\nu\nu'}$  and  $\chi_{0,lmm'l'}^{\omega\nu\nu'}$  (in the graphics, the "external" bosonic index  $q = (\mathbf{q}, \omega)$  has been omitted). Shown are the first two "orbital blocks" (in orange). The block-diagonal structure arises from the fact that the bubble terms are diagonal with respect to the fermionic frequency  $\delta_{\nu\nu'}$ . The local  $\chi_{0,lmm'l'}^{\omega\nu\nu'}$  of Eq. (4.78) has an even simpler, completely diagonal structure (dark orange matrix elements only). Here, the full structure is only shown for clarity, the main AbinitioDGA program stores and works only with the non-zero orbital blocks.

all zero elements. On the other hand, this has the advantage that the implementation of the main AbinitioDΓA program is not restricted to density or Kanamori kind of interactions.

By using the compound indices  $\{ml, \nu\}$  and  $\{m'l', \nu'\}$ , also the time reversal symmetry of the local  $F$  can be implemented easily. In fact, the time reversal symmetry

$$F_{lmm'l'}^{\omega\nu\nu'} = F_{l'm'ml}^{\omega\nu'\nu}, \quad (4.85)$$

which corresponds to an exchange of the incoming and outgoing particles, reduces to a transpose in the compound matrix

$$F_{\{ml, \nu\}\{m'l', \nu'\}}^{\omega} = F_{\{m'l', \nu'\}\{ml, \nu\}}^{\omega}. \quad (4.86)$$

Similar to the local, full vertex function  $F^{\omega\nu\nu'}$ , also the bubble terms  $\chi_0^{nl, q\nu\nu}$ ,  $\chi_0^{q\nu\nu}$  and  $\chi_0^{\omega\nu\nu}$  can be written in matrix form with respect to the compound indices  $\{ml, \nu\}$  and  $\{m'l', \nu'\}$ , as visualized in Fig. 4.12. Since the bubble terms are diagonal with respect to the fermionic frequency indices  $\chi_0^{\nu\nu} = \chi_0^{\nu'\nu'} \delta_{\nu\nu'}$ , they have a block-diagonal structure with all frequency off-diagonal ( $\nu \neq \nu'$ ) matrix elements being zero. This block-diagonal structure applies to  $\chi_0^{nl, q\nu\nu}$ ,  $\chi_0^{q\nu\nu}$  and  $\chi_0^{\omega\nu\nu}$ . However, the purely local  $\chi_0^{\omega\nu\nu}$  of Eq. (4.78) is even fully diagonal (containing only the dark orange elements in Fig. 4.12), since the local DMFT Green's functions are assumed to be orbital-diagonal. This diagonal structure of  $\chi_0^{\omega\nu\nu}$  is used in Eq. (4.82) for "amputating" the legs of the local  $G^{\text{con}, \omega\nu\nu'}$  in order to obtain  $F^{\omega\nu\nu'}$ .

**Computation of the three-leg vertices** The computation of the three-leg vertices  $\gamma^q$  and  $\eta^q$  in Eqs. (4.80) and (4.83) involves a multiplication of  $\chi_0^{nl, q}$  with  $F^{\omega}$ . This matrix multiplication can be simplified by exploiting the block-diagonal structure of  $\chi_0^{nl, q}$ . In fact, by multiplying each orbital block of  $\chi_0^{nl, q}$  with the corresponding horizontal slice of  $F^{\omega}$ , as shown in Fig. 4.13, one can avoid a large and time-consuming matrix multiplication with a lot of zero entries.

The matrix inversion in the equation for  $\eta^q$  (4.83) instead cannot be simplified or split into smaller subroutines. Here, the full matrix dimension is needed. In fact, from a numerical point of view, this matrix inversion is the most demanding operation of the main AbinitioDΓA program.

The calculation of the three-leg vertices in Eqs. (4.79)-(4.83) furthermore requires a sum over the left fermionic frequency. In fact, the summation over the left fermionic frequency makes them, diagrammatically, *three-leg* vertices. In terms of compound matrices, this

$$\begin{matrix} & \nu'_1 & \nu'_2 & \dots \\ \nu_1 & \text{orange block} & & \\ \nu_2 & \text{red block} & & \\ \vdots & & & \end{matrix} = \begin{matrix} & \nu''_1 & \nu''_2 & \dots \\ \nu_1 & \text{orange block} & & \\ \nu_2 & & \text{red block} & \\ \vdots & & & \ddots \end{matrix} \times \begin{matrix} & \nu'_1 & \nu'_2 & \dots \\ \nu''_1 & \text{orange block} & & \\ \nu''_2 & \text{red block} & & \\ \vdots & & & \end{matrix}$$

FIGURE 4.13: The matrix multiplication of the block-diagonal  $\chi_{0,lmm'l'}^{nl,q\nu\nu'}$  with the full  $F_{r,lmm'l'}^{\omega\nu\nu'}$  in Eqs. (4.80) and (4.83) can be split into several smaller operations. By multiplying each orbital block of  $\chi_{0,lmm'l'}^{nl,q\nu\nu'}$  with the corresponding slice of  $F_{r,lmm'l'}^{\omega\nu\nu'}$  (marked with the same color), one can avoid multiplying a lot of zero entries with each other.

sum over the left fermionic frequency is visualized in Fig. 4.14. Through the sum, the left compound index is reduced to an orbital compound index  $\{lm\}$  and the resulting matrix is not quadratic any more. Please note that this summation over the left fermionic frequency needs to be performed explicitly only in order to obtain  $\gamma^q$  and  $\gamma^\omega$ .<sup>6</sup> The three-leg structure of  $\eta^q$  is actually obtained in a different way, i.e. by multiplying with  $(\vec{1} + \gamma^\omega)$  from the left, as can be seen in Eq. (4.83).

**Equation of motion** Once the three-leg vertices  $\gamma_r^\omega$ ,  $\gamma_r^q$  and  $\eta_r^q$  are obtained, they can directly be used in the expression for the Schwinger-Dyson equation of motion (4.84). There, the multiplication of the three-leg vertices with the corresponding local and non-local Coulomb interaction terms ( $U$ ,  $\tilde{U}$  and  $\mathbf{V}^q$ ) is done in the basis of compound indices. Thus, the four-index  $U_{lmm'l'}$  and  $V_{lmm'l'}^q$ , which are obtained through constrained random phase approximation (cRPA) [32] and stored in the files *umatrix.dat* and *vmatrix.hdf5*, first need to be transformed to compound indices  $\{ml\}$  and  $\{m'l'\}$ .<sup>7</sup> Then, the multiplication of  $V^q$  and  $U$  times the three-leg  $\gamma$ 's and  $\eta$  in the Schwinger-Dyson equation of motion (4.84) can easily be performed, as schematically depicted in Fig. 4.15.

The final convolution with the non-local Green's function  $G^{k-q}$  in the equation of motion (4.84) is more straightforward to perform by breaking up the compound indices in single orbital and frequency indices again. This way, the different contributions in the equation of motion can be computed easily. The sum over the bosonic compound index  $q = (\mathbf{q}, \omega)$ , on the other hand, is performed by summing up all  $q$ -contributions

<sup>6</sup>Eventually, the purely local three-leg vertex  $\gamma^\omega$  will be directly computed in CT-HYB (see Ref. [116]), which will make the current sum over the left fermionic frequency to obtain  $\gamma^\omega$  redundant.

<sup>7</sup>Currently, all components of the local four-index  $U$  are simply stored in the file *umatrix.dat* in the format *i j k l u\_value*. The non-local Coulomb interaction  $V^q$  instead is stored in an *hdf5*-file making use of a similar group structure which has already been employed for the local  $G^{\text{con}}$ . Thus, *vmatrix.hdf5* contains only the non-zero components of  $V^q$ . Eventually, local and non-local Coulomb interaction will be joined in one single *hdf5* file.

$$\gamma^\omega, \gamma^q, \eta^q = \{ml\} \left( \begin{array}{c} \nu_1 \\ \nu_2 \\ \nu_3 \\ \vdots \end{array} \begin{array}{c} \nu'_1 \\ \nu'_1 \\ \nu'_1 \\ \vdots \end{array} \begin{array}{c} \nu'_2 \\ \nu'_2 \\ \nu'_2 \\ \vdots \end{array} \begin{array}{c} \dots \\ \dots \\ \dots \\ \vdots \end{array} \right)$$

FIGURE 4.14: Schematic representation of the sum over the left fermionic frequency needed to obtain the three-leg vertices  $\gamma^\omega$ ,  $\gamma^q$  and  $\eta^q$  in Eqs. (4.79)-(4.83). By summing over all stacked slices (different colors symbolize different left fermionic frequencies  $\nu_i$ ), the first dimension of the matrix is reduced to the orbital-only compound index  $\{lm\}$ .

within the parallel loop over  $q$ . Finally, the contributions computed on different cores are summed up by using an MPI\_gather. As discussed in Sec. 3.2.4, the AbinitioDFA self-energies  $\Sigma_{DFA}^k$ , which are Ladder-DFA self-energies, need to be  $\lambda$ -corrected. However, in  $\text{SrVO}_3$ —the material studied here—, the  $\lambda$ -correction turned out to be negligible. Thus, at the moment there does not exist any standardized implementation of the AbinitioDFA  $\lambda$ -corrections yet.

**k-point symmetries and high-frequency asymptotics** Currently, the  $\mathbf{k}$ -dependent AbinitioDFA self-energy  $\Sigma_{DFA}^k$  is, by default, computed on a regular  $\mathbf{k}$ -grid within the first Brillouin zone of the corresponding material. In fact, the AbinitioDFA algorithm uses the  $\mathbf{k}$ -grid of the wien2wannier Hamiltonian, which is a regular grid within the reducible Brillouin zone. However, this default  $\mathbf{k}$ -grid for the computation and output of the AbinitioDFA self-energy can be substituted with a user-defined  $\mathbf{k}$ -list or  $\mathbf{k}$ -path (set *k\_list* = *true*. in the file *case.conf*). Of course, it would also be desirable to restrict the computation of  $\Sigma_{DFA}^k$  to the irreducible Brillouin zone. Especially, restricting the  $\mathbf{q}$ -grid of the parallel  $q$ -loop to the irreducible Brillouin zone would save a lot of computational time. In general, this could be done through an interface with a DFT-code like Wien2k, which includes already elaborate routines to deal with crystal symmetries. So far, there exists only the option to choose a more coarse  $\mathbf{q}$ -grid. By setting e.g. *q\_frac* = 2 in the *case.conf* file, the distance between neighbouring  $\mathbf{q}$ -points is doubled compared to the original  $\mathbf{k}$ -grid of the wien2wannier Hamiltonian. However, this option is rather for a speedup of test runs, since it does not respect any crystal symmetries for the reduction of the  $\mathbf{k}$ -grid.

In *case.conf* one can also specify to run a computation with fewer bosonic or fermionic frequencies. By setting *small\_freq\_box* = *true*. and explicitly entering the desired number of bosonic and fermionic Matsubara frequencies, the default frequency boxes, which are taken over from the  $G^{\text{con}}$  measured in CT-QMC, are cut to the specified size. With this option one can check the convergence of the AbinitioDFA results with respect to the

$$\left( \begin{matrix} \{m''l''\} \\ U, V^{\mathbf{q}} \end{matrix} \right) \times \left( \begin{matrix} \{m'l', \nu'\} \\ \gamma^{\omega}, \gamma^q, \eta^q \end{matrix} \right)$$

FIGURE 4.15: Schematic representation of the matrix multiplication between the interaction matrices  $U$  and  $V^{\mathbf{q}}$  and the three-leg vertices  $\gamma_r^{\omega}$ ,  $\gamma_r^q$  and  $\eta_r^q$ . This operation is part of the Schwinger-Dyson equation of motion (4.84).

size of the used frequency boxes. By performing several computations with increasing size of the bosonic and fermionic frequency boxes, one can extrapolate the value of the AbinitioDFA self-energy  $\Sigma_{D\Gamma A}^k$  and avoid uncertainties related to the finite size of the considered frequency boxes. However, this extrapolation procedure is numerically expensive since it requires running the AbinitioDFA program multiple times (once for each frequency box size). Furthermore, the quality of the CT-QMC data for  $G^{\text{con}}$  needs to be very high in order to obtain a monotonous and smooth behavior for the extrapolation. Hence, currently I simply work with the maximally affordable box size and check the convergence of  $\Sigma_{D\Gamma A}^k$  by further performing some computations with smaller box sizes.

Recently, vertex asymptotics have been implemented within w2dynamics [116]. Thus, the high-frequency asymptotics of the local, full vertex function  $F^{\omega\nu\nu'}$  are directly computed within CT-QMC by considering all asymptotically contributing diagrams. This reduces statistical uncertainties of the local vertex and allows for very large frequency box sizes. These improvements regarding the local vertex are really important for the main AbinitioDFA program. However, because of numerical limitations, the latter cannot deal with arbitrary big frequency boxes, and thus the final extrapolation of  $\Sigma_{D\Gamma A}^k$  with respect to the frequency box size still needs to be done.

**Momentum-dependent susceptibilities** With the main AbinitioDFA program one can also compute momentum-dependent, physical susceptibilities. This option (*susc*) can be specified in the *case.conf* file. Then, the AbinitioDFA program is executed in the usual way until the computation of the three-leg vertices. But instead of continuing with the equation of motion, the q-dependent DMFT susceptibilities can be obtained as

$$\chi_{r,lm m'l'}^{\mathbf{q}} = \sum_{\substack{nn'hh' \\ \nu'\nu}} \chi_{0,lm hn}^{\mathbf{q}\nu'\nu'} F_{r,nhh'n'}^{\mathbf{q}\nu'\nu} \chi_{0,n'h'm'l'}^{\mathbf{q}\nu\nu}. \quad (4.87)$$



These are the dynamic and  $\mathbf{q}$ -dependent DMFT susceptibilities in the density and magnetic channel  $r \in \{d, m\}$  (the compound index  $q$  contains  $\mathbf{q}$  and the bosonic frequency  $\omega$ ). The magnetic susceptibility in form of a spin-spin correlation function can then be obtained from Eq. (4.87) by summing over the corresponding orbital combinations  $\chi_m^q = \sum_{ll'} \chi_{m, ll' l' l}^q$ . The local magnetic susceptibility, which has been computed for FeAl in Sec. 2.4, can be obtained by replacing the compound index  $q = (\mathbf{q}, \omega)$  in Eq. (4.87) with the bosonic frequency index  $\omega$  only, i.e.  $\chi_m^q \rightarrow \chi_m^\omega$ .

#### 4.2.4 Numerical effort

The numerical effort for calculating the local vertex in CT-HYB scales roughly as  $\beta^5(\#o)^4$  with a large prefactor because of the Monte-Carlo sampling ( $\#o$  is the number of orbitals; there is also an exponential scaling in  $\#o$  for calculating the local trace but only with a  $\beta^1$  prefactor so that this term is less relevant for typical  $\#o$  and  $\beta$ ). The  $\beta^5(\#o)^4$  scaling can be understood from the fact that an update of the hybridization matrix is  $\sim \beta^2$  (the mean expansion order is  $\sim \beta$ ), and we need to determine  $(\beta)^3(\#o)^4$  different vertex contributions if the number of measurements per imaginary time interval stays constant. However, since we eventually calculate the self energy which depends on only one frequency and two orbitals, a much higher noise level can be permitted for larger  $\#\omega$  and  $\#o$ . That is, in practice a weaker scaling on  $\#\omega$  and  $\#o$  is possible. Outside a window of lowest frequencies, one can also employ the asymptotic form [105, 116, 117] of the vertex which depends on only two frequencies so that its calculation scales as  $\beta^4(\#o)^4$ . Without using these shortcuts, calculating the vertex for SrVO<sub>3</sub> with  $\#o = 3$ ,  $\#\omega = 120$  and  $\beta = 10 \text{ eV}^{-1}$  took 150000 core h (Intel Xeon E5-2650v2, 2.6 GHz, 16 cores per node).

As discussed already, the main AbinitioDΓA program is parallelized over the compound index  $q = (\omega, \mathbf{q})$ . Obviously, this  $q$ -loop scales with the number of  $\mathbf{q}$ -points  $\#q$  and the number of (bosonic) Matsubara frequencies  $\#\omega$  (which is roughly  $\sim \beta$ ), and thus as  $\#\omega\#q$ . Within this parallel loop, the numerically most demanding task is the matrix inversion in Eq. (4.83). Since the dimension of the matrix that needs to be inverted is given by  $\#\omega(\#o)^2$ , the inversion scales  $\sim (\#\omega\#o^2)^3$ . Altogether this part hence scales as  $\#q\#\omega^4\#o^6$ . (The numerical effort for calculating the self energy via the equation of motion (4.84) is  $\sim \#q^2\#\omega^2\#o^6$  and becomes the leading contribution at high temperatures and a large number of  $\mathbf{q}$ -points.) For the AbinitioDΓA computation of SrVO<sub>3</sub> with  $\#o = 3$  and  $\#q = 20^3$ , the numerical effort with respect to the number of Matsubara frequencies  $\#\omega$  has explicitly been tested by performing computations with three different frequency box sizes:  $\#\omega = 120$ ,  $\#\omega = 240$  and  $\#\omega = 400$ . Fig. 4.16 shows the respective numerical effort in core h. From Fig. 4.16 it can be seen that the main

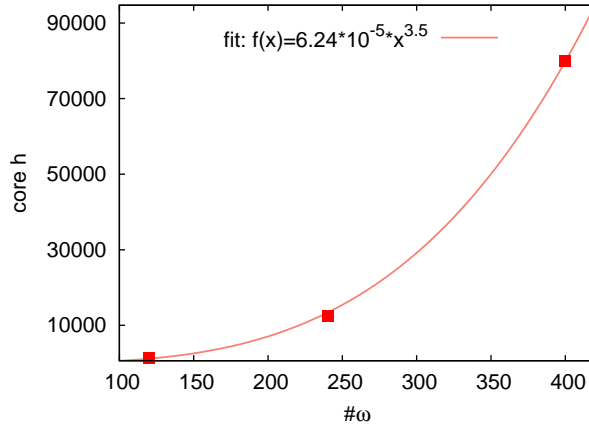


FIGURE 4.16: Computational effort of the AbinitioDΓA program with respect to the number of involved Matsubara frequencies  $\#\omega$ .

AbinitioDΓA program scales with  $(\#\omega)^{3.5}$ , which is indeed slightly better than the expected  $\#\omega^4$  behavior. This is most likely due to the fact that the used linear-algebra routines for matrix inversions scale better than  $(\#\omega\#o^2)^{3.8}$ .

### 4.3 Test cases

In order to assess the numerical stability and convergence of the newly developed AbinitioDΓA program, several test cases have been considered. Since the AbinitioDΓA is a genuinely new method, there do not exist many other results to compare with. However, there exists already a DΓA program for the one-band case, which has e.g. been used to obtain the results in Refs. [9, 98, 99]. Thus, I benchmarked the newly developed AbinitioDΓA program to this already existing DΓA program. For the multi-band case instead, we rely on tests performed in the atomic limit, where the results are known exactly. The results of these test cases are summarized in the following.

#### 4.3.1 One-band Hubbard model

The one-band Hubbard model was chosen as a first test case to benchmark the AbinitioDΓA program. I considered the one-band 2d Hubbard model at half-filling  $n = 0.5$  and an inverse temperature of  $\beta = 8$  (all quantities in units of the bandwidth). The Hubbard interaction was set to  $U = 1$  and a total number of  $N_k = N_q = 10 \times 10$  k-points in the reducible 2d Brillouin zone and  $\#\omega = 80$  bosonic and fermionic frequencies were used in the computation.

<sup>8</sup>The matrix inversion in Eq. (4.83) is performed by using the *lapack*-routines *zgetrf* and *zgetri*, which compute the inverse of a matrix by triangular decomposition.

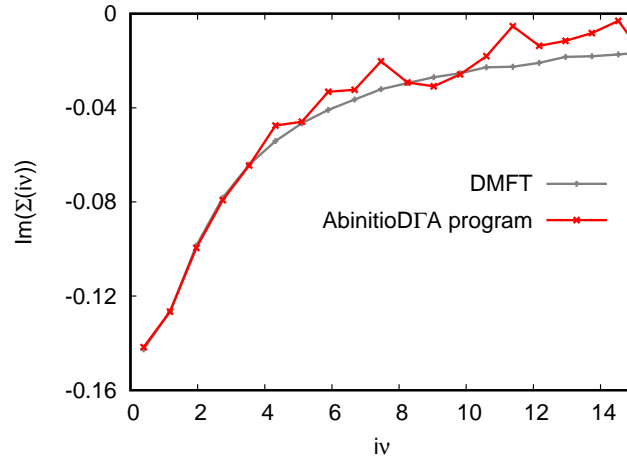


FIGURE 4.17: Local self-energy for the one-band 2d Hubbard model at half-filling  $n = 0.5$  and inverse temperature  $\beta = 8$  ( $\#\omega = 80$ ). The local self-energy obtained from the AbinitioD $\Gamma$ A program (in red) coincides with the original DMFT self-energy (in grey) up to statistical fluctuations.

Fig. 4.17 shows the result of the first check that has been performed for this system. Here, all  $\mathbf{k}$ - and  $\mathbf{q}$ -dependent propagators  $G^{\mathbf{k}}$  and  $G^{\mathbf{k}-\mathbf{q}}$  have been replaced with their local counterpart  $G^{\nu}$  and  $G^{\nu-\omega}$ . This way, the AbinitioD $\Gamma$ A program corresponds to a local equation of motion and thus reproduces the local DMFT self-energy. Indeed, Fig. 4.17 shows that the local self-energy obtained this way coincides with the original DMFT self-energy up to statistical fluctuations stemming from the CT-QMC error, which is larger for the local two-particle vertex employed in AbinitioD $\Gamma$ A.

After this first check, I computed the  $\mathbf{k}$ -dependent AbinitioD $\Gamma$ A self-energies and compared them to the results obtained from the one-band D $\Gamma$ A program. Fig. 4.18 shows the comparison of the self-energies for three different  $\mathbf{k}$ -points. In order to exclude uncertainties related to the statistical noise of the CT-QMC input data, I also run the AbinitioD $\Gamma$ A program with exactly the same exact-diagonalization (ED) input data which was used in the one-band D $\Gamma$ A program. Indeed, Fig. 4.18 shows that this way the self-energies obtained from the D $\Gamma$ A and the AbinitioD $\Gamma$ A program are lying on top of each other.

The results presented so far were at half-filling, where additional symmetries apply which are in general not present away from half-filling. In order to make sure the AbinitioD $\Gamma$ A program works correctly at all fillings, the 2d Hubbard model at a filling of  $n = 0.57$  has been considered. Fig. 4.19 shows that also out of half-filling the local DMFT self-energy is reproduced correctly by the AbinitioD $\Gamma$ A program. The visible fluctuations in the local self-energy obtained from the AbinitioD $\Gamma$ A program (red lines in Fig. 4.19) are due to poor statistics of the CT-QMC data and the small frequency boxes of  $\#\omega = 60$  employed in this test run. However, one can observe a small deviation in the real part of

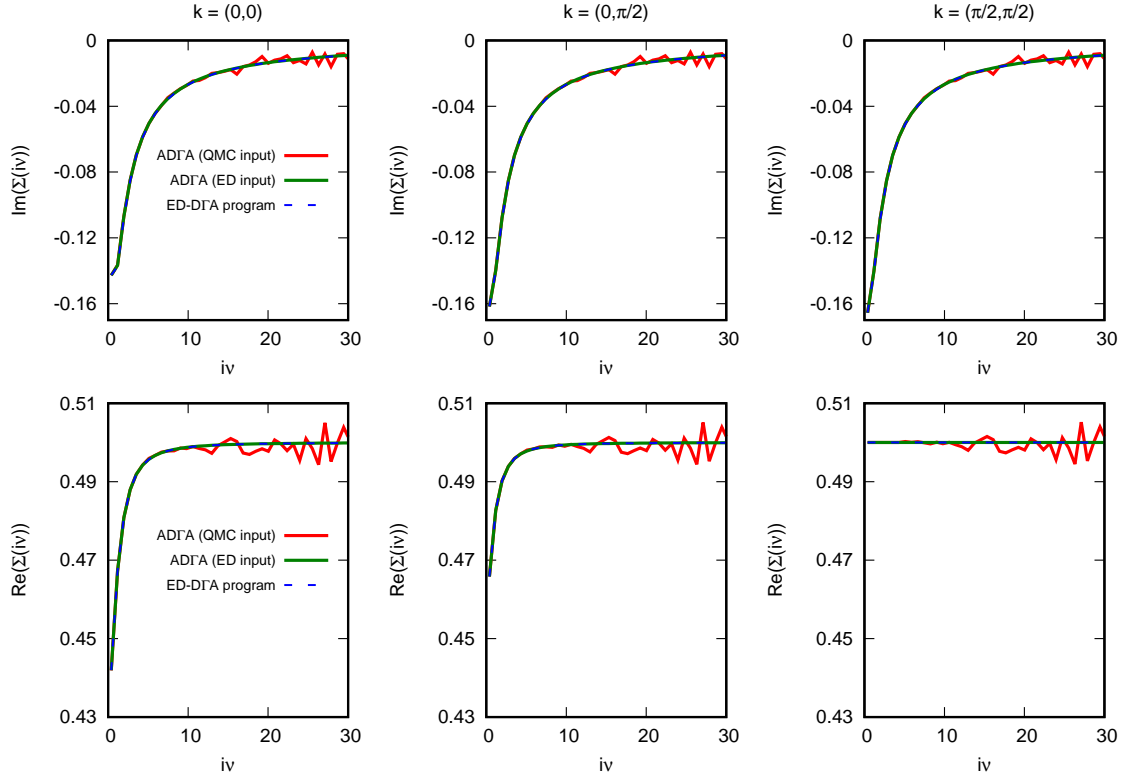


FIGURE 4.18: (Abinitio)DΓA self-energies of the 2d Hubbard model (half-filling,  $\beta = 8$ ,  $\#\omega = 80$ ) for three different  $\mathbf{k}$ -points: (red) AbinitioDΓA program with CT-QMC input data, (blue) AbinitioDΓA program with ED input data, (green) DΓA program with ED input data. Up to statistical fluctuations (in particular at large frequencies  $iv$ ) stemming from the CT-QMC input data, all self-energies are lying on top of each other.

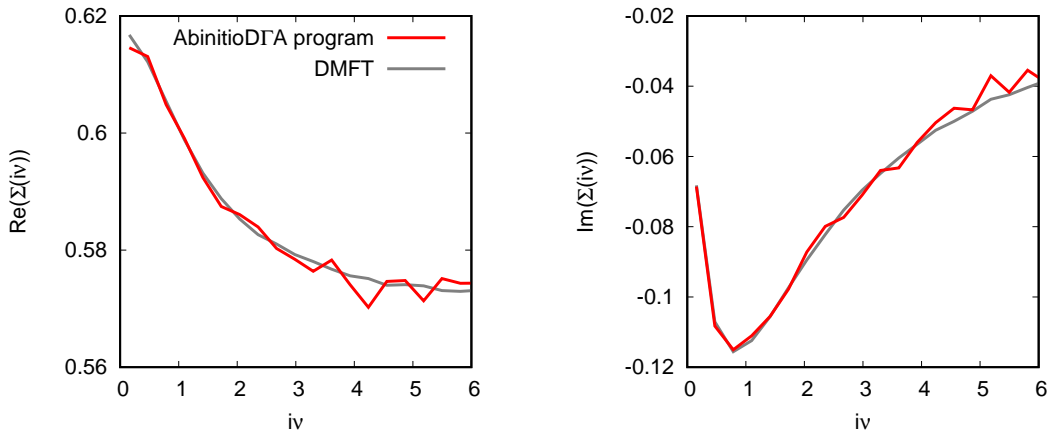


FIGURE 4.19: 2d Hubbard model out of half-filling ( $n = 0.57$ ) for  $U = 1$  and  $\beta = 20$ : Comparison between (in red) the local self-energy obtained from the AbinitioDΓA program (with  $\#\omega = 60$ ) and (in grey) the original DMFT self-energy .

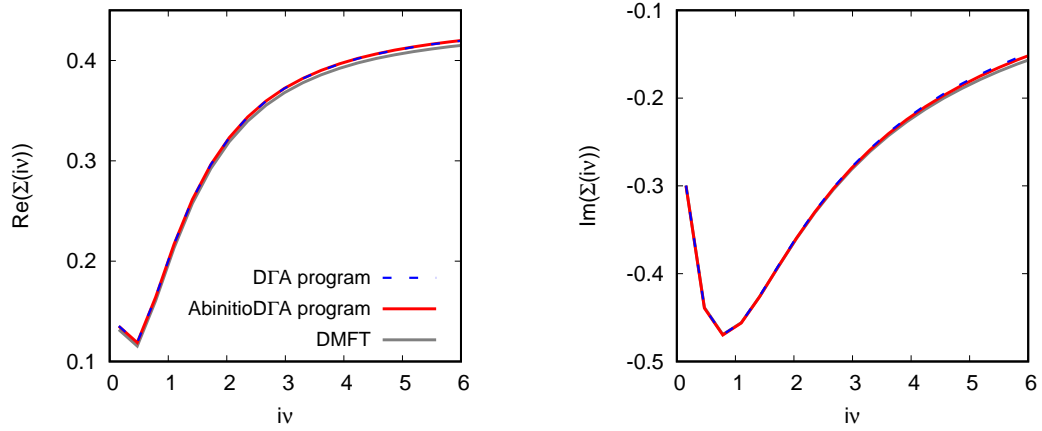


FIGURE 4.20: 3d Hubbard model out of half-filling ( $n = 0.43$ ) for  $U = 1$ ,  $\beta = 20$  and  $\#\omega = 80$ : When the D $\Gamma$ A and the AbinitioD $\Gamma$ A program are provided with the same ED data, they yield exactly the same local self-energy which coincides with the DMFT self-energy.

the self-energy even at the first fermionic Matsubara frequencies (visible in the left panel of Fig. 4.19). Thus, in order to make sure that there is no error in the AbinitioD $\Gamma$ A program, I compared with out of half-filling results obtained from the existing one-band D $\Gamma$ A program. Since there were no D $\Gamma$ A results available for the same test case (2d Hubbard model,  $n = 0.57$ ), Fig. 4.20 shows results for the 3d Hubbard model at  $n = 0.43$ . There, it can clearly be seen that the one-band D $\Gamma$ A and the AbinitioD $\Gamma$ A program yield exactly the same result for the local self-energy which agrees very well with the original DMFT self-energy.<sup>9</sup>

### 4.3.2 Two-band atomic limit

Since the present AbinitioD $\Gamma$ A program is the first implementation of D $\Gamma$ A for multi-orbital systems, the options to actually test the multi-orbital features are very limited. Of course, in any case one can and should always check that the local version of the AbinitioD $\Gamma$ A program correctly reproduces the local DMFT self-energy. In particular, in the multi-orbital case one should make sure that the local version of the AbinitioD $\Gamma$ A program yields the same local self-energy for all degenerate orbitals.

For further checks, we here rely on computations in the atomic limit, where no hybridization of the impurity with the bath exists. In this simplified limit, the self-energy and the two-particle Green's function can be calculated analytically. Thus, one can provide

<sup>9</sup>For the test cases out of half-filling presented in Figs. 4.19 and 4.20, no actual D $\Gamma$ A self-energies have been computed. The agreement of the AbinitioD $\Gamma$ A with the D $\Gamma$ A program in the cases presented so far has been regarded to be sufficient to indicate that the AbinitioD $\Gamma$ A program is working correctly for the one-band case.

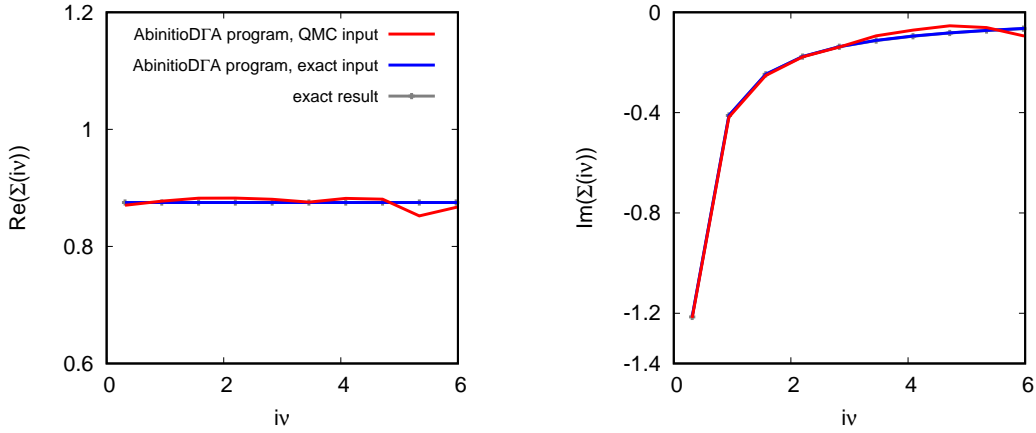


FIGURE 4.21: Two-band atomic limit at half-filling ( $n = 0.5$ ) and interaction parameters  $U = 1.0$ ,  $J = 0.25$  and  $U' = 0.5$ . The exact solution (in grey, background) is reproduced correctly by the AbinitioDΓA program with exact input data (in blue) as well as QMC input data (in red). (here  $\#\omega = 80$ )

the AbinitioDΓA program with the exact two-particle Green's function of the atomic limit and make sure that the resulting self-energy corresponds to the exact solution. Fig. 4.21 indeed shows that the exact self-energy in the two-band degenerate atomic limit at half-filling is correctly reproduced by the AbinitioDΓA program. In fact, when the program is provided with the exact two-particle Green's function, the resulting self-energy perfectly agrees with its exact counterpart. In addition, also the atomic limit two-particle Green's function obtained through CT-QMC yields the correct self-energy up to statistical fluctuations.<sup>10</sup>

Furthermore, I also investigated the two-band atomic limit for a filling of  $n = 0.3$ . Fig. 4.22 shows that in this case the AbinitioDΓA algorithm yields a self-energy which slightly deviates from the exact solution. Especially the real part of the self-energy in the left panel of Fig. 4.22 shows a notable offset compared to the exact solution. This deviation is most likely an artefact of the finite size (here  $\#\omega = 80$ ) of the employed fermionic and bosonic frequency boxes. In fact, I checked the convergence of the self-energy with respect to the employed frequency boxes and found that by increasing  $\#\omega$  the self-energy converges towards its exact solution (see Fig. 4.23). This suggests that the limitations due to finite frequency box sizes within the AbinitioDΓA program can be overcome by a final extrapolation of the AbinitioDΓA self-energy.

<sup>10</sup>Please note that the self-energy shown in Fig. 4.21 applies to both orbitals since they are degenerate.

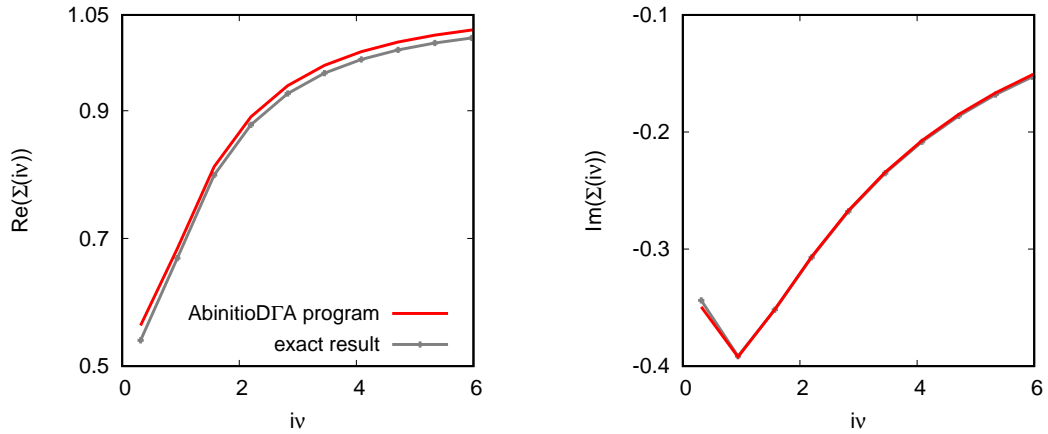


FIGURE 4.22: Two-band atomic limit away from half-filling ( $n = 0.3$ ) and for the interaction parameters  $U = 2.0$ ,  $J = 0.5$  and  $U' = 1.0$ . Especially the real part of the self-energy (left panel) shows a notable offset compared to the exact solution (in grey). (employed frequency box:  $\#\omega = 80$ )

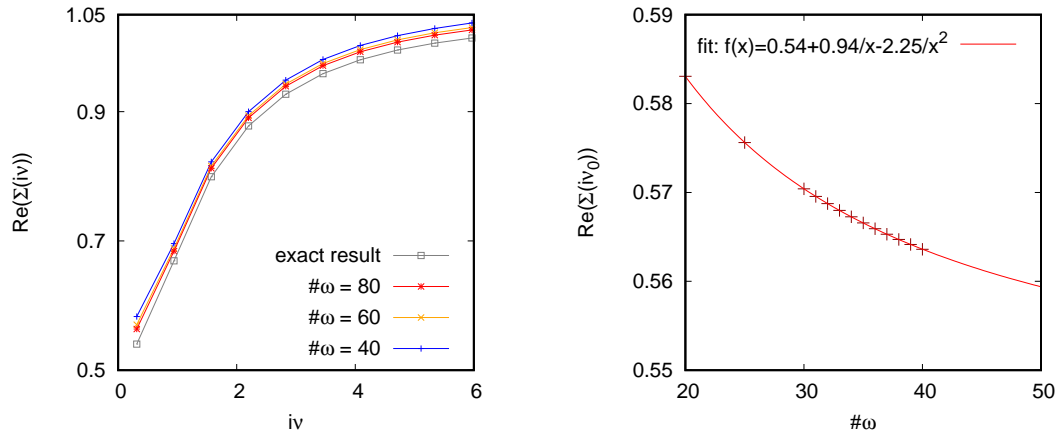


FIGURE 4.23: Convergence of the real part of the self-energy  $\Re(\Sigma(iv))$  with respect to the size  $\#\omega$  of the frequency box used in the computation (two-band atomic limit,  $n = 0.3$ ). By increasing  $\#\omega$ , the self-energy converges towards its exact solution. In the right panel the value of the self-energy at the first Matsubara frequency  $iv_0$  has explicitly been extrapolated to an infinite box size. The extrapolated value of  $\Re(\Sigma(iv_0)) = 0.54$  perfectly agrees with the exact result.





## Chapter 5

# AbinitioD $\Gamma$ A results for SrVO $_3$

*This chapter shows the first AbinitioD $\Gamma$ A results for the transition metal oxide SrVO $_3$ . I have chosen SrVO $_3$  as the first material to be studied within AbinitioD $\Gamma$ A since it is a well-established testbed material in the field of strongly correlated materials. Please note that most of the results presented here have already been published in A. Galler et al., Phys. Rev. B 95, 115107 (2017), which has also been taken as the textual basis for this chapter.*

Strontium vanadate, SrVO $_3$ , is a strongly correlated metal that crystallizes in a cubic perovskite lattice structure with lattice constant  $a = 3.8\text{\AA}$ . It has a mass enhancement of  $m^*/m \sim 2$  according to photoemission spectroscopy [118] and specific heat measurements [119]. At low frequencies, SrVO $_3$  further reveals a correlation induced kink in the energy-momentum dispersion relation [77, 120–122] if subject to careful examination [122]. SrVO $_3$  became the testbed material for the benchmarking of new codes and the testing of new methods for strongly correlated electron systems, see e.g. Refs. [48, 92, 118, 120, 123–130]. Besides academic interests, SrVO $_3$  actually has a number of potential technological applications, e.g. as electrode material [131], Mott transistor [132], or as a transparent conductor [133].

Here we first employ Wien2k [19, 113] band-structure calculations in the generalized gradient approximation (GGA) [10] and wien2wannier [49] to project onto maximally localized Wannier functions [50] for the low-energy  $t_{2g}$  orbitals of vanadium. The momentum dispersion corresponding to these orbitals is shown in Fig. 5.1 (left) along with a cut of the Fermi surface (right). For these low-energy orbitals the constrained local density approximation [135] yields an intra-orbital Hubbard  $U = 5\text{ eV}$ , a Hund's exchange  $J = 0.75\text{ eV}$  and an inter-orbital  $U' = U - 2J = 3.5\text{ eV}$  [118, 120]. These

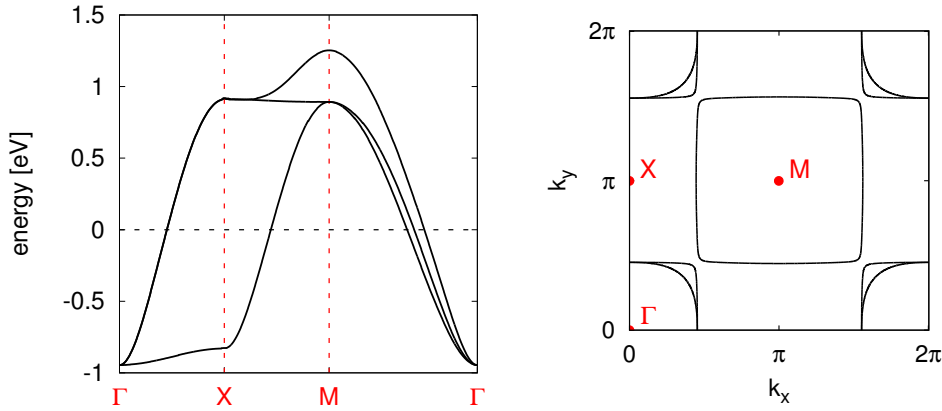


FIGURE 5.1: Band-structure and Fermi surface of SrVO<sub>3</sub> within GGA: Shown is the dispersion of the vanadium  $t_{2g}$  states (left) and the Fermi surface in the  $(k_x, k_y)$ -plane for  $k_z = 0$  (right).

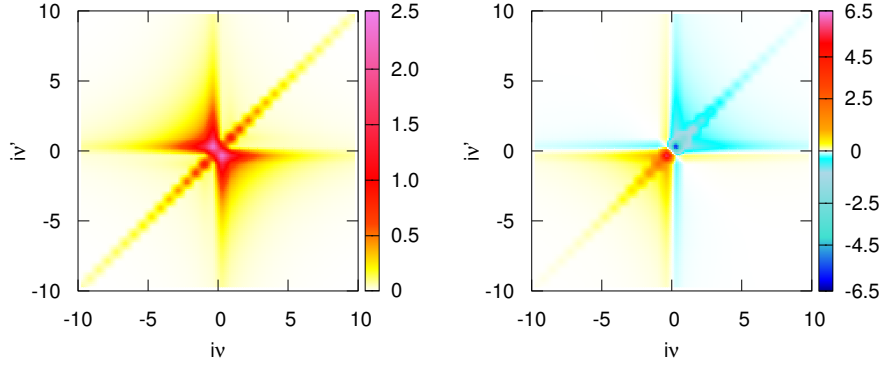


FIGURE 5.2: Real (left) and imaginary (right) part of the generalized susceptibility  $\chi_{m,1111}^{\omega\nu\nu'}$  in the magnetic ( $m$ ) channel for the 1111 orbital component at  $\omega = 0$ .  $\chi$  is related to the irreducible local vertex via Eq. (4.20). By summing  $\chi_{m,1111}^{\omega\nu\nu'}$  over its two fermionic frequencies  $\nu$  and  $\nu'$  one can obtain the physical local magnetic susceptibility  $\chi_m^\omega$ , as e.g. in Ref. [134].

interaction values were shown to reproduce the experimental mass enhancement within DMFT [118, 120, 123].<sup>1</sup>

We use the Kanamori parametrisation of the local interaction with the above values for  $U$ ,  $U'$  and  $J$  and perform DMFT calculations for the thus defined low-energy model at an inverse temperature  $\beta = 10eV^{-1}$ . In DMFT the lattice model is self-consistently mapped onto an auxiliary single Anderson impurity model (AIM) [136]. In order to extract the local dynamic four-point vertex function we use the w2dynamics package [42, 51], which solves the AIM using continuous-time quantum Monte Carlo in the hybridisation

<sup>1</sup>For studying the recently suggested role of plasmonic effects [48, 125, 129] on the quasi-particle renormalization, we would need to include a larger set of orbitals in AbinitioDFA, which is possible if the local vertex corrections are restricted to the  $d$  orbitals. Alternatively, one could perform the AbinitioDFA with a dynamical/retarded interaction.

expansion (CT-HYB) [106, 107]. When considering non-density-density interactions (such as the Kanamori interaction), the multi-orbital vertex function is only accessible by extending CT-HYB with a worm algorithm [108]. To illustrate the complexity of this quantity, we display in Fig. 5.2 the generalized susceptibility  $\chi_{m,1111}^{\omega\nu\nu'}$  [related to the vertex via Eq. (4.20)] as a function of the two fermionic frequencies at zero bosonic frequency and all orbital indices being the same.

While the CT-HYB algorithm is in principle numerically exact, the four-point vertex function usually suffers from poor statistics due to finite computation times. In an effort to limit the statistical uncertainties to an acceptable level, we further make use of a sampling method termed “improved estimators” [109, 112]. This method redefines Green’s function estimators of CT-HYB by employing local versions of the equation of motion, resulting in an improved high-frequency behavior for sampled quantities. Additionally, we also employ high-frequency asymptotics for the vertex function, which further reduce statistical uncertainties and allow for an extrapolation to larger frequency boxes. Thus, within CT-HYB, we sample a cubic frequency box with 120 points in each direction and compute the high frequency asymptotics as described in Ref. [116]. In principle, through the use of the high frequency asymptotics, arbitrary big frequency boxes for the vertex function are accessible. However, in order to limit the numerical effort of the AbinitioDFA program, we restrict ourselves to a maximum of 400 frequency points in each direction.

Before computing the actual AbinitioDFA self-energies for  $\text{SrVO}_3$ , we check the quality and statistics of the four-point vertex sampled in CT-HYB. Thus, we employ the local version of the equation of motion, which should reproduce the original DMFT self-energy and reads  $\Sigma_{\text{DMFT}}^\nu = -\beta^{-1} \sum_{\omega\nu'} U \chi_0^{\omega\nu'\nu'} F_d^{\omega\nu'\nu} G^{\nu-\omega}$  [see Eq. (4.62)]. Fig. 5.3 shows the comparison between the local DMFT self-energy obtained this way (in red) and the original DMFT self-energy (in grey). Small differences are clearly notable. Since similar deviations have already been observed for test cases out of half-filling in Sec. 4.3, where they could be attributed to the finite size of the employed frequency boxes, we study the convergence with respect to the frequency boxes also here. Thus, beside the frequency box of  $\#\omega = 400$  frequencies<sup>2</sup> used to obtain the result in Fig. 5.3, we further employ two smaller frequency boxes with  $\#\omega = 240$  and  $\#\omega = 120$  respectively. Fig. 5.4 shows a clear tendency towards the correct DMFT result with increasing frequency box size. Convergence is, however, not yet reached. In the AbinitioDFA implementation we therefore explicitly substitute  $\Sigma_{\text{DMFT}}^\nu$  with the original DMFT result. Consequently, all remaining  $U$ -terms in the equation of motion (4.71) are non-local terms, which decay faster with frequency than their local counterparts by at least one power. Indeed, the

<sup>2</sup>A frequency box of  $\#\omega = 400$  yields Matsubara frequencies extending to  $\pm(400+1)\pi/\beta$  for fermionic and to  $\pm 400\pi/\beta$  for bosonic frequencies, respectively.

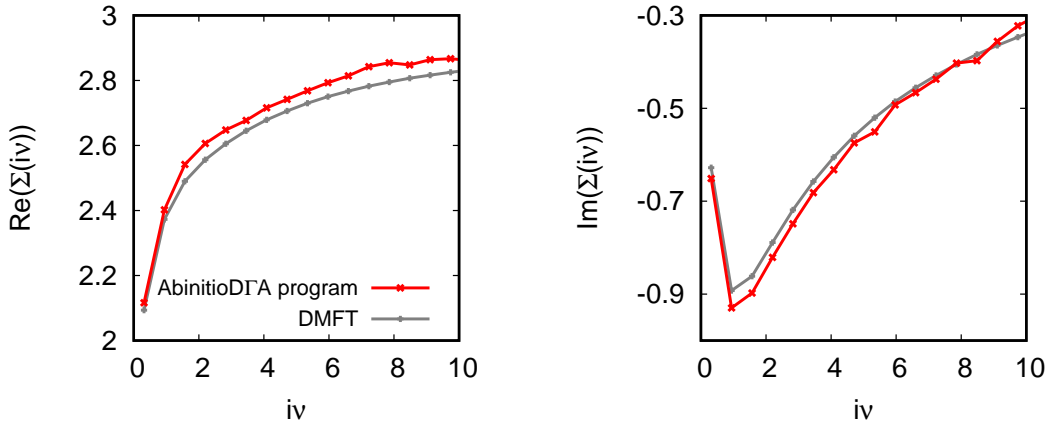


FIGURE 5.3: Comparison between the original DMFT self-energy for  $\text{SrVO}_3$  (in grey) and the local self-energy obtained from the local vertex through the local version of the equation of motion (in red). (employed frequency box size:  $\#\omega = 400$ )

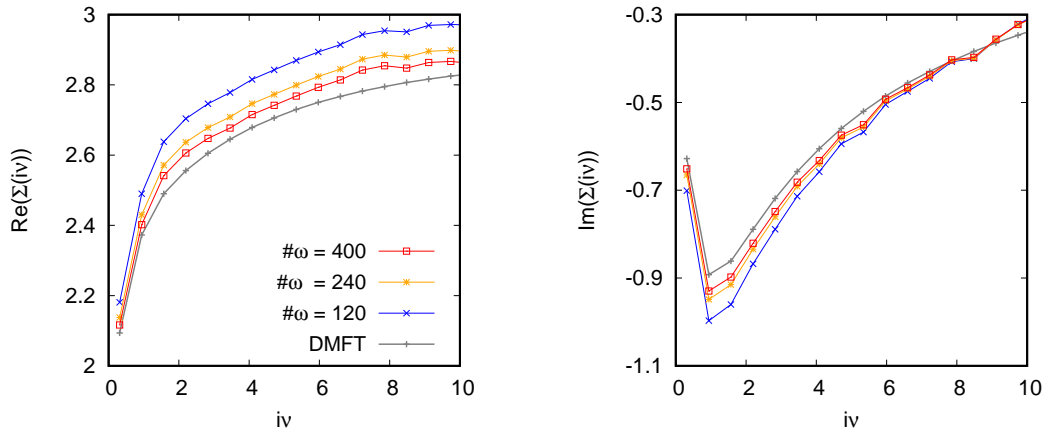


FIGURE 5.4: By increasing the size of the frequency box  $\#\omega$  of the local vertex, the local self-energy slowly approaches the DMFT solution.

AbinitioDFA self-energy obtained this way depends only very weakly on the size of the employed frequency box: in Fig. 5.5, the symbols indicate results for the smallest frequency box  $\#\omega = 120$ , while the lines depict the self-energy for the largest box  $\#\omega = 400$ .

The two top panels of Fig. 5.5 show the momentum-dependent self-energy  $\Sigma_{mm'}(iv, \mathbf{k})$  of  $\text{SrVO}_3$  in the  $t_{2g}$  subspace ( $m = xy, xz, yz$ ) for three selected  $\mathbf{k}$ -points. For a comparison, also the momentum-independent DMFT self-energy is shown. The results have been obtained following the AbinitioDFA approach developed in Sec. 4.1 with the local vertex obtained from a DFT+DMFT calculation (using a constrained DFT interaction) as a starting point. Please note that concomitant to the restriction to the  $t_{2g}$  subspace and

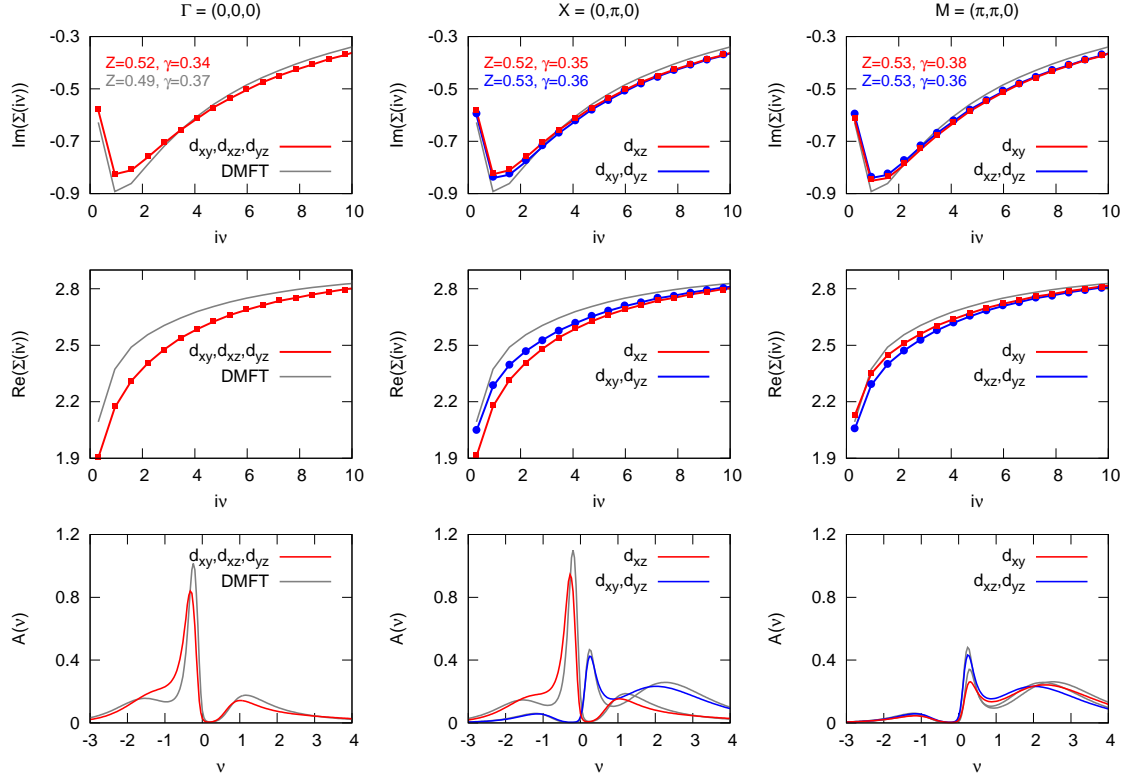


FIGURE 5.5: (Color online) AbinitioDFA  $\mathbf{k}$ -dependent self-energies and spectral functions for  $\text{SrVO}_3$ . Shown are the imaginary (top) and real (middle) part of the self-energy and the corresponding spectral function (bottom) for the  $\mathbf{k}$ -points  $\Gamma = (0, 0, 0)$  (first column),  $X = (0, \pi, 0)$  (second column) and  $M = (\pi, \pi, 0)$  (third column).

the DFT starting point, we did not include the inter-site interaction  $V^{\mathbf{q}}$  yet.<sup>3</sup>

We first discuss the self-energy via its low-frequency expansion:  $\Sigma(i\nu, \mathbf{k}) = \Re(i\nu \rightarrow 0, \mathbf{k}) + i\Im\Sigma(i\nu \rightarrow 0, \mathbf{k}) + (1 - 1/Z_{\mathbf{k}})i\nu + \mathcal{O}(\nu^2)$ . From the local DMFT self-energy we extract<sup>4</sup> a quasi-particle weight  $Z^{\text{DMFT}} = 0.49$  and a scattering rate  $\gamma^{\text{DMFT}} \equiv -\Im\Sigma^{\text{DMFT}}(i\nu \rightarrow 0) = 0.37 \text{ eV}$ . The imaginary parts of the AbinitioDFA Matsubara self-energy (see Fig. 5.5 top panel) suggest a slight enhancement of the quasi-particle weight  $Z_{\mathbf{k}}$  (smaller slope at low energy) for all momenta and orbital components. Interestingly, we find for the quasi-particle weight  $Z_{\mathbf{k}}$  an extremely weak momentum-dependence. Indeed  $Z_{\mathbf{k}}$  varies by less than 2% within the Brillouin zone. This is also illustrated in Fig. 5.6 (d) which displays  $Z_{\mathbf{k}}$  of the  $d_{xy}$  Wannier orbital in the  $k_z = 0$  plane. The corresponding dependence of  $\gamma_{\mathbf{k}}$  is displayed in panel (c) of Fig. 5.6. Also here, we see only a small momentum differentiation of at most 10%.

<sup>3</sup>Using a larger window of orbitals, it would be possible to include  $U + V^{\mathbf{q}}$  even if the local vertex is calculated only for a smaller subset of orbitals. This would yield at least the  $GW$  contribution to the self-energy.

<sup>4</sup>We extract the expansion coefficients from the Matsubara data with a 3rd-order polynomial fit to  $\Sigma(i\nu_n, \mathbf{k})$  at the first six Matsubara frequencies, and limit the discussion to orbital-diagonal components. Spectra are computed with the full self-energy.

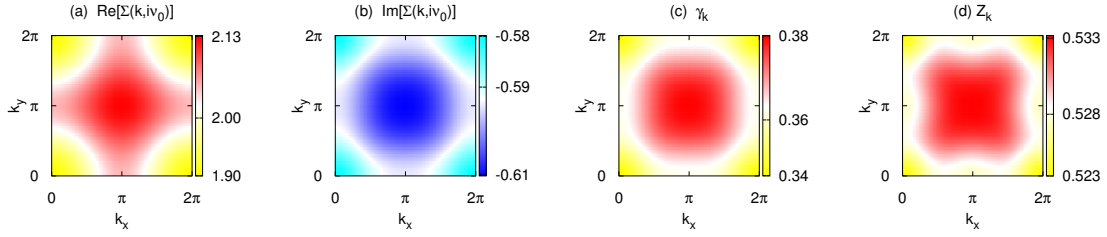


FIGURE 5.6: (a) Real and (b) imaginary part of the AbinitioDFA self-energy  $\Sigma(i\nu_0, \mathbf{k})$  at the first Matsubara frequency  $\nu_0$  (c) scattering rate  $\gamma_{\mathbf{k}}$  and (d) quasiparticle weight  $Z_{\mathbf{k}}$  in the  $k_z = 0$  plane for the  $d_{xy}$  orbital.<sup>a</sup>

<sup>a</sup>We extract the expansion coefficients from the Matsubara data with a 3rd-order polynomial fit to  $\Sigma(i\nu_i, \mathbf{k})$  at the first six Matsubara frequencies, and limit the discussion to orbital-diagonal components. Spectra are computed with the full self-energy.

The momentum-dependence of the DFA self-energy in general further allows for an orbital differentiation of correlation effects in this locally degenerate system.<sup>5</sup> For  $Z_{\mathbf{k}}$  and  $\gamma_{\mathbf{k}}$  that are both obtained from the *imaginary* part of the Matsubara self-energy, only a small difference between non-equivalent orbital components develops (see top panel in Fig. 5.5).

Much more sizable effects occur for both the momentum and the orbital dependence of the *real-part* of the self-energy at low energies. This can be inferred from the middle panel of Fig. 5.5 and Fig. 5.6 (a) that displays  $\Re\Sigma(i\nu_0, \mathbf{k})$  at the lowest Matsubara frequency, again for the  $d_{xy}$  orbital in the  $k_z = 0$  plane. We witness a momentum-differentiation of 0.2eV or more—a quite notable effect beyond DMFT. We note that, contrary to  $Z_{\mathbf{k}}$  and  $\gamma_{\mathbf{k}}$ , the momentum-dependence of  $\Re\Sigma(i\nu_0, \mathbf{k})$  in Figure 5.6 (a) does not mirror the shape of the Fermi surface in Figure 5.1 (right). This will in particular influence transport properties that probe states in close proximity to the Fermi surface.

At low energies, we also find a pronounced orbital-dependence in  $\Re\Sigma(i\nu, \mathbf{k})$ : At the  $X$ -point the real-part of the low-frequency self-energy is larger by about 0.1eV for the (at this  $k$  point) degenerate  $d_{xy}, d_{yz}$  orbitals than for the  $d_{xz}$  component. At the  $M$  point the  $d_{xy}$  component is larger than the  $d_{xz}, d_{yz}$  doublet.

Combining the influence of the orbital- and momentum dependent self-energy, we hence find systematically larger shifts  $\Re\Sigma(i\nu = 0, \mathbf{k})$  for excitations with higher initial (DFT) energy. Seen relatively, this means that unoccupied states are pushed upwards and occupied states downwards, resulting in a widening of the overall band-width. This was previously evidenced using perturbative techniques [127, 129, 137].

<sup>5</sup>In particular, away from high-symmetry points, the lifting of degeneracy also allows for orbital-off-diagonal components in the self-energy. We however find these to be very small in the current system, which is why we limit the discussion to the diagonal components.

At high energies, the self-energy becomes again independent of orbital and momentum to recover the value of the Hartree term.<sup>6</sup>

We now use the maximum entropy method [54, 138] for the analytical of the AbinitioDFA Green's function<sup>7</sup> to real frequency spectra. In the lowest panel of Fig. 5.5 we compare our results to conventional DMFT for selected k-points. From the above discussion it is clear that the AbinitioDFA self-energy will cause quantitative differences in the many-body spectra, while the overall shape will be qualitatively similar to our and previous DMFT results. As evidenced above, the inclusion of non-local fluctuations decreases the degree of electronic correlations: Both, a larger  $Z$  and the shifts induced by  $\Re\Sigma$ , slightly increase the interacting band-width with respect to DMFT. Indeed, we see in our spectra signatures of reduced correlations: Hubbard bands are less pronounced and quasi-particle peaks move away from the Fermi level, although in the current case these effects are small. This is congruent with previous dynamical cluster approximation (DCA) calculations that included short-ranged non-local fluctuations [105]. Let us also note that recently it was indeed found experimentally [139], that the lower Hubbard band in  $\text{SrVO}_3$  is intrinsically somewhat less pronounced than previously thought, with a substantial part of spectral weight actually originating from oxygen vacancies.

The very weak momentum dependence of the quasi-particle dynamics and electronic lifetimes does not come as a surprise. Indeed, the local nature of  $Z$  was previously established in a DFA study of the 3D Hubbard model [101], and, using perturbative techniques, in metallic oxides [129] and the iron pnictides and chalcogenides [137, 140]. On the other hand, these studies found a largely momentum-dependent static contribution  $\Re\Sigma(\nu = 0, \mathbf{k})$  to the self-energy. Going beyond model studies and perturbative methods, we here confirm that  $\Re\Sigma(\nu = 0, \mathbf{k})$  indeed contains non-negligible momentum-dependent correlations beyond DMFT even for only purely local interactions. Still, in the current study, momentum-dependent effects are small enough to only lead to quantitative changes. There are three main reasons for the preponderance of local self-energy effects: (1)  $\text{SrVO}_3$  is not in close proximity to a spin-ordered phase or any other second-order phase transition. Therefore, non-local spin- or charge-fluctuations were not expected to be particularly strong. (2)  $\text{SrVO}_3$  is a cubic, i.e. fairly isotropic system. Non-local correlation effects are generally more pronounced in anisotropic or lower dimensional systems. Therefore, we can speculate that non-local self-energies will become more prevalent in ultra-thin films of  $\text{SrVO}_3$  [132, 141]. (3) The *GW* approach in fact yields a much larger static  $\mathbf{k}$ -dependence  $\Re\Sigma(\nu = 0, \mathbf{k})$  [127, 129]. This is however an effect of the non-locality of the *interaction* which yields a largely momentum-dependent

<sup>6</sup>The Hartree term is  $\mathbf{k}$ -independent since the interactions we use here are local.

<sup>7</sup>In our AbinitioDFA calculations we do not update the chemical potential. However, from the DFA Green's function we find a particle number of 1.062, which is very close to the target occupation of 1.

screened exchange contribution to the self-energy.<sup>8</sup> While non-local interactions are included in the *AbinitioDΓA* formalism (see Sec. 4.1), we here performed calculations with a local interaction only, and are thus missing this effect.

---

<sup>8</sup>Indeed, applying the *GW* approach to the one-band Hubbard model (in which exchange effects are absent by construction), results in a negligible momentum dependence of  $\Re\Sigma(\nu = 0, \mathbf{k})$  in three dimensions [101].



## Chapter 6

# Conclusion and outlook

In this thesis, I have introduced methods to treat materials with local and non-local electronic correlations, namely the well-established DFT+DMFT approach and the newly developed AbinitioD $\Gamma$ A methodology. Furthermore, I have presented results for specific correlated materials—the intermetallic FeAl and the transition metal oxide SrVO<sub>3</sub>.

The first part of this thesis has been devoted to the DFT+DMFT approach and a particular DFT+DMFT study of the intermetallic FeAl. In Chap. 1, which provided a general introduction to the DFT+DMFT method, I have first briefly discussed the basic ideas of density functional theory (DFT). Then, I have introduced the multi-orbital Hubbard model and the necessary steps to combine DFT with DMFT, namely the Wannier projection and the constrained random-phase approximation (cRPA). In the following, the solution of the multi-orbital Hubbard model within dynamical mean-field theory (DMFT) has been discussed in detail. A short section at the end of Chap. 1 has been dedicated to DFT+DMFT spectral functions and the problem of analytical continuation. Finally, in Chap. 2, I have presented the results of a DMFT+DMFT study for the intermetallic FeAl. While DFT wrongly predicts FeAl to be ferromagnetic, no magnetization and a paramagnetic susceptibility for the whole range of temperature investigated is found within DFT+DMFT. I have shown that this behavior originates from quantum fluctuations that screen short-lived local magnetic moments of  $1.6 \mu_B$ .

In the second part of this thesis, starting with Chap. 3, I have presented in detail the newly developed *ab initio* dynamical vertex approximation (AbinitioD $\Gamma$ A). The latter represents a diagrammatic extension of DMFT, which can take into account non-local electronic correlations and a non-local Coulomb interaction. Since AbinitioD $\Gamma$ A is the extension of D $\Gamma$ A to *ab initio* materials' computations, I decided to provide an overview over the basic ideas of D $\Gamma$ A and its success over the last years in Chap. 3. In the following Chap. 4, the multi-orbital AbinitioD $\Gamma$ A equations have been derived and some

implementational details regarding the new AbinitioDFA program have been discussed. In the end of Chap. 4, I also included the results of some test cases, which I used in order to test the newly developed AbinitioDFA program. In Chap. 5, I have finally presented the first AbinitioDFA results for a realistic material, namely  $\text{SrVO}_3$ , a frequently used testbed material in the field of strongly correlated electron systems.

The first AbinitioDFA study for  $\text{SrVO}_3$  shows that the AbinitioDFA methodology, which has been developed within this thesis, is capable of studying non-local electronic correlations in realistic materials. In fact, the present AbinitioDFA study for  $\text{SrVO}_3$  already included three correlated orbitals. The AbinitioDFA method has now been implemented and tested on the testbed material  $\text{SrVO}_3$  and is ready to be used on materials where non-local correlations and a non-local Coulomb interaction are expected to play an important role. However, before that, the role of the non-local Coulomb interaction  $V^{\mathbf{q}}$  still needs to be tested, since it has not yet been included in the AbinitioDFA study for  $\text{SrVO}_3$  presented in this thesis. But once the non-local Coulomb interaction is tested, non-local effects in a variety of materials can be investigated. Possible candidates are e.g. cuprate superconductors with their layered crystal structure or  $\text{SrVO}_3$  thin films. Closely related to the AbinitioDFA approach and possible future projects are also the calculation of the  $\mathbf{q}$ -dependent magnetic susceptibility (e.g. in Fe) and the optical conductivity including vertex corrections. Another remaining task is the further development of the AbinitioDFA program. There, e.g. the implementation of additional symmetries, especially k-point symmetries, could reduce the current numerical effort, making bigger systems with more correlated orbitals accessible to AbinitioDFA.

# Bibliography

- [1] P. Hohenberg and W. Kohn. Inhomogeneous electron gas. *Phys. Rev.*, 136:B864–B871, Nov 1964.
- [2] W. Kohn and L. J. Sham. Self-consistent equations including exchange and correlation effects. *Phys. Rev.*, 140:A1133–A1138, Nov 1965.
- [3] E. Assmann, P. Blaha, R. Laskowski, K. Held, S. Okamoto, and G. Sangiovanni. Oxide heterostructures for efficient solar cells. *Phys. Rev. Lett.*, 110:078701, Feb 2013.
- [4] R. Bliem, E. McDermott, P. Ferstl, M. Setvin, O. Gamba, J. Pavelec, M. A. Schneider, M. Schmid, U. Diebold, P. Blaha, L. Hammer, and G. S. Parkinson. Subsurface cation vacancy stabilization of the magnetite (001) surface. *Science*, 346(6214):1215–1218, 2014.
- [5] W. Metzner and D. Vollhardt. Correlated lattice fermions in  $d = \infty$  dimensions. *Phys. Rev. Lett.*, 62:324–327, Jan 1989.
- [6] A. Georges and G. Kotliar. Hubbard model in infinite dimensions. *Phys. Rev. B*, 45:6479–6483, Mar 1992.
- [7] A. Toschi, A. A. Katanin, and K. Held. Dynamical vertex approximation: A step beyond dynamical mean-field theory. *Phys. Rev. B*, 75:045118, Jan 2007.
- [8] G. Rohringer, A. Toschi, A. Katanin, and K. Held. Critical properties of the half-filled Hubbard model in three dimensions. *Phys. Rev. Lett.*, 107:256402, Dec 2011.
- [9] T. Schäfer, F. Geles, D. Rost, G. Rohringer, E. Arrigoni, K. Held, N. Blümer, M. Aichhorn, and A. Toschi. Fate of the false Mott-Hubbard transition in two dimensions. *Phys. Rev. B*, 91:125109, Mar 2015.
- [10] J. P. Perdew, K. Burke, and M. Ernzerhof. Generalized gradient approximation made simple. *Phys. Rev. Lett.*, 77:3865–3868, Oct 1996.

- [11] F. Tran and P. Blaha. Implementation of screened hybrid functionals based on the Yukawa potential within the LAPW basis set. *Phys. Rev. B*, 83:235118, Jun 2011.
- [12] F. Tran, P. Blaha, M. Betzinger, and S. Blügel. Comparison between exact and semilocal exchange potentials: An all-electron study for solids. *Phys. Rev. B*, 91:165121, Apr 2015.
- [13] M. Betzinger, C. Friedrich, and S. Blügel. Hybrid functionals within the all-electron FLAPW method: Implementation and applications of PBE0. *Phys. Rev. B*, 81:195117, May 2010.
- [14] G. Kresse and D. Joubert. From ultrasoft pseudopotentials to the projector augmented-wave method. *Phys. Rev. B*, 59:1758–1775, Jan 1999.
- [15] P. E. Blöchl. Projector augmented-wave method. *Phys. Rev. B*, 50:17953–17979, Dec 1994.
- [16] G. Kresse and J. Furthmüller. Efficient iterative schemes for *ab initio* total-energy calculations using a plane-wave basis set. *Phys. Rev. B*, 54:11169–11186, Oct 1996.
- [17] J. C. Slater. Wave functions in a periodic potential. *Phys. Rev.*, 51:846–851, May 1937.
- [18] O. K. Andersen. Linear methods in band theory. *Phys. Rev. B*, 12:3060–3083, Oct 1975.
- [19] P. Blaha, K. Schwarz, P. Sorantin, and S. B. Trickey. Full-potential, linearized augmented plane wave programs for crystalline systems. *Computer Physics Communications*, 59(2):399 – 415, 1990.
- [20] J. Hubbard. Electron correlations in narrow energy bands. *Proceedings of the Royal Society of London. Series A, Mathematical and Physical Sciences*, 276(1365):238–257, 1963.
- [21] A. Fetter and J. Walecka. *Quantum Theory of Many-Particle Systems*. Courier Dover Publications, McGraw-Hill, New York, 1971.
- [22] A. Zagoskin. *Quantum Theory of Many-Body Systems: Techniques and Applications*. Springer, London, second edition, 2014.
- [23] K. Held. Electronic structure calculations using dynamical mean field theory. *Advances in Physics*, 56(6):829–926, 2007.
- [24] M. Springer and F. Aryasetiawan. Frequency-dependent screened interaction in Ni within the random-phase approximation. *Phys. Rev. B*, 57:4364–4368, Feb 1998.

- [25] S. Sakai. *Theoretical study of multi-orbital correlated electron systems with Hund's coupling*. PhD thesis, University of Tokyo, 2006.
- [26] T. Ribic, E. Assmann, A. Tóth, and K. Held. Cubic interaction parameters for  $t_{2g}$  Wannier orbitals. *Phys. Rev. B*, 90:165105, Oct 2014.
- [27] J. Kanamori. Electron correlation and ferromagnetism of transition metals. *Progress of Theoretical Physics*, 30(3):275–289, 1963.
- [28] N. Marzari, A. A. Mostofi, J. R. Yates, I. Souza, and D. Vanderbilt. Maximally localized Wannier functions: Theory and applications. *Rev. Mod. Phys.*, 84:1419–1475, Oct 2012.
- [29] G. H. Wannier. The structure of electronic excitation levels in insulating crystals. *Phys. Rev.*, 52:191–197, Aug 1937.
- [30] N. Marzari and D. Vanderbilt. Maximally localized generalized Wannier functions for composite energy bands. *Phys. Rev. B*, 56:12847–12865, Nov 1997.
- [31] R. Wang, E. A. Lazar, H. Park, A. J. Millis, and C. A. Marianetti. Selectively localized Wannier functions. *Phys. Rev. B*, 90:165125, Oct 2014.
- [32] D. Bohm and D. Pines. A collective description of electron interactions. I. magnetic interactions. *Phys. Rev.*, 82:625–634, Jun 1951.
- [33] M. Gell-Mann and K. A. Brueckner. Correlation energy of an electron gas at high density. *Phys. Rev.*, 106:364–368, Apr 1957.
- [34] F. Aryasetiawan, T. Miyake, and R. Sakuma. *The constrained RPA method for calculating the Hubbard  $U$  from first-principles*. Forschungszentrum Jülich, 2011.
- [35] T. Miyake, F. Aryasetiawan, and M. Imada. *Ab initio* procedure for constructing effective models of correlated materials with entangled band structure. *Phys. Rev. B*, 80:155134, Oct 2009.
- [36] T. Kotani. *Ab initio* random-phase-approximation calculation of the frequency-dependent effective interaction between 3d electrons: Ni, Fe, and MnO. *J. Phys: Condens. Matter*, 12(11):2413, 2000.
- [37] F. Gebhard. *The Mott Metal-Insulator Transition, Models and Methods*. Springer, Berlin Heidelberg, 1997.
- [38] K. Held. Electronic structure calculations using dynamical mean field theory. *Adv. Phys.*, 56:829, 2007.

- [39] W. Negele and H. Orland. *Quantum Many-Particle Systems*. Addison-Wesley, New York, 1987.
- [40] J. E. Hirsch and R. M. Fye. Monte Carlo method for magnetic impurities in metals. *Phys. Rev. Lett.*, 56:2521–2524, Jun 1986.
- [41] E. Gull, A. J. Millis, A. I. Lichtenstein, A. N. Rubtsov, M. Troyer, and P. Werner. Continuous-time Monte Carlo methods for quantum impurity models. *Rev. Mod. Phys.*, 83:349–404, May 2011.
- [42] N. Parragh, A. Toschi, K. Held, and G. Sangiovanni. Conserved quantities of  $SU(2)$ -invariant interactions for correlated fermions and the advantages for quantum Monte Carlo simulations. *Phys. Rev. B*, 86:155158, Oct 2012.
- [43] V. I. Anisimov, I. V. Solovyev, M. A. Korotin, M. T. Czyżyk, and G. A. Sawatzky. Density-functional theory and NiO photoemission spectra. *Phys. Rev. B*, 48:16929–16934, Dec 1993.
- [44] P. Wissgott. *Transport properties of correlated materials from first principles*. PhD thesis, TU Wien, 2012.
- [45] V. I. Anisimov, J. Zaanen, and O. K. Andersen. Band theory and Mott insulators: Hubbard  $U$  instead of stoner  $I$ . *Phys. Rev. B*, 44:943–954, Jul 1991.
- [46] S. Biermann, F. Aryasetiawan, and A. Georges. First-principles approach to the electronic structure of strongly correlated systems: Combining the  $GW$  approximation and dynamical mean-field theory. *Phys. Rev. Lett.*, 90:086402, Feb 2003.
- [47] J. M. Tomczak, P. Liu, A. Toschi, G. Kresse, and K. Held. Merging  $GW$  with DMFT and non-local correlations beyond. *preprint arXiv:1703.08446*, 2017.
- [48] L. Boehnke, F. Nilsson, F. Aryasetiawan, and P. Werner. When strong correlations become weak: Consistent merging of  $GW$  and DMFT. *Phys. Rev. B*, 94:201106, Nov 2016.
- [49] J. Kunes, R. Arita, P. Wissgott, A. Toschi, H. Ikeda, and K. Held. Wien2wannier: From linearized augmented plane waves to maximally localized Wannier functions. *Computer Physics Communications*, 181(11):1888–1895, 2010.
- [50] A. A. Mostofi, J. R. Yates, Y. S. Lee, I. Souza, D. Vanderbilt, and N. Marzari. wannier90: A tool for obtaining maximally-localised Wannier functions. *Computer Physics Communications*, 178(9):685–699, 2008.
- [51] M. Wallerberger. *w2dynamics: continuous time quantum Monte Carlo calculations of one- and two-particle propagators*. PhD thesis, TU Wien, 2016.

- [52] S. Bhandary, E. Assmann, M. Aichhorn, and K. Held. Charge self-consistency in density functional theory combined with dynamical mean field theory:  $k$ -space reoccupation and orbital order. *Phys. Rev. B*, 94:155131, Oct 2016.
- [53] J. Schött, I. L. M. Loch, E. Lundin, O. Grånäs, O. Eriksson, and I. Di Marco. Analytic continuation by averaging Padé approximants. *Phys. Rev. B*, 93:075104, Feb 2016.
- [54] A. W. Sandvik. Stochastic method for analytic continuation of quantum Monte Carlo data. *Phys. Rev. B*, 57:10287–10290, May 1998.
- [55] M. Jarrell. *The maximum entropy method: Analytic continuation of QMC data*. Forschungszentrum Jülich, 2012.
- [56] J. M. Tomczak and S. Biermann. Effective band structure of correlated materials: the case of  $\text{VO}_2$ . *Journal of Physics: Condensed Matter*, 19(36):365206, 2007.
- [57] L. Si, O. Janson, G. Li, Z. Zhong, Z. Liao, G. Koster, and K. Held. Quantum anomalous Hall state in ferromagnetic  $\text{SrRuO}_3$  (111) bilayers. *preprint arXiv:1610.01948*, Oct 2016.
- [58] J. Bogner, W. Steiner, M. Reissner, P. Blaha, K. Schwarz, R. Krachler, H. Ipser, and B. Sepiol. Magnetic order and defect structure of  $\text{Fe}_x\text{Al}_{1-x}$  alloys around  $x = 0.5$ : An experimental and theoretical study. *Phys. Rev. B*, 58:14922–14933, Dec 1998.
- [59] G. P. Das, B. K. Rao, P. Jena, and S. C. Deevi. Electronic structure of substoichiometric Fe-Al intermetallics. *Phys. Rev. B*, 66:184203, Nov 2002.
- [60] N. I. Kulikov, A. V. Postnikov, G. Borstel, and J. Braun. Onset of magnetism in B2 transition-metal aluminides. *Phys. Rev. B*, 59:6824–6833, Mar 1999.
- [61] V. Sundararajan, B. R. Sahu, D. G. Kanhere, P. V. Panat, and G. P. Das. Cohesive, electronic and magnetic properties of the transition metal aluminides FeAl, CoAl and NiAl. *Journal of Physics: Condensed Matter*, 7(30):6019, 1995.
- [62] H. Chacham, E. Galvo da Silva, D. Guenzburger, and D. E. Ellis. Electronic structure, magnetic properties, Mössbauer isomer shifts, and hyperfine fields of disordered Fe-rich Fe-Al alloys. *Phys. Rev. B*, 35:1602–1608, Feb 1987.
- [63] P. Mohn, C. Persson, P. Blaha, K. Schwarz, P. Novák, and H. Eschrig. Correlation induced paramagnetic ground state in FeAl. *Phys. Rev. Lett.*, 87:196401, Oct 2001.
- [64] A. V. Smirnov, W. A. Shelton, and D. D. Johnson. Importance of thermal disorder on the properties of alloys: Origin of paramagnetism and structural anomalies in bcc-based  $\text{Fe}_{1-x}\text{Al}_x$ . *Phys. Rev. B*, 71:064408, Feb 2005.

- [65] B. V. Reddy, D. H. Sastry, S. C. Deevi, and S. N. Khanna. Magnetic coupling and site occupancy of impurities in  $\text{Fe}_3\text{Al}$ . *Phys. Rev. B*, 64:224419, Nov 2001.
- [66] D. D. Johnson, D. M. Nicholson, F. J. Pinski, B. L. Gyorffy, and G. M. Stocks. Density-functional theory for random alloys: Total energy within the coherent-potential approximation. *Phys. Rev. Lett.*, 56:2088–2091, May 1986.
- [67] J. Korringa. On the calculation of the energy of a Bloch wave in a metal. *Physica*, 13(67):392 – 400, 1947.
- [68] W. Kohn and N. Rostoker. Solution of the Schrödinger equation in periodic lattices with an application to metallic lithium. *Phys. Rev.*, 94:1111–1120, Jun 1954.
- [69] J. Staunton, B. L. Gyorffy, A. J. Pindor, G. M. Stocks, and H. Winter. Electronic structure of metallic ferromagnets above the Curie temperature. *Journal of Physics F: Metal Physics*, 15(6):1387, 1985.
- [70] A. G. Petukhov, I. I. Mazin, L. Chioncel, and A. I. Lichtenstein. Correlated metals and the LDA +  $U$  method. *Phys. Rev. B*, 67:153106, Apr 2003.
- [71] V. I. Anisimov, A. I. Poteryaev, M. A. Korotin, A. O. Anokhin, and G. Kotliar. First-principles calculations of the electronic structure and spectra of strongly correlated systems: dynamical mean-field theory. *J. Phys. Cond. Matter*, 9:7359, 1997.
- [72] A. I. Lichtenstein and M. I. Katsnelson. Ab initio calculations of quasiparticle band structure in correlated systems: LDA++ approach. *Phys. Rev. B*, 57:6884–6895, Mar 1998.
- [73] G. Kotliar, S. Y. Savrasov, K. Haule, V. S. Oudovenko, O. Parcollet, and C. A. Marianetti. Electronic structure calculations with dynamical mean-field theory. *Rev. Mod. Phys.*, 78:865–951, Aug 2006.
- [74] N. Parragh, G. Sangiovanni, P. Hansmann, S. Hummel, K. Held, and A. Toschi. Effective crystal field and Fermi surface topology: A comparison of  $d$ - and  $dp$ -orbital models. *Phys. Rev. B*, 88:195116, Nov 2013.
- [75] M. Aichhorn, L. Pourovskii, V. Vildosola, M. Ferrero, O. Parcollet, T. Miyake, A. Georges, and S. Biermann. Dynamical mean-field theory within an augmented plane-wave framework: Assessing electronic correlations in the iron pnictide  $\text{LaFeAsO}$ . *Phys. Rev. B*, 80:085101, Aug 2009.
- [76] A. Georges, L. de’ Medici, and J. Mravlje. Strong electronic correlations from Hund’s coupling. *Annual Reviews of Condensed Matter Physics*, 4:137–178, 2013.



- [77] K. Held, R. Peters, and A. Toschi. Poor man's understanding of kinks originating from strong electronic correlations. *Phys. Rev. Lett.*, 110:246402, Jun 2013.
- [78] P. Hansmann, R. Arita, A. Toschi, S. Sakai, G. Sangiovanni, and K. Held. Dichotomy between large local and small ordered magnetic moments in iron-based superconductors. *Phys. Rev. Lett.*, 104:197002, May 2010.
- [79] Y. I. Prokopyev and B. I. Reser. A single-site spin correlation function in paramagnetic iron. *J. Phys. Cond. Matter*, 3:6055, 1991.
- [80] A. Toschi, R. Arita, P. Hansmann, G. Sangiovanni, and K. Held. Quantum dynamical screening of the local magnetic moment in fe-based superconductors. *Phys. Rev. B*, 86:064411, Aug 2012.
- [81] K. Haule and G. Kotliar. Coherenceincoherence crossover in the normal state of iron oxypnictides and importance of Hund's rule coupling. *New Journal of Physics*, 11(2):025021, 2009.
- [82] D. Vollhardt, N. Blümer, K. Held, M. Kollar, J. Schlipf, M. Ulmke, and J. Wahle. *Metallic ferromagnetism: Progress in our understanding of an old strong-coupling problem*, pages 383–396. Springer Berlin Heidelberg, Berlin, Heidelberg, 1999.
- [83] K. Held and D. Vollhardt. Microscopic conditions favoring itinerant ferromagnetism: Hund's rule coupling and orbital degeneracy. *The European Physical Journal B - Condensed Matter and Complex Systems*, 5(3):473–478, 1998.
- [84] R. Klingeler, N. Leps, I. Hellmann, A. Popa, U. Stockert, C. Hess, V. Kataev, H.-J. Grafe, F. Hammerath, G. Lang, S. Wurmehl, G. Behr, L. Harnagea, S. Singh, and B. Büchner. Local antiferromagnetic correlations in the iron pnictide superconductors  $\text{LaFeAsO}_{1-x}\text{F}_x$  and  $\text{Ca}(\text{Fe}_{1-x}\text{Co}_x)_2\text{As}_2$  as seen via normal-state susceptibility. *Phys. Rev. B*, 81:024506, Jan 2010.
- [85] S.L. Skornyakov, A.A. Katanin, and V.I. Anisimov. Linear temperature-dependence of static magnetic susceptibility in  $\text{LaFeAsO}$  from dynamical mean-field theory. *Phys. Rev. Lett.*, 106:047007, 2011.
- [86] G. Kotliar, S. Y. Savrasov, G. Pálsson, and G. Biroli. Cellular dynamical mean field approach to strongly correlated systems. *Phys. Rev. Lett.*, 87:186401, Oct 2001.
- [87] M. H. Hettler, M. Mukherjee, M. Jarrell, and H. R. Krishnamurthy. Dynamical cluster approximation: Nonlocal dynamics of correlated electron systems. *Phys. Rev. B*, 61:12739–12756, May 2000.

- 
- [88] T. Maier, M. Jarrell, T. Pruschke, and M. H. Hettler. Quantum cluster theories. *Rev. Mod. Phys.*, 77:1027–1080, Oct 2005.
- [89] A. S. Belozerov, M. A. Korotin, V. I. Anisimov, and A. I. Poteryaev. Monoclinic  $M_1$  phase of  $\text{VO}_2$ : Mott-Hubbard versus band insulator. *Phys. Rev. B*, 85:045109, Jan 2012.
- [90] Y. Imai and N. Kawakami. Spectral functions in itinerant electron systems with geometrical frustration. *Phys. Rev. B*, 65:233103, May 2002.
- [91] E. Gull, P. Staar, S. Fuchs, P. Nukala, M. S. Summers, T. Pruschke, T. C. Schulthess, and T. Maier. Submatrix updates for the continuous-time auxiliary-field algorithm. *Phys. Rev. B*, 83:075122, Feb 2011.
- [92] H. Lee, K. Foyevtsova, J. Ferber, M. Aichhorn, H. O. Jeschke, and R. Valentí. Dynamical cluster approximation within an augmented plane wave framework: Spectral properties of  $\text{SrVO}_3$ . *Phys. Rev. B*, 85:165103, Apr 2012.
- [93] A. N. Rubtsov, M. I. Katsnelson, and A. I. Lichtenstein. Dual fermion approach to nonlocal correlations in the Hubbard model. *Phys. Rev. B*, 77:033101, Jan 2008.
- [94] G. Rohringer, A. Toschi, H. Hafermann, K. Held, V. I. Anisimov, and A. A. Katanin. One-particle irreducible functional approach: A route to diagrammatic extensions of the dynamical mean-field theory. *Phys. Rev. B*, 88:115112, Sep 2013.
- [95] T. Ayral and O. Parcollet. Mott physics and spin fluctuations: A unified framework. *Phys. Rev. B*, 92:115109, Sep 2015.
- [96] T. Ayral and O. Parcollet. Mott physics and collective modes: An atomic approximation of the four-particle irreducible functional. *Phys. Rev. B*, 94:075159, Aug 2016.
- [97] G. Rohringer, H. Hafermann, A. Toschi, A. A. Katanin, A. E. Antipov, M. I. Katsnelson, A. I. Lichtenstein, A. N. Rubtsov, and K. Held. Diagrammatic routes to non-local correlations beyond dynamical mean-field theory. *preprint arXiv:1705.00024*, Apr 2017.
- [98] T. Schäfer, G. Rohringer, O. Gunnarsson, S. Ciuchi, G. Sangiovanni, and A. Toschi. Divergent precursors of the mott-hubbard transition at the two-particle level. *Phys. Rev. Lett.*, 110:246405, Jun 2013.
- [99] T. Schäfer, S. Ciuchi, M. Wallerberger, P. Thunström, O. Gunnarsson, G. Sangiovanni, G. Rohringer, and A. Toschi. Nonperturbative landscape of the Mott-Hubbard transition: Multiple divergence lines around the critical endpoint. *Phys. Rev. B*, 94:235108, Dec 2016.

- [100] G. Rohringer and A. Toschi. Impact of nonlocal correlations over different energy scales: A dynamical vertex approximation study. *Phys. Rev. B*, 94:125144, Sep 2016.
- [101] T. Schäfer, A. Toschi, and Jan M. Tomczak. Separability of dynamical and non-local correlations in three dimensions. *Phys. Rev. B*, 91:121107, Mar 2015.
- [102] P. Pudleiner, T. Schäfer, D. Rost, G. Li, K. Held, and N. Blümer. Momentum structure of the self-energy and its parametrization for the two-dimensional Hubbard model. *Phys. Rev. B*, 93:195134, May 2016.
- [103] G. Rohringer. *New routes towards a theoretical treatment of nonlocal electronic correlations*. PhD thesis, TU Wien, 2013.
- [104] G. Rohringer, A. Valli, and A. Toschi. Local electronic correlation at the two-particle level. *Phys. Rev. B*, 86:125114, Sep 2012.
- [105] G. Li, N. Wentzell, P. Pudleiner, P. Thunström, and K. Held. Efficient implementation of the parquet equations: Role of the reducible vertex function and its kernel approximation. *Phys. Rev. B*, 93:165103, Apr 2016.
- [106] P. Werner and A. J. Millis. Hybridization expansion impurity solver: General formulation and application to Kondo lattice and two-orbital models. *Phys. Rev. B*, 74:155107, Oct 2006.
- [107] E. Gull, A. J. Millis, A. I. Lichtenstein, A. N. Rubtsov, M. Troyer, and P. Werner. Continuous-time Monte Carlo methods for quantum impurity models. *Reviews of Modern Physics*, 83(2):349–404, May 2011.
- [108] P. Gunacker, M. Wallerberger, E. Gull, A. Hausoel, G. Sangiovanni, and K. Held. Continuous-time quantum Monte Carlo using worm sampling. *Phys. Rev. B*, 92:155102, Oct 2015.
- [109] P. Gunacker, M. Wallerberger, T. Ribic, A. Hausoel, G. Sangiovanni, and K. Held. Worm-improved estimators in continuous-time quantum Monte Carlo. *Phys. Rev. B*, 94:125153, Sep 2016.
- [110] L. Hedin. New method for calculating the one-particle Green’s function with application to the electron-gas problem. *Phys. Rev.*, 139:A796–A823, Aug 1965.
- [111] A. A. Katanin, A. Toschi, and K. Held. Comparing pertinent effects of antiferromagnetic fluctuations in the two- and three-dimensional Hubbard model. *Phys. Rev. B*, 80:075104, Aug 2009.

- [112] H. Hafermann, K. R. Patton, and P. Werner. Improved estimators for the self-energy and vertex function in hybridization-expansion continuous-time quantum Monte Carlo simulations. *Phys. Rev. B*, 85:205106, May 2012.
- [113] K. Schwarz and P. Blaha. Solid state calculations using wien2k. *Comp. Mater. Sci.*, 28:259, 2003.
- [114] F. Aryasetiawan, M. Imada, A. Georges, G. Kotliar, S. Biermann, and A. I. Liechtenstein. Frequency-dependent local interactions and low-energy effective models from electronic structure calculations. *Phys. Rev. B*, 70:195104, Nov 2004.
- [115] T. Miyake and F. Aryasetiawan. Screened Coulomb interaction in the maximally localized Wannier basis. *Phys. Rev. B*, 77:085122, Feb 2008.
- [116] J. Kaufmann, P. Gunacker, and K. Held. Continuous-time quantum Monte Carlo calculation of multi-orbital vertex asymptotics. *preprint arxiv:1703.09407*, Apr 2017.
- [117] N. Wentzell, G. Li, A. Tagliavini, C. Taranto, G. Rohringer, K. Held, A. Toschi, and S. Andergassen. High-frequency asymptotics of the vertex function: diagrammatic parametrization and algorithmic implementation. *preprint arxiv:1610.06520*, 2017.
- [118] A. Sekiyama, H. Fujiwara, S. Imada, S. Suga, H. Eisaki, S. I. Uchida, K. Takegahara, H. Harima, Y. Saitoh, I. A. Nekrasov, G. Keller, D. E. Kondakov, A. V. Kozhevnikov, Th. Pruschke, K. Held, D. Vollhardt, and V. I. Anisimov. Mutual experimental and theoretical validation of bulk photoemission spectra of  $\text{Sr}_{1-x}\text{Ca}_x\text{VO}_3$ . *Phys. Rev. Lett.*, 93(15):156402, Oct 2004.
- [119] I. H. Inoue, O. Goto, H. Makino, N. E. Hussey, and M. Ishikawa. Bandwidth control in a perovskite-type  $3d^1$ -correlated metal  $\text{Ca}_{1-x}\text{Sr}_x\text{VO}_3$ . I. evolution of the electronic properties and effective mass. *Phys. Rev. B*, 58:4372–4383, Aug 1998.
- [120] I. A. Nekrasov, K. Held, G. Keller, D. E. Kondakov, Th. Pruschke, M. Kollar, O. K. Andersen, V. I. Anisimov, and D. Vollhardt. Momentum-resolved spectral functions of  $\text{SrVO}_3$  calculated by LDA+DMFT. *Phys. Rev. B*, 73:155112, Apr 2006.
- [121] K. Byczuk, M. Kollar, K. Held, Y.-F. Yang, I. A. Nekrasov, T. Pruschke, and D. Vollhardt. Kinks in the dispersion of strongly correlated electrons. *Nature Physics*, 3:168, 2007.

- [122] S. Aizaki, T. Yoshida, K. Yoshimatsu, M. Takizawa, M. Minohara, S. Ideta, A. Fujimori, K. Gupta, P. Mahadevan, K. Horiba, H. Kumigashira, and M. Oshima. Self-energy on the low- to high-energy electronic structure of correlated metal  $\text{SrVO}_3$ . *Phys. Rev. Lett.*, 109:056401, Jul 2012.
- [123] E. Pavarini, S. Biermann, A. Poteryaev, A. I. Lichtenstein, A. Georges, and O. K. Andersen. Mott transition and suppression of orbital fluctuations in orthorhombic  $3d^1$  perovskites. *Phys. Rev. Lett.*, 92:176403, Apr 2004.
- [124] M. Casula, A. Rubtsov, and S. Biermann. Dynamical screening effects in correlated materials: Plasmon satellites and spectral weight transfers from a Green’s function ansatz to extended dynamical mean field theory. *Phys. Rev. B*, 85:035115, Jan 2012.
- [125] J. M. Tomczak, M. Casula, T. Miyake, F. Aryasetiawan, and S. Biermann. Combined  $GW$  and dynamical mean-field theory: Dynamical screening effects in transition metal oxides. *EPL (Europhysics Letters)*, 100(6):67001, 2012.
- [126] C. Taranto, M. Kaltak, N. Parragh, G. Sangiovanni, G. Kresse, A. Toschi, and K. Held. Comparing quasiparticle  $GW$ +DMFT and LDA+DMFT for the test bed material  $\text{SrVO}_3$ . *Phys. Rev. B*, 88:165119, 2013.
- [127] T. Miyake, C. Martins, R. Sakuma, and F. Aryasetiawan. Effects of momentum-dependent self-energy in the electronic structure of correlated materials. *Phys. Rev. B*, 87:115110, Mar 2013.
- [128] R. Sakuma, P. Werner, and F. Aryasetiawan. Electronic structure of  $\text{SrVO}_3$  within  $GW$ +DMFT. *Phys. Rev. B*, 88:235110, Dec 2013.
- [129] J. M. Tomczak, M. Casula, T. Miyake, and S. Biermann. Asymmetry in band widening and quasiparticle lifetimes in  $\text{SrVO}_3$ : Competition between screened exchange and local correlations from combined  $GW$  and dynamical mean-field theory  $GW + \text{DMFT}$ . *Phys. Rev. B*, 90:165138, Oct 2014.
- [130] K. Nakamura, Y. Nohara, Y. Yosimoto, and Y. Nomura. *Ab initio*  $GW$  plus cumulant calculation for isolated band systems: Application to organic conductor  $(\text{TMTSF})_2\text{PF}_6$  and transition-metal oxide  $\text{SrVO}_3$ . *Phys. Rev. B*, 93:085124, Feb 2016.
- [131] J. A. Moyer, C. Eaton, and R. Engel-Herbert. Highly conductive  $\text{SrVO}_3$  as a bottom electrode for functional perovskite oxides. *Advanced Materials*, 25(26): 3578–3582, 2013.

- [132] Z. Zhong, M. Wallerberger, J. M. Tomczak, C. Taranto, N. Parragh, A. Toschi, G. Sangiovanni, and K. Held. Electronics with correlated oxides:  $\text{SrVO}_3/\text{SrTiO}_3$  as a Mott transistor. *Phys. Rev. Lett.*, 114:246401, Jun 2015.
- [133] L. Zhang, Y. Zhou, L. Guo, W. Zhao, A. Barnes, H. Zhang, C. Eaton, Y. Zheng, M. Brahlek, H. F. Haneef, N. J. Podraza, M. H. W. Chan, V. Gopalan, K. M. Rabe, and R. Engel-Herbert. Correlated metals as transparent conductors. *Nature Materials*, 15(2):204–210, Feb 2016.
- [134] A. Galler, C. Taranto, M. Wallerberger, M. Kaltak, G. Kresse, G. Sangiovanni, A. Toschi, and K. Held. Screened moments and absence of ferromagnetism in FeAl. *Phys. Rev. B*, 92:205132, Nov 2015.
- [135] V. I. Anisimov and O. Gunnarsson. Density-functional calculation of effective Coulomb interactions in metals. *Phys. Rev. B*, 43:7570–7574, Apr 1991.
- [136] A. Georges, G. Kotliar, W. Krauth, and M. J. Rozenberg. Dynamical mean-field theory of strongly correlated fermion systems and the limit of infinite dimensions. *Rev. Mod. Phys.*, 68(1):13, Jan 1996.
- [137] J. M. Tomczak. QsGW+DMFT: an electronic structure scheme for the iron pnictides and beyond. *Journal of Physics: Conference Series*, 592(1):012055, 2015.
- [138] M. Jarrell and J. E. Gubernatis. Bayesian inference and the analytic continuation of imaginary-time quantum Monte Carlo data. *Physics Reports*, 269(3):133 – 195, 1996.
- [139] S. Backes, T. C. Rödel, F. Fortuna, E. Frantzeskakis, P. Le Fèvre, F. Bertran, M. Kobayashi, R. Yukawa, T. Mitsuhashi, M. Kitamura, K. Horiba, H. Kumigashira, R. Saint-Martin, A. Fouchet, B. Berini, Y. Dumont, A. J. Kim, F. Lechermann, H. O. Jeschke, M. J. Rozenberg, R. Valentí, and A. F. Santander-Syro. Hubbard band versus oxygen vacancy states in the correlated electron metal  $\text{SrVO}_3$ . *Phys. Rev. B*, 94:241110, Dec 2016.
- [140] J. M. Tomczak, M. van Schilfgaarde, and G. Kotliar. Many-body effects in iron pnictides and chalcogenides: Nonlocal versus dynamic origin of effective masses. *Phys. Rev. Lett.*, 109:237010, Dec 2012.
- [141] K. Yoshimatsu, T. Okabe, H. Kumigashira, S. Okamoto, S. Aizaki, A. Fujimori, and M. Oshima. Dimensional-crossover-driven metal-insulator transition in  $\text{SrVO}_3$  ultrathin films. *Phys. Rev. Lett.*, 104:147601, Apr 2010.

# *Acknowledgements*

My doctoral studies and this thesis would not have been possible without the support of many people. First of all, I would like to thank my supervisor Karsten Held for giving me the opportunity to write my doctoral thesis (and previously also my diploma thesis) in his group. I really appreciate that I could do my doctoral studies and my first steps in research in his lively and active group. The projects which I was working on, especially the AbinitioDFA project, were very interesting and forefront in their field of research and in numerous discussions over the last years I could profit a lot from Karsten's expertise and experience. Furthermore, I got the opportunity to attend many international schools and conferences, where I could learn about new topics and present my research.

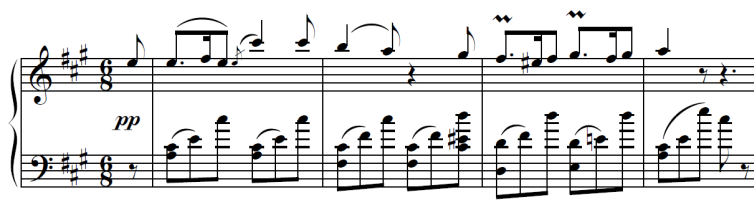
Especially I would like to thank also Jan Tomczak, who co-supervised my doctoral studies from the beginning till the finalization of this thesis. I could learn a lot from his expertise. He was always there for any kind of questions I had and very supportive whenever I had my own ideas. At the same time, I would like to thank also Patrik Thunström, my second co-supervisor. He dedicated a lot of his time to fruitful and precious discussions, from which I learned a lot. Furthermore, I also really appreciate that he invited me to visit him and the materials's theory group at Uppsala University.

Furthermore, I would like to thank Alessandro Toschi for many pedagogical lectures and discussions over the last years. Special thanks also go to the people with whom I probably shared most of the time here in the group in Vienna: my Solids4fun companions Thomas Schäfer and Liang Si and my long-term office-mates Patrik Gunacker and Markus Wallerberger. However, I want to thank also all other present and former colleagues: Elias Assmann, Marco Battiato, Sumanta Bhandary, Oleg Janson, Josef Kaufmann, Anna Kauch, Motoharu Kitatani, Gang Li, Petra Pudleiner, Tin Ribic, Georg Rohringer, Daniel Springer, Ciro Taranto, Angelo Valli, Michael Wais (and everyone who might be missing on this list). Thanks for all the scientific and non-scientific discussions and for sharing a great time!

I acknowledge financial support from the Austrian Science Fund (FWF) through the doctoral school W1243 Solids4Fun (Building Solids for Function), and the European Research Council through Karsten Held's ERC grant. I am thankful that I got public financial support for my PhD studies. At this point I would like to thank also the TU Vienna and all the professors whose lectures I attended throughout these years: for providing a very good education in physics.

Besonders bedanken möchte ich mich auch bei meinen Freunden, die mich über all die Jahre meines Studiums hier in Wien begleitet haben. Es ist auch euer Verdienst, dass ich mich hier zu Hause fühle!

Mein größter Dank geht jedoch an meine Familie, besonders an meine Eltern Elisabeth und Martin. Vielen Dank für eure konstante Unterstützung und Ermutigung, auf die ich mich immer verlassen kann! Nicht zuletzt seid ihr mir auch ein Vorbild, unter anderem wenn es darum geht, mit Mut und Fleiß neue Herausforderungen anzugehen.



*Frühlingstraum*, F. Schubert *Winterreise*



# Curriculum vitae

## Anna Galler

Born on January 12, 1988, in Bozen (Italy)

### Education:

**Ph.D. studies in Physics** at Vienna University of Technology (TU Vienna), since 09/2013

**BA in Philosophy** completed with distinction at Vienna University, 07/2016

Title of the thesis: *Biopolitik und Rassismus. Michel Foucaults Analyse und deren Aktualität*

Supervisor: Dr. Gerhard Unterthurner

**Dipl.-Ing. equiv M.Sc. in Technical Physics** completed with distinction at TU Vienna, 06/2013

Title of the thesis: *Electronic correlations in FeAl: an LDA+DMFT study*

Supervisor: Prof. Karsten Held

**BSc in Technical Physics** completed with distinction at TU Vienna, 10/2010

Title of the thesis: *Hall effect and electrical conductivity of Nb and Ag*

Supervisor: Prof. Silke Bühler-Paschen

**Matura** secondary school leaving exam with distinction *100/100 cum laude* at Realgymnasium Bozen, 07/2007

### Employment:

**Scientific Project Assistant** at the Institute of Solid State Physics, TU Vienna, in the group of Prof. Karsten Held, since 09/2013

**Internship** at Infineon Technologies Austria AG in the Research and Development Center Automotive in Villach (Austria), from 07/2012 to 08/2012

**Internship** at the EURAC Institute for Applied Remote Sensing, Bozen, from 07/2009 to 09/2009

Project: Climate Change in South Tyrol, high resolution monitoring and modelling of satellite data

### Teaching:

I was a teaching assistant for the following undergraduate courses at TU Vienna:

**Quantum Mechanics II**, winter terms 2014/15 and 2012/13

**Quantum Mechanics I**, winter term 2013/14

**Mathematics II for Geodesy**, summer term 2012

**Analysis I for Technical Physics**, winter terms 2012/13, 2011/12, 2010/11

## Languages:

**English:** very good (University of Cambridge Examinations: First Certificate in English, Grade A)

**Italian:** very good

**German:** mother tongue

## Publications:

A. Galler, J. Kaufmann, P. Gunacker, P. Thunström, J. M. Tomczak and K. Held: *Towards ab initio calculations with the dynamical vertex approximation*, submitted to JPSJ (May 2017)

A. Galler, P. Thunström, P. Gunacker, J. M. Tomczak and K. Held: *Ab initio dynamical vertex approximation*, Phys. Rev. B 95, 115107 (2017)

A. Galler, C. Taranto, M. Wallerberger, M. Kaltak, G. Kresse, G. Sangiovanni, A. Toschi and K. Held: *Screened moments and absence of ferromagnetism in FeAl*, Phys. Rev. B 92, 205132 (2015)

## Conferences and workshops attended:

**Theory winter school** on the modeling of correlated electron materials, National high magnetic field laboratory, Tallahassee (Florida), 01/2017

Contribution: *Ab initio dynamical vertex approximation* (poster)

**Conference New Generations Strongly Correlated Electron Systems**, Trieste (Italy), 09/2016

Contribution: *Towards an ab initio treatment of non-local electronic correlations with dynamical vertex approximation* (talk)

**Summer school** of the FWF doctoral school Solids4fun (Building Solids for Function), Waidhofen an der Ybbs (Austria), 07/2016

Contribution: *AbinitioDFA: a new method for materials with non-local electronic correlations* (talk)

**March Meeting** of the American Physical Society (APS), Baltimore (US), 03/2016

Contribution: *Towards an ab initio treatment of non-local electronic correlations with dynamical vertex approximation* (talk)

**Summer school** of the FWF doctoral school Solids4fun, Hernstein (Austria), 07/2015

Contribution: *Screened moments and absence of ferromagnetism in FeAl* (talk)

**Summer school** of the Simons Collaboration on the Many Electron Problem, Stony Brook University (US), 06/2015

Contribution: *Screened moments and absence of ferromagnetism in FeAl* (talk)

**Spring Meeting** of the German Physical Society (DPG), Condensed Matter Section, TU Berlin (Germany), 03/2015

Contribution: *Magnetic properties of FeAl: an LDA+DMFT study* (talk)

**Young scientists meeting** of the DFG Research unit FOR1346: Dynamical Mean-Field Approach with Predictive Power for Strongly Correlated Materials, Würzburg (Germany), 02/2015

**Autumn school** on Correlated Electrons, DFG Research unit FOR1346, Forschungszentrum Jülich (Germany), 09/2014

**Workshop Quantum Critical Matter—from Atoms to Bulk**, University Center Obergurgl (Austria), 08/2014

Contribution: *Correlation effects in the intermetallic CrSb<sub>2</sub>* (poster)

**Young researchers meeting** of the Vienna Computational Materials Laboratory (SFB-ViCom), Vienna, 04/2014

Contribution: *The correlated semiconductor CrSb<sub>2</sub>* (poster)

**DPG Spring Meeting**, Condensed Matter Section, Dresden (Germany), 04/2014

Contribution: *The correlated semiconductor CrSb<sub>2</sub>* (poster)

**Young European Scientists meeting** of the Marie Curie CCQED network, Landeck/Zams (Austria), 03/2014

Contribution: *Electronic structure of solids: The LDA+DMFT approach* (invited talk)

**European Forum Alpbach**, Technology Symposium, participation supported by a scholarship of the Austrian Ministry for Transport, Innovation and Technology, Alpbach (Austria), 08/2013

**DPG Spring Meeting**, Condensed Matter Section, Regensburg (Germany), 03/2013

Contribution: *Electronic correlations in FeAl: an LDA+DMFT study* (poster)

**Summer school Bandstructure meets Many Body Theory**, TU Vienna, 09/2012

**Summer school Introductory Course on Quantum Information and Quantum Gases**, University of Innsbruck (Austria), 07/2010

**Mathematik-Modellierungswoche**, TU Kaiserslautern (Germany), participation supported by a scholarship of the Autonomous Province Bozen-Südtirol, 06/2006

## Research visits and seminar talks:

**École polytechnique**, Paris (France), Prof. Silke Biermann, 22/02-24/02/2017

Invited seminar talk: *Towards a realistic description of materials with strong local and non-local electronic correlations*

**University of Innsbruck**, Prof. Hans Briegel, 08/02-09/02/2017

Invited seminar talk: *Towards a realistic description of materials with strong local and non-local electronic correlations*

**Dahlem Center for Complex Quantum Systems**, FU Berlin (Germany), Prof. Piet Brouwer, 02/02/2017

Invited seminar talk: *Towards a realistic description of materials with strong local and non-local electronic correlations*

**Uppsala University** (Sweden), Prof. Olle Eriksson, 12/12-16/12/2016

Invited seminar talk: *Towards a realistic description of materials with strong local and non-local electronic correlations*

**Columbia University**, New York (US), Prof. Andrew Millis, 21/03-22/03/2016

**Georgetown University**, Washington D.C. (US), Prof. Jim Freericks, 10/03-11/03/2016

Seminar talk: *Towards a realistic description of materials with local and non-local electronic correlations*

**University of Innsbruck**, internship in the group of Prof. Rudolf Grimm, 07/2010-08/2010  
Experimental project work on ultracold RbCs molecules

## Awards and Fellowships:

**Fellow** of the TU Vienna graduate school Solids4fun (Building Solids for Function), since 11/2013

**Fellow** of the Austrian academic scholarship foundation ProScientia, 03/2014-02/2017

Participation in the **High Potential Program** of the TU Vienna, 10/2011-06/2012

**Merit-based grant** by the *Stiftung Südtiroler Sparkasse* and the *Unternehmerverband Südtirol* for academic achievements, 11/2011

**Merit scholarship** by the Autonomous Province Bozen-Südtirol: 07/2013, 07/2012, 07/2011, 07/2010, 07/2009

**Merit scholarship** by the *Stiftung Südtiroler Sparkasse* and the *Unternehmergeverband Südtirol* for the best secondary school graduates in the Autonomous Province Bozen-Südtirol, 10/2007

**Merit scholarship** by the Italian Republic for a secondary school leaving exam with highest marks, 09/2007